Black Hole and Host Galaxy Co-Evolution

Matthew Ryan Thorne

Physics

Department of Physics

Lancaster University

January 28, 2026

A thesis submitted to Lancaster University for the degree of Doctor of Philosophy in the Faculty of Science and Technology

Supervised by Dr Brooke Simmons

Abstract

The origins and the evolution of the observed correlations between supermassive black holes (SMBHs) and their host galaxies are still under debate. A merger-driven co-evolution framework has been a popular hypothesis, and suggests that mergers fuel both star formation and SMBH accretion. However, there is now evidence that the majority of black hole growth has occurred in the absence of mergers; moreover, a merger-driven scenario does not account for the rapidly accreting SMBHs, known as active galactic nuclei (AGN), observed in galaxies with morphologies indicative of a secular evolutionary history.

The nature of co-evolution in disc-dominated galaxies is unclear, with different studies of unobscured (Type 1) AGN drawing contradictory conclusions. We analyse three such samples, applying their selection functions to a mock population of Type 1 AGN. We find that the different samples from the published studies are consistent with being drawn from the same underlying population. The mock AGN population is agnostic to the specifics of galaxy mass accretion and assembly. The fact that the disc galaxy samples are in agreement with the mock sample supports the growing consensus that merger-free black hole growth is typical and can lead to co-evolution between supermassive black holes and galaxies.

We then use multicomponent 2D decomposition to examine the morphological dependence, as traced by bulge-to-total (B/T) ratio, of the correlations between SMBH mass and both total and bulge stellar mass for a sample of 415 Type 1 AGN at $z < 0.35$. We use mock synthetic AGN host galaxies, generated by inserting point sources into inactive galaxies, to show that the decomposition process is reliable

with small systematics. We find no morphological dependence on the SMBH mass-total stellar mass relation, while we find that the SMBH mass-bulge stellar mass relation is a shallower relation and dependent on B/T, with SMBHs in disc-dominated galaxies being offset above SMBHs hosted in bulge-dominated galaxies for a given bulge stellar mass. This further supports the hypothesis that secular evolution plays a strong role in driving co-evolution.

In summary, regardless of the mechanism driving bulge growth, co-evolution of the galaxy and SMBH clearly occurs, and is more strongly tied to the total stellar mass than to bulge properties. Thus, AGN growth may be more related to the total gravitational potential, which is better traced by the total stellar mass than the bulge stellar mass. The new and upcoming surveys are well placed to further this work with larger or higher resolution samples.

To anyone who was always asking ‘why?’ as a child.

Acknowledgements

Since I was a child I have always been intrested in science, most of all Astrophysics. There are many people who have helped me throughout my life to get me where I am today. I offer my sincere gratitude and thanks to people who have helped me during my PhD:

My supervisor Brooke Simmons. Your guidance, enthusiasm, support, and pacience over these many years have made this work possible.

My collaborater at IMPU, John Silverman. Thank you for allowing me to work with you. The experience at IPMU was invaluable.

My examiners Isobel Hook and James Mullaney. Your comments on this work greatly improved its quality.

The academics in the department: John Stott, Julie Wardlow, Mathew Smith, and Sam Oates.

The PhDs, Postdocs, and others at Lancaster and IMPU, who made them such welcoming places. Bruna Araujo, Sonny Bailey, Kevin Bosseboeuf, Jon Carrick, Tom Cornish, Georgios Dimitriadis, Xuheng Ding, Jamie Dumayne, Chris Duffy, Pascale Desmet, Izzy Garland, Melzie Ghendrih, Scott Hagen, Fergus Henstridge, Naoki Itoh, Boris Kalita, Young-Lo Kim, Qiuyue Liang, Zhaoxuan Liu, Jason Makechemu, Alice Mead, Andrew Milligan, Masafusa Onoue, Rahul Rana, Rahul Rana, Wenke Ren, Sam Shilling, Yasuyuki Shimizu, Harry Stephenson, Tomoko Suzuki, Takumi Takana, Katya Vovk, Heather Wade. Especially to any who played Table Tennis or Cricket with me!

My housemates and close friends: Abby Taylor, Amy Hewitt, Arthur Tshaka, David O'Ryan, Faye Davis, George Johnson, Mayur Helia,

Nikita Mehta, Patrica Valimaa, and Zach Mason. Thank you for the many great stories and precious memories. I wish you all the best.

My A-level physics class: Mr White, Miss Wood, Christian Weir, George Browne, Kerys Melvin Smith, Matthew Dengel, and Stephen Brown. Thank you for the great camping trips.

Rach Howden, my landlord and new friend: Thank you for welcoming me into your home during the final months of my PhD, and also a thank you to Monet Ada, Lyra, and Henry.

My parents who have always supported me and have helped me make my own way in life.

My close family, Emma, Jon, Kieran, Ella, Leo, Freddie, Nanny, Granddad Jim, Granny, Suzy, Stuart, Grandad Donald, Hazel and Grandad Bruce.

A special thank you to the many dyslexia support workers who have helped me with my dyslexia from primary school to university.

This research was funded by the Science and Technology Funding Council of the UK, without them, this work would not have been possible.

Finally, to Hasumi Arai. I thank you for your love, support, and most importantly, patience during my PhD journey. I look forward to continuing our life together.

Declaration

This thesis is my own work and no portion of the work referred to in this thesis has been submitted in support of an application for another degree or qualification at this or any other institute of learning.

The most terrifying fact about the universe is not that it is hostile but that it is indifferent, but if we can come to terms with this indifference, then our existence as a species can have genuine meaning. However vast the darkness, we must supply our own light.

- Stanley Kubrick

*

You'll never know unless you try.

- proverb

*

Standing on a bridge at midnight
When a thought came to my head:
"What a fool I am for standing here,
When I should be at home in bed."

- RIP Granddad Jim (1930-2024)

Contents

List of Figures

Chapter 1

Introduction

1.1 Background

The field of Astrophysics is focused on understanding the nature of celestial objects through the application of physics. A key aspect of this is the study of galaxies, which are gravitationally bound objects consisting of Dark Matter in a halo and Baryonic matter in the form of gas, dust, stars, Black Holes, planets, etc. Most galaxies are believed to host at least one supermassive black hole (SMBH) (Magorrian et al., 1998), which is known as an Active Galactic Nucleus (AGN) while accreting matter. In this thesis, I investigate the relationship between SMBHs and their host galaxies through mass scaling relations. In the text below, I will introduce and cover both, starting with how AGN were first discovered and came to be understood.

1.1.1 Active Galactic Nuclei

AGN are characterised by their extreme emissions across multiple wavelengths, which led to independent discoveries in different bands. The first recorded observation of what would become known as an AGN was by Fath (1909), who noted extreme emission lines in the spectrum of NGC 1068. However, the nature of this object was a mystery, as this predated the confirmation of galaxies beyond

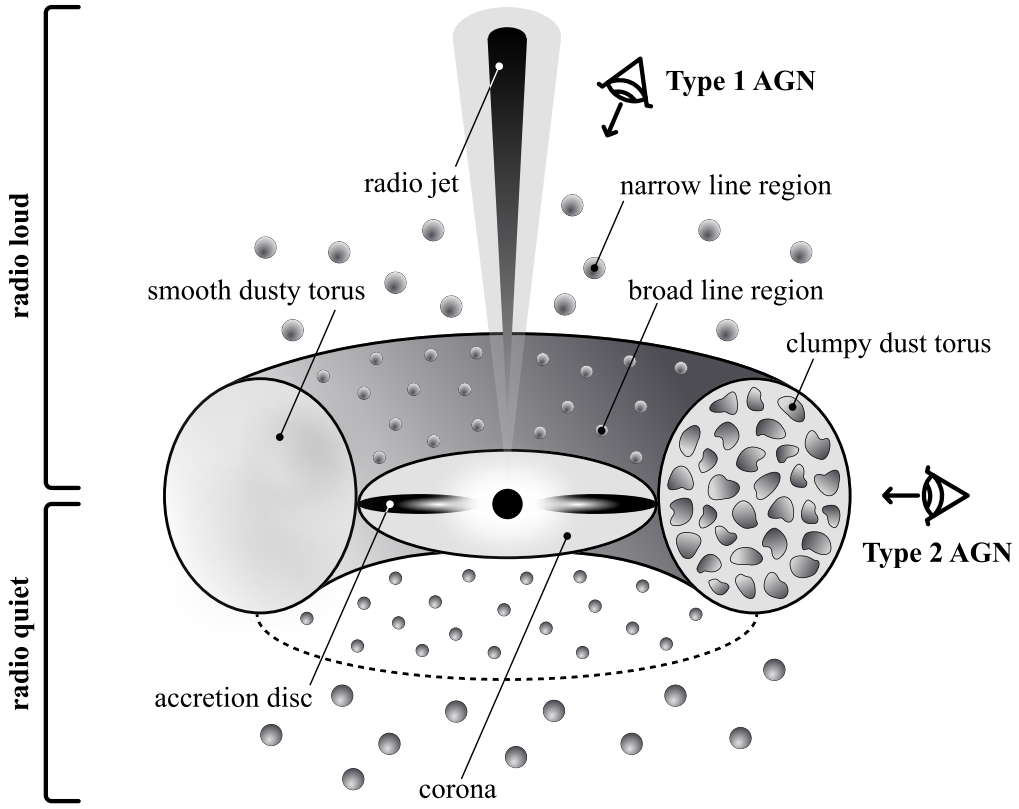

Figure 1.1: A unified scheme of radiative mode AGN structure showing how viewing angle affects the observed emission. Illustrated by Zach Mason

our own by Hubble (1926). Later studies revealed two different classes of strong emission-line galaxies: Type 1, which included broad emission lines, and Type 2, which only possessed narrow emission lines (Weedman, 1973; Khachikian & Weedman, 1974). Concurrently, radio astronomers noticed extreme radio sources that seemed to emanate from optical point sources at the centres of galaxies (Schmidt, 1963). Additionally, in some galaxies, non-thermal radio emissions were detected in collimated jets and large extended structures and appeared to be driven by a central source (e.g., Baade & Minkowski 1954; Burbidge et al. 1963).

Theories on the mechanisms capable of producing the energies associated with such objects began to emerge. The most prevailing theory was of mass accretion

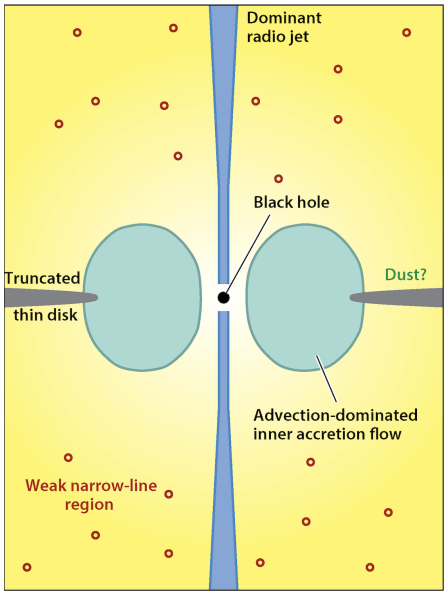

Figure 1.2: A unified scheme of jet mode AGN structure (Heckman & Best, 2014).

onto a supermassive black hole (SMBH) (SMBH; Hoyle & Fowler, 1963; Lynden-Bell, 1969; Lynden-Bell & Rees, 1971). This eventually led to the unification of AGN, which is a widely accepted model. It postulates that the different observed properties arise from differing viewing angles of the same fundamental structure (e.g., Antonucci 1993; Urry & Padovani 1995). The Unification model has been expanded upon to include two distinct AGN accretion modes (Hardcastle et al., 2007; Heckman & Best, 2014; Hardcastle, 2018), the radiative and the jet mode. They are characterised by different radiative efficiency and energy transport mechanisms, which can have different impacts on the host galaxies; this is further discussed in Section 1.4.1.1. These different accretion modes are believed to be related to the nature of accretion flow, the fuelling mechanism and the properties of the accreted matter (Hardcastle et al., 2007; Heckman & Best, 2014; Hardcastle, 2018). The unification model for radiative-mode AGN can be seen in Figure 1.1, while Figure 1.2 shows the model for Jet-mode AGN.

In the Radiative mode, the efficient conversion of potential energy into electromagnetic radiation during accretion is the dominant energy output of the AGN. A broadly representative spectral energy distribution (SED) from radio to hard X-rays of radiative mode AGN is shown in Figure 1.3 and is taken from Harrison

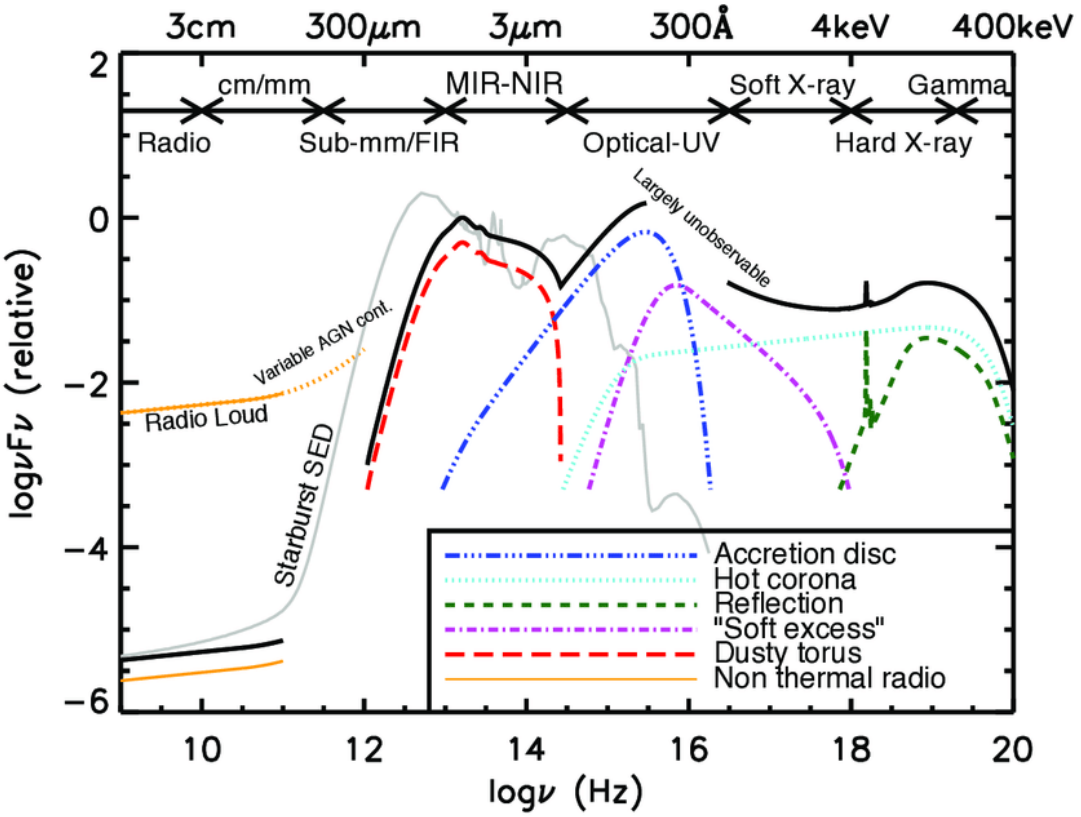

Figure 1.3: A Schematic representation of the AGN SED derived from radio-quiet Type 1 AGN taken from Harrison et al. (2014). The solid black line is the total AGN SED, and the coloured lines (offsets not to scale) represent the emission from different processes associated with physical components. Also shown in grey is an example radio–UV SED of a starburst galaxy.

et al. (2014).

The current paradigm of the radiative mode model, shown in Figure 1.1, is of a central SMBH surrounded by a cool, geometrically thin, and optically thick accretion disc perpendicular to the spinning axis. This accretion disc has a thermal gradient and emits ultraviolet (UV) in the hottest regions around the SMBH and Infrared (IR) at larger radii, where the disc is cooler. The emission from the accretion disc is shown as the dark blue line in Figure 1.3 and is typically the peak of AGN emission; this peak is often referred to as the "big blue bump". The accretion process may also drive radio jets, which emanate along the spin axis on parsec scales. This gives rise to two different radio-loud and radio-quiet populations based on whether a jet is formed. The detected radio emission can, therefore, vary by many orders of magnitude between AGN, as shown by the orange line in Figure 1.3.

Magnetic reconnection within the accretion disc gives rise to an optically thin, hot corona on scales of a few gravitational radii. Photons from the disc are then inverse Compton scattered by electrons into the X-ray range with a power-law distribution, shown as a light blue line in Figure 1.3. Encompassing the accretion disc on scales of thousands of gravitational radii, there is a dense ($n_e \gtrsim 10^8$ cm^{-3}; Osterbrock & Ferland 2006) cloudy region of dust-free gas with high orbital velocities (1000 - 25,000 km s^{-1}; Peterson 2006) that undergoes photoionisation by UV photons. This results in high emission rates at specific wavelengths, thus producing emission lines in the spectra. The high orbital velocities Doppler broaden these emission lines, hence, this region is referred to as the broad line region (BLR). At parsec scales perpendicular to the plane, the gas has significantly lower densities $n_e \gtrsim 10^6$ cm^{-3} and velocities (order of 100 km s^{-1}). Due to the lower velocities, the emission lines produced by photoionisation remain narrow in this region; thus, it is referred to as the narrow line region (NLR). The low densities of this region result in low collision rates between atoms/ions, which can allow for the emission of forbidden lines.

In the plane of the disc at parsec scales, the system is enshrouded by an axisymmetric, geometrically thick dusty toroidal structure with an inner radius at the dust sublimation limit. The torus is also optically thick to much of the emission from the central regions, re-emitting UV-optical photons as IR, shown

by the red line in Figure 1.3. The internal structure of the torus is still a matter of debate, with different models predicting clumpy (Dullemond & van Bemmel, 2005; Nenkova et al., 2008b,a) or continuous (Pier & Krolik, 1992; Fritz et al., 2006) structures. Both cases may exist, potentially simultaneously (Assef et al., 2013); however, most AGN tori are assumed to be clumpy. The X-rays produced by the corona may also reflect off the torus and the accretion disc to produce an extra bump in the X-ray region of the SED, shown in green in Figure 1.3.

The obscuring torus is a fundamental component of the unification model, as the inclination angle to the observer determines which regions are observed; this is demonstrated in Figure 1.1. Light from the inner regions of the AGN, comprising the accretion disc, corona, and BLR, will be obscured to an observer with a viewing angle along the plane of the torus. This case is referred to as a Type 2 AGN and is characterised by the NLR, which extends beyond the torus and remains observable. However, broad lines have been detected in the polarised spectra of Type 2 AGN (Antonucci, 1984; Du et al., 2017), which is key evidence for the unification model, as it demonstrates there is an obscured BLR. A Type 1 AGN is seen when an observer is viewing closer to the polar axis of the AGN and has an unobscured view of the internal structure and emissions. The unobscured view of the BLR is the most notable characteristic of Type 1 AGN. Observationally, the distinction between Type 1 and Type 2 appears more complex as there is evidence that the obscured AGN fraction is a function of AGN luminosity and potentially of redshift, host properties and local environment (Treister & Urry, 2006; Mayo & Lawrence, 2013; Merloni et al., 2014; Hickox & Alexander, 2018).

The jet mode is characterised by a lower accretion rate and radiative efficiency than in the radiative mode. The main energy output in the jet mode is kinetic outflows of matter; see Heckman & Best (2014) for a review. In the jet mode model, shown in Figure 1.2, the accretion disc is replaced by a hot, optically thin, and geometrically thick structure with an advection-dominated accretion flow. However, at larger radii, beyond the direct accretion region, a standard accretion disc may still be present. This accretion mode also gives rise to two-sided jets. The BLR is absent in this mode, while there may be a weak NLR, and the extent to which there is a dusty torus is unclear. However, this is just a specific

mode of the same fundamental structure. Simulations and now observations have shown there is a collapse of the accretion disc at low accretion, and AGN can move between the different modes at $L_{\rm Edd} \approx 0.02$ (Yuan & Narayan, 2014; Hagen et al., 2024).

1.1.2 AGN Identification Methods

AGN are extreme objects that can produce unique signatures and powerful emissions across the electromagnetic spectrum, which cannot be explained by other mechanisms. See the comparison between a star-forming galaxy and an AGN in Figure 1.3. The most luminous unobscured AGN dominate the flux of the host galaxy and are easily detectable at most wavelengths, while lower luminosity AGN in highly star-forming galaxies are significantly harder to distinguish. AGN and their host galaxies cover a broad parameter space, and different selection methods can be biased towards different population subsets (Aird et al., 2012; Trump et al., 2015; Ji et al., 2022; Powell et al., 2024). Understanding AGN requires consideration of the entire population; thus, a large variety of selection methods have been developed. Some methods that are relevant to this work are outlined below.

1.1.2.1 Continuum

X-ray emission is a near-ubiquitous signature of AGN, with most known AGN having X-ray detections. X-ray photons (especially high energy ones, i.e., 2 keV) typically pass through the torus, meaning X-ray selection is significantly less affected by inclination angle. However, if the dusty torus is Compton thick (column density of $N_e > 1.5 \times 10^{24}$ cm^{-2} ;Kocevski et al. 2015) or if there is a Compton thick region in the line of sight of the observer, the X-ray detection may be missed (Treister et al., 2004; Daddi et al., 2007; Alexander et al., 2008).

The most reliable X-ray indicator of an AGN is $L_{2-10\ \rm keV} > 10^{42}$ erg s^{-1}, as it is associated with an exceptionally hot and energetic environment, and it is exceedingly rare for other sources of X-rays, such as star formation, to surpass such luminosities (Ranalli et al., 2003). However, not all AGN produce X-rays

at such luminosities, and some sources can be obscured. Therefore, this method is heavily biased against lower luminosity and heavily obscured AGN, which are significantly more likely to have lower masses. As a result, most solely X ray detected AGN have $M_{BH} > 10^7$ $M_\odot$ (Brandt & Alexander, 2015). However, X-ray data can be used in conjunction with data at other wavelengths (e.g., O'Sullivan et al. 2001; Steffen et al. 2006; Persic & Rephaeli 2007; Lehmer et al. 2010; Wang et al. 2013).

A significant amount of light is reprocessed in the torus into IR; therefore, IR observation can be a useful AGN selection tool. As shown in Figure 1.3, star-forming galaxies produce similar amounts of IR to AGN; however, due to the different temperature regimes, the slope of the SED in IR is reasonably different and can thus be used in AGN selection. For example, the Edelson & Malkan (2012) catalogue is constructed using infrared colours from the Wide-field Infrared Survey Explorer (WISE; see Wright et al. 2010a) and the Two Micron All-Sky Survey (2MASS; Skrutskie et al. 2006), as well as the distance from an X-ray source in the ROSAT All-Sky Survey (RASS; Voges et al. 1999). Edelson & Malkan (2012) used the uniqueness of the power-law in the near-to-mid-IR of AGN SEDs and the near ubiquity of X-ray detection in AGN to predict the likelihood that a source is an AGN.

1.1.2.2 Optical Emission Line Ratios

A key aspect of AGN is the creation of forbidden emission lines, which are produced by the emission from electrons in long-lived orbitals. The low density of the NLR means that the emission time is shorter than the collision time, a condition not met in most other environments. Although the production of these forbidden lines is not exclusive to AGN, the relative intensity, due to the hardness of the AGN continuum (i.e., out to higher energies), is different enough from other sources, such as O-type stars, to distinguish the AGN.

This was first utilised for classification by Baldwin, Phillips & Terlevich (1981), who used flux ratios between high-excitation emission lines (forbidden) and ordinary emission lines on diagrams now known as BPT diagrams to classify different driving mechanisms. Figure 1.4 shows a BPT diagram from Moiseev &

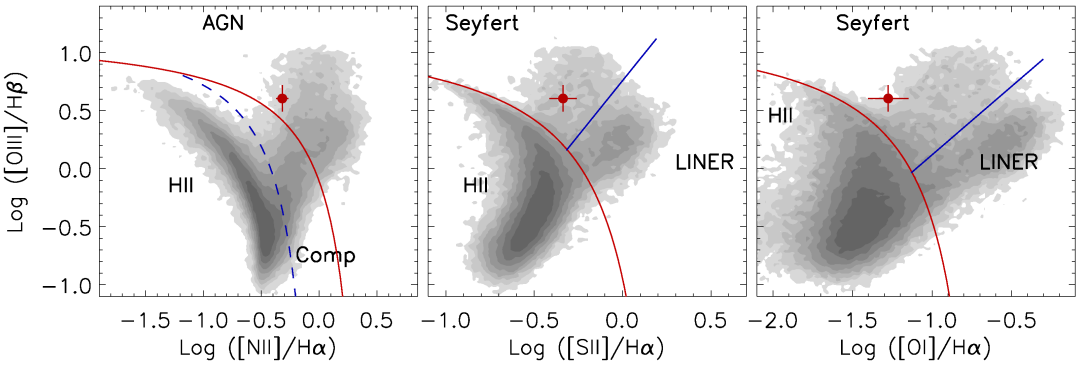

Figure 1.4: A set of diagnostic diagrams taken from Moiseev & Smirnova (2023). The separation between star-forming galaxies and AGN is mostly done using panel a, whereas panels b and c can be used to separate Seyferts from LINERs.

Smirnova (2023) and based on Kewley et al. (2006). The far left plot uses the [OIII]5007/Hβ and [NII]6584/Hα line ratios to distinguish between star formation and AGN-driven line ratios. The objects populating the left and right extremities of the populations represent star formation and AGN-dominated systems, respectively (Kauffmann et al., 2003). However, a significant population of galaxies host both star formation and AGN, so they occupy a composite region. The red boundary sets the theoretical upper limit for star formation from photoionisation and stellar population synthesis models. The other two panels can be used to separate Low-Ionisation Nuclear Emission Line Regions (LINERs) and AGN. LINERs are objects that have properties similar to the NLR of AGN, but with lower luminosities (Heckman, 1980). There is no consensus on the driver mechanism of LINERS. However, some are likely driven by star formation, and others by low luminosity AGN (Heckman & Best, 2014; Coldwell et al., 2018). Due to this ambiguity, many studies remove LINERs from their AGN sample in order to obtain a less contaminated sample of AGN (Garland et al., 2024).

1.1.2.3 Broad Lines

Another AGN selection technique is based on searching for broad emission lines in the optical spectra, which are defining features of AGN accretion. The velocity of the BLR can be measured from the full–width–half–maximum (FWHM) of

the broad emission lines in the 1D spectrum. The most massive SMBHs can have broad emission lines of FWHM > 10000 km s^{-1}, much higher than the broad lines typically produced by star-forming regions and shocks, while low-mass AGN has been measured at a few hundred km s^{-1}, which are of similar order to non-AGN processes. A frequently used threshold for selecting Type 1 AGN is FWHM$_{H\beta} > 1000$ km s^{-1} (Hao et al., 2005; Schneider et al., 2010; Oh et al., 2015). However, this cut is biased against lower-mass BHs, which have lower values of FWHM and low-luminosity AGN, where the broad lines do not sufficiently dominate the spectra. To select the lower-mass and luminosity AGN from broad lines, which may be dominated by stellar emission, detailed modelling techniques for stellar emission features have been created, which allow for the removal of the host continuum from the spectra (Hao et al., 2005; Greene & Ho, 2007). Therefore, to construct more complete samples, a lower limit on FWHM can be selected with constraints on the goodness of the fit. For example, Reines & Volonteri (2015) used a lower limit of 500 km s^{-1}, while Liu et al. (2019) set no lower limit. One caveat of this technique is the contamination from stellar winds, which also broaden emission lines; this can be somewhat mitigated by additional selection, such as BPT diagrams. Due to the requirement of broad emission lines, this method excludes Type 2 AGN. This needs to be considered in the selection biases, as there may be differences between the host properties of Type 1 and Type 2 AGN populations (Zou et al., 2019).

1.1.3 AGN Luminosity and Accretion

As mentioned previously, the extraordinary luminosities associated with the SMBHs gave rise to debate about their origin. The continuum produced is inconsistent with a simple isotropic blackbody emission, and the highly collimated jets indicate a single source. The only model that accounts for all of these is an accreting SMBH (Salpeter, 1964; Lynden-Bell, 1969).

The most simple model of AGN accretion is a spherically symmetric inflow down the gravitational potential well, with potential energy released as EM radiation. Assuming a fully ionised gas, the radiation will transfer momentum through

Thomson scattering, creating radiation pressure. Therefore, this model of accretion is limited when the radiation forces are equal to the gravitational forces; this is known as the Eddington limit and can be written as:

$$F_{rad} = \frac{L_{Edd}\sigma_T}{4\pi r^2 c} = F_{grav} = \frac{GM_{BH}(m_p + m_e)}{r^2} \tag{1.1}$$

where L_{Edd} is the luminosity at this limit and is known as the Eddington luminosity, r is the distance from the SMBH, σ_T is the Thomson cross section for the interaction of photons with electrons, c is the speed of light, and m_p and m_e are the proton and electron masses. This can be rearranged to give the Eddington luminosity:

$$L_{Edd} = \frac{4\pi G c M_{BH} m_p}{\sigma_T}. \tag{1.2}$$

The luminosity of the AGN is related to the accretion rate and can be expressed as:

$$L_{Bol} = \nu \dot{M} c^2, \tag{1.3}$$

where L_{Bol} is the bolometric luminosity, which is the total luminosity across the electromagnetic spectrum. $\dot{M}$ is the accretion rate, c is the speed of light, and ν is a mass-energy efficiency conversion factor, known as radiative efficiency. The value of ν varies across different AGN and is strongly dependent on BH spin (Thorne, 1974). Spin is a term used to describe the angular momentum associated with a BH (Kerr, 1963). As angular momentum is conserved, the spin of a BH can be impacted by the direction and alignment of accretion in relation to the spin axis of the BH. As the spin increases, the radius of the last stable orbit decreases, which increases radiative efficiency (Thorne, 1974). Therefore, the fuelling mechanism of an AGN (see Section 1.4) can impact the spin and radiative efficiency of an AGN (Smethurst et al., 2019; Beckmann et al., 2024).Typical values of ν range from 0.05 to 0.42 (Thorne, 1974). For most studies, the average value of $\nu = 0.1$ is used. However, higher values are used if the spin nature of the SMBH is known.

A frequently used value is the Eddington ratio λ, which is the ratio between bolometric luminosity and Eddington luminosity and is given as:

$$\lambda = L_{Bol}/L_{Edd} \tag{1.4}$$

This ratio is used to show how close an AGN is accreting to the Eddington limit. Most AGN only accrete at a few per cent of Eddington (Aird et al., 2018), with AGN at $\lambda > 0.1$ being known as high-accretion AGN. The accretion of gas and the emission of radiation is not isotropic, thus AGN can exceed the Eddington limit. These super-Eddington AGN have been invoked to explain the extremely high mass AGN found in the early universe (Haiman et al., 2004; Madau & Rees, 2001; Li et al., 2008).

The most reliable way of determining bolometric luminosity is by measuring the luminosity across the entire EM spectrum and constructing an AGN SED. Observing AGN across numerous bands is extremely time-consuming and expensive. However, extensive studies of AGN spectra have found a remarkable similarity in shape across AGN (Sanders et al., 1989; Elvis et al., 1994; Richards et al., 2006b). Thus, it is possible to estimate the bolometric luminosity using one band; this is known as a bolometric correction and is written as:

$$L_{Bol} = K_{band} L_{Band} \tag{1.5}$$

where K_{band} is the bolometric correction and L_{Bol} and L_{Band} are the bolometric and band luminosities, respectively. Corrections have been determined for a large number of continuum wavebands and/or emission lines, such as X-ray, IR and 5100 Å (Netzer, 2019). It is important to note that these are derived from averages and empirical measurements and carry errors.

1.1.3.1 Black Hole Mass

Since SMBHs were first discovered, a number of different methods have been created that can measure or reliably estimate the mass of SMBHs. This section presents some of the methods which can be used to derive SMBH masses for both active and inactive SMBHs.

1.1.3.2 Direct measurement

One of the most direct methods of SMBH mass measurement is to use spatially resolved gas or stellar kinematics within the sphere of influence, where the SMBH mass accounts for roughly half the gravitational potential, to measure a dynamical mass. The stellar mass of the region is derived from mass-to-light ratios (M/L), and a dark matter component can be calculated by modelling the dark matter halo (Gebhardt & Thomas, 2009). The mass of the SMBH can then be determined by the discrepancy between mass measurements (Genzel et al., 1996; Ghez et al., 1998, 2008; Gillessen et al., 2009; Genzel et al., 2010).

Although resolving the sphere of SMBH influence is ideal, BH measurements can be made on scales larger than the sphere of influence. However, the increasing error with larger scales, along with the required resolution and depth for such measurements, presents a strong limiting factor (Gebhardt et al., 2003; Kormendy & Ho, 2013; Thater et al., 2017). This selection method may only be sampling a small demographic of the underlying SMBH and galaxy populations, biasing the results of population studies based on this method (Shankar et al., 2016). Furthermore, strong emission from the AGN continuum can dominate the stellar absorption features, making this method impractical for most AGN, so it is primarily used for inactive SMBH. However, the water megamaser method is a dynamical method for measuring BH mass in AGN host galaxies. This method is based on detecting water vapour emission at 1.3 cm (22 GHz) in the accretion disc of AGN at scales smaller than 1 pc (Miyoshi et al., 1995). However, this method has limitations such as the gas accretion disc being viewed edge-on.

1.1.3.3 Reverberation Mapping

Another direct and reliable method of estimating the mass of a SMBH is the reverberation mapping (RM) of the BLR, thus excluding Type 2 AGN. As mentioned previously, the BLR is within a few thousand gravitational radii and is thus kinematically dominated by the SMBH. Therefore, the mass of the SMBH can be measured using Newtonian physics (Czerny & Hryniewicz, 2011). The radius can be measured due to the variability of the accretion disc emission, which can be seen in the emission of the BLR after a travel-time delay (Blandford &

McKee, 1982; Peterson, 1993; Wandel, 1999). The time delay is typically measured in emission lines. However, it can also be achieved with continuum emission (Kovačević et al., 2022; Pozo Nuñez et al., 2023). As mentioned in Section 1.1.1, the high orbital velocity of the BLR region broadens emission lines through the Doppler effect. Since this is directly related to velocity, the width of the broad lines, typically Hβ and Hα, can be used to determine velocity. Thus, the formula for SMBH mass is typically given as:

$$M(r) = f\frac{W^2 R_{BLR}}{G}, \tag{1.6}$$

where W is the width of the broad emission line, R_{BLR} is the radius of the broad line region and G is the gravitational constant. The additional factor f is added to correct for the fact that the velocity derived from the broad line does not directly translate to the true velocity of the BLR. The broad-line velocity measurement is affected by the geometry, structure, and kinematics of the BLR, as well as the inclination angle of the AGN. To account for this, the f coefficient is applied (Onken et al., 2004; Park et al., 2012), which is derived from scaling the mass in the $M_{\rm BH}-\sigma$ relation from RM to match the relation derived from direct dynamical measurements. Importantly, individual AGN have different corrections depending on their properties and inclination, and the $M_{\rm BH} - \sigma$ relation has a significant intrinsic scatter. Therefore, the virial coefficient $\langle f \rangle$ is an average measurement for a population and is the main source of error in the BH mass measurements, with recent estimations suggesting an error of 0.3 dex and an f of 4.2 (Shen et al., 2023). Additionally, different galaxy types may require different corrections (Ho & Kim, 2014). Previous measurements have ranged from $\langle f \rangle = 2.8 - 5.9$ (Graham et al., 2011; Woo et al., 2013) as changes to the canonical $M_{\rm BH} - \sigma$ relation affect the result (Kormendy & Ho, 2013; Savorgnan & Graham, 2016) see Section 1.4.1.1. However, when high-quality spectrophotometric monitoring data is available the orientation and structure of the BLR can be constrained, removing the requirement of a scaling factor (Pancoast et al., 2011; Grier et al., 2013; Pancoast et al., 2014).

1.1.3.4 Single-epoch virial estimation

A significant advancement in AGN mass estimation comes from RM studies and the revealing of a tight relation between the monochromatic luminosity of the AGN, typically at 5100 Å (Kaspi et al., 2000; Bentz et al., 2013) and the size of the broad line region. This likely arises from the dust sublimation limit, which is related to the rate of arrival of ionising photons, marking the transition between the BLR and the torus (Netzer, 1993; Laor & Draine, 1993). This relation allows for single-epoch (SE) estimation of the BLR size and is the most widely used method for BH mass estimation. The SE mass estimation formula is usually given in the form:

$$\log\left(\frac{M_{\rm BH}}{M_\odot}\right) = a + b\log\left(\frac{L_{5100}}{10^{44}\ \rm ergs}\right) + c\log\left(\frac{\rm FWHM_{H\beta}}{\rm km/s}\right) \tag{1.7}$$

where a,b, and c are calibrated against the RM AGN coefficients; different works have given a range of values, with recent values from (Shen et al., 2023) being 0.85, 0.5 and 2. A variety of wavelengths can be used in the L-R relation, including X-rays and UV, when assuming a general AGN SED template. Certain line luminosities may also be used when there is significant contamination of stellar emission in the continuum (e.g., Greene & Ho 2005). However, the best wavelength is 5100Å with an estimated mass error of 0.35 dex Shen et al. (2023).

1.1.3.5 Scaling relations

Another widely used method are the BH mass-galaxy scaling relation; see Section 1.4.1 for a more detailed overview. These are typically used when other methods are not available, such as high redshift and large X-ray samples (Aird et al., 2012) and in predicting the stochastic gravitational wave background (Sesana et al., 2009; Sesana, 2013). However, there is no consensus on the most fundamental relation, the mass and morphological dependencies, or how they evolve with redshift.

1.2 Historical view of Galaxies

Besides the Milky Way, four galaxies are visible to the naked eye: the Andromeda and Triangulum galaxies, as well as the Milky Way's dwarf satellite galaxies, the Large and Small Magellanic Clouds. While these galaxies were likely first observed many millennia ago, the first recorded observation was of the Andromeda galaxy by Abd al-Rahman al-Sufi in 964 (Hafez, 2010). It was classed as a "small cloud" and similar observations in the age of telescopes gave rise to the term nebula for extended cloudy objects in the night sky (Messier, 1781; Herschel, 1786; Dreyer, 1888). At the time, these objects were not well understood, and it was believed that the universe consisted solely of the Milky Way galaxy. However, there was some speculation that these nebulae were, in fact, their own universes separate from our own (Kant, 1755), and were dubbed island universes. There was so much contention over this theory it became known as the Great Debate and famously resulted in an actual debate between Shapley and Curtis on whether these structures were external and on the same scales as the Milky Way or small structures within it. It was not until the measurements of Cepheid variable stars, which follow a tight luminosity-period relation in Andromeda by Hubble (1926), that the concept of external galaxies was broadly accepted.

1.3 Galaxy Structure and Morphology

Early observations revealed a variety of different galaxy shapes and structures, and astronomers began to classify them into different categories for statistical studies. The most famous early classification system was the Jeans-Hubble tuning fork, also known as the Hubble sequence (Hubble, 1926, 1936).

This diagram attempted to construct a simple yet comprehensive morphological sequence and is shown in Figure 1.5. The sequence begins with spherical galaxies, also known as elliptical galaxies. These were placed on the far left of the diagram and were labelled E, followed by a number based on the ellipticity from:

$$E = 10(1 - b/a) \tag{1.8}$$

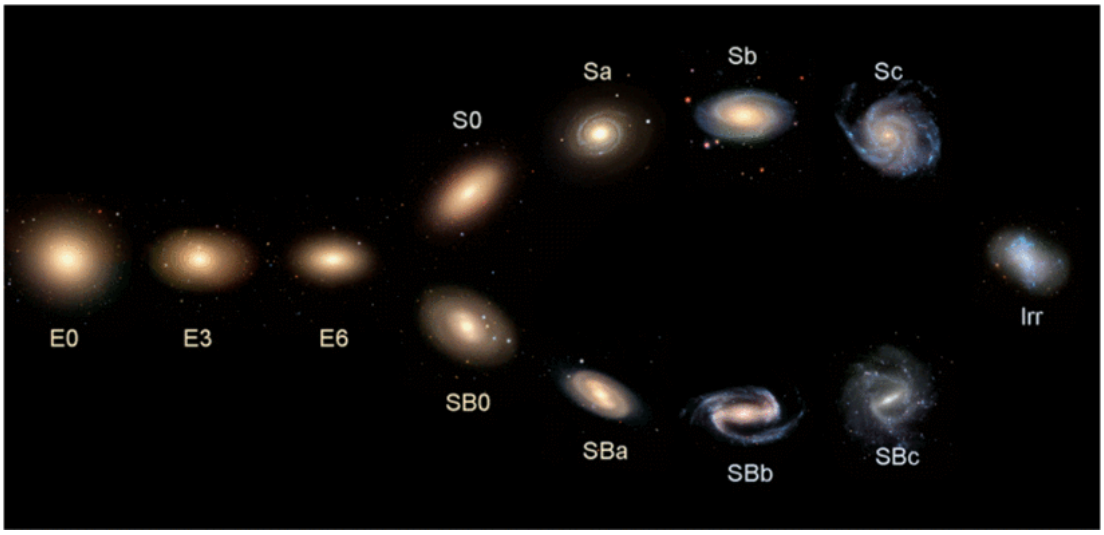

Figure 1.5: A diagram of the Hubble tuning fork. Early-type elliptical and lenticular galaxies are shown on the left-hand side of the diagram, late-type spirals lie on the right and are split into barred and unbarred galaxies, while irregular galaxies are to the far right. Figure from Cui et al. (2014)

where a is the length of the major axis and b is the length of the minor axis; E0 would be a purely spherical galaxy. Going right on the diagram increased the ellipticity value to show oblate spheroids. This led to the classification of S0 galaxies, which had a disc-like morphology but appeared more like the spheroids in internal structure. Further to the right on the sequence is the spiral section of the diagram, which was split into two, where unbarred galaxies were S-type and barred galaxies were SB. Both of these spiral types had subclasses of a, b, and c, based on the relative dominance of the bulge, the winding angle, and the resolution of spiral arms. The sequence was also divided into early-type galaxies (ETGs), corresponding to elliptical galaxies and late-type galaxies (LTGs), corresponding to spiral galaxies. This classification was based on the early/late-type nomenclature to describe complexity in stellar spectral classification and was not intended to convey any temporal connotations.

Beyond physical structure, another classifier that categorises galaxies is optical colour. Early large-scale surveys found galaxies largely fell within two populations: one characterised by high mass and red colours, known as the red sequence (old stellar population), and one by low mass and blue colours (young stellar population), known as the blue sequence (Baldry et al., 2004; Willmer et al., 2006; Brammer et al., 2009). Only a minority of observed galaxies fall between the two populations, in a region known as the green valley. This colour bimodality has been suggested as a method to predict morphology, as two populations also loosely map to the LTG and ETG categories, with LTGs typically populating the blue sequence and ETGs the red sequence (Strateva et al., 2001; Bell et al., 2004). However, there are large populations of red spiral galaxies ($\approx 30\%$) and blue ellipticals ($\approx 10\%$) (Schawinski et al., 2009; Bamford et al., 2009; Masters et al., 2010; Rowlands et al., 2012; Mahajan et al., 2020). Therefore, as highlighted by Smethurst et al. (2022), colour is not a suitable proxy for morphology and catalogues constructed using it have low purity/completeness.

1.3.1 Large-Scale Structure and Galaxy Formation

The most widely accepted framework for explaining the formation and evolution of both large-scale cosmic structure and galaxies is the Λ-CDM cosmological

model. This model describes a flat universe (de Bernardis et al., 2000) in which the present-day energy density consists of roughly 4% baryonic matter, 26% dark matter, and 70% dark energy. The Λ-CDM framework was originally proposed on theoretical grounds (Peebles, 1984; Blumenthal et al., 1984) and later constrained observationally by measurements of the cosmic microwave background (Spergel et al., 2003; Bennett et al., 2013).

In this model, overdense regions of dark matter, formed from quantum perturbations in the early universe, collapse under gravity into dark matter halos. Through accretion and mergers, these halos grew and interconnected to create a network of filaments, sheets, clusters, and voids, collectively known as the large-scale structure of the universe. The baryonic matter in the universe then began to cool and collapse at the centres of dark matter halos. The baryonic matter clouds, mostly hydrogen and helium, further fragmented into rotating discs due to angular momentum conservation. Regions within these discs subsequently collapsed to form stars. Through mergers and secular processes, these proto-galaxies evolved into the diverse population of galaxies observed today. Large-scale hydrodynamical simulations of a standard Λ-CDM universe, with additional prescriptions for physical processes such as feedback (see section 1.4) (e.g., Horizon-AGN Dubois et al. 2014; EAGLE Schaye et al. 2015; McAlpine et al. 2016; Illustris Vogelsberger et al. 2014) have successfully reproduced both the large-scale structure of the universe and the broad statistical properties of galaxies.

1.3.2 Elliptical Galaxies

Elliptical galaxies are typically characterised by uniformity in the stellar population, negligible gas fraction, limited star formation, large stellar mass, red colour, and, most notably, dispersion-dominated structures (Djorgovski & Davis, 1987; Kormendy, 2016). The Λ-CDM model predicts the initial formation of rotation-dominated systems, which may grow via gas accretion and mergers. The process of a merger is an extremely chaotic event that can dramatically redistribute the angular momentum of a galaxy. Simulations have repeatedly shown that major mergers, typically defined as having stellar mass ratios greater than 1:4 between the secondary and primary galaxy, can drive rotation-supported systems into

dispersion-supported ones (Toomre, 1977; Walker et al., 1996; Kormendy & Kennicutt, 2004; Hopkins et al., 2012; Martig et al., 2012). The role of mergers is evident due to the observed relation between morphology and galactic environment. Galaxy clusters, which are groupings of at least 100 galaxies within the same dark matter halo, more violent merger histories and thus high fractions of elliptical galaxies when compared to galaxies in under-dense environments (Dressler, 1980; Bower & Balogh, 2004).

The loss of angular momentum may also cause the collapse and massive inflows of gas, triggering starbursts in gas-rich or "wet" mergers. This can exhaust the gas supply required for further star formation, quenching the post-merger remnant (Mihos & Hernquist, 1994, 1996; Hopkins et al., 2006; Hayward et al., 2014; Sparre & Springel, 2016). In gas-poor or "dry" mergers, there is no additional star formation and the inward spiralling of binary SMBHs may scour the core of the galaxy, depleting it of stars. These are known as core-Sérsic galaxies and are typically the most massive ellipticals, while galaxies with intact cores are known as Sérsic galaxies (Begelman et al., 1980; Graham, 2004; Merritt, 2006) (Sérsic profiles are discussed further in Section 1.3.4.1 below).

Another defining feature of elliptical galaxies is the relation between their stellar velocity dispersion, luminosity, and effective radius, which is known as the fundamental plane (Dressler, 1987; Djorgovski & Davis, 1987). Thus, this relation can be a constraint for models of elliptical formation. Mergers in galaxy and cosmological simulations have organically reproduced the fundamental plane for elliptical galaxies, further cementing the role of mergers in galaxy evolution (Bekki, 1998; Nipoti et al., 2003; Boylan-Kolchin et al., 2005; Robertson et al., 2006; Hilz et al., 2012; Taranu et al., 2015; Rosito et al., 2021).

1.3.3 Galaxies with Discs

One prominent feature of many galaxies is large-scale galactic discs, geometrically thin structures consisting of gas, stars, and dust in circular orbits along the same plane with limited dispersion (Binney & Merrifield, 1998). The formation of a thin rotating disc requires a smooth accretion of gas with the angular momentum vector always in the same direction. This smooth and slow accretion of

disc galaxies results in a slower and longer-lasting star formation rate, compared to mergers, putting most disc galaxies in the blue cloud. However, if the gas reservoirs are depleted, a galaxy can move to the red sequence (Masters et al., 2010; Lopes et al., 2016).

The majority of galaxies with discs also include a central bulge component, which can dominate the stellar mass distribution or only comprise a small fraction of the stellar mass. These bulges are often separated into two different categories: classical and pseudo-bulges (Kormendy & Kennicutt, 2004; Gadotti, 2009). Classical bulges are dispersion-dominated and share similar properties to elliptical galaxies, such as structure, colour and composition, whereas pseudo-bulges are rotation-dominated, bluer in colour, less concentrated surface-brightness profiles, geometrically flatter and are significantly more likely to host structures such as bars (Kormendy & Ho, 2013). The fact that classical bulges share similar properties to ellipticals and follow the same fundamental plane suggests a common evolutionary history, while properties of pseudo-bulges suggest a secular evolutionary history similar to discs (Kormendy & Kennicutt, 2004).

The stellar mass ratio between the bulge and the total stellar mass of a galaxy is known as the bulge-to-total ratio (B/T) and is believed to be linked to the dynamic evolution of the galaxies. If a system is dominated by mergers in its early evolution and consequently dispersion-dominated, it can evolve into a disc-dominated system through the smooth accretion of gas, and undergo no major mergers (Hopkins & Hernquist, 2009a; Emsellem et al., 2011; Pontzen et al., 2016; Sparre & Springel, 2017). Moreover, a disc-dominated galaxy can grow its classical bulge through minor mergers while not significantly impacting the kinematics of the outer disc (Kannan et al., 2015). The minimum mass ratio required for significant classical bulge growth is often routinely cited as 1:10 between the secondary and primary galaxy; however, it can depend on the specific parameters of the merger (Walker et al., 1996; Hopkins et al., 2012; Tonini et al., 2016). Using galaxy simulations, Martig et al. (2012) predicts that galaxies with a bulge-to-total ratio < 0.3 have not had any mergers above a mass ratio of 1:10 since $z \approx 1$ and are unlikely to have had one since $z \approx 2$, with the most disc-dominated galaxies not having any mergers since $z \approx 2$. However, some work has suggested that classical bulges may also be built up via secular processes

(Scannapieco et al., 2009; Sales et al., 2012; Bell et al., 2017; Park et al., 2019; Wang et al., 2019; Guo et al., 2020). The dynamical history inferred from the B/T ratio of pseudo-bulge galaxies is less clear. Although most agree pseudo-bulge evolution is dominated by secular processes, some simulations suggest pseudo-bulges can be formed via dynamical interactions (Guedes et al., 2013).

The determination of bulge type is thus greatly important in characterising a galaxy. However, the parameter space of pseudo and classical bulges overlap and both formation processes may be present in a galaxy. Therefore, simple classification methods carry an uncertainty. One of the most widely used photometric classifications is based on the Kormendy relation, which is a projection of the fundamental plane into mean surface brightness versus effective radius (Kormendy, 1977; Hamabe & Kormendy, 1987). The dividing line for a pseudo-bulge is typically given as 1σ from the relation formed by elliptical galaxies, however, some pseudo-bulges do lie on the relation (Gadotti, 2009).

1.3.4 Disc Structures

There are several distinct internal structures within galaxies. These structures, which include spiral arms, clumps, lenses and bars, and rings, are believed to be formed through disc instabilities and galaxy interaction.

The stability of a disc is related to its mass distribution and velocity and has been parameterised in a number of ways. One way is the Toomre stability parameter (Q), defined in Toomre (1964):

$$Q = \frac{\kappa \sigma_r}{3.36 G \Sigma} \tag{1.9}$$

where κ is the epicyclic frequency, σ_r is the velocity dispersion in the radial direction from the centre, G is the gravitational constant and Σ is the disc surface density. A disc is defined as unstable and has the potential for bar formation when $Q < 1$. Another parameterisation is the ELN-criterion, ϵ, (Efstathiou et al., 1982), defined as:

$$\epsilon = \frac{V_{\max}}{\sqrt{G M_d / R_d}} \tag{1.10}$$

where $V_{\max}$ is the maximum rotational velocity, M_d is the total disc mass, and R_d is the scale length of the disc. In this criterion, the threshold for instability and potential structure formation is $\epsilon < 1.1$.

Spiral arms are prominent spiral structures composed of stars, gas, and dust, extending across the discs of many galaxies. It is generally accepted that spirals are variations in surface density and brightness driven by gravitational instabilities (Rix & Zaritsky, 1995). However, the exact nature and formation mechanism of spiral arms in galaxies is still an area of ongoing debate and research (Dobbs & Baba, 2014; Michikoshi & Kokubo, 2020; Sellwood & Masters, 2022). One of the main theories of spiral arms is that they are not fixed aggregations of material but long-lived density waves (Lindblad, 1960; Sellwood & Kahn, 1991). A notable feature of spiral arms is the high star formation rate within the arms. However, it is unclear if spiral arms trigger star formation or condense it into a smaller region as studies comparing specific star formation rate (sSFR) and star formation efficiency (SFE) for the arm and inter-arm regions have found mixed results (Rebolledo et al., 2012; Moore et al., 2012; Hart et al., 2017; Querejeta et al., 2024; Sun et al., 2024)

Galaxy clumps are structures within galaxies that are denser and more star-forming than their surrounding regions. Most clumps likely form within gas-rich "marginally stable" galaxies where $Q \approx 1$ (Bournaud et al., 2014; Mandelker et al., 2014), while some clumps may be the remnant of an accreted lower mass galaxy (Mandelker et al., 2014; Zanella et al., 2019). It has also been suggested that the migration of clumps due to dynamical friction can contribute to galaxy bulge growth (Saha & Cortesi, 2018) and drive inflows (Bournaud et al., 2011), which could also fuel AGN.

Bars are elongated structures that almost ubiquitously extend from the central region of the galaxy and are present in a significant fraction of disc galaxies. The prominence of bars in galaxies is diverse; they can range from containing a small fraction of the stellar mass in a galaxy to the majority (de Vaucouleurs, 1959, 1963). One possible mechanism for the formation of bars is the spontaneous formation from gravitational instabilities in the disc, which redistributes the angular momentum. These gravitational instabilities can arise from purely

secular mechanisms and have been shown to form stable bars in simulations (Polyachenko, 2013). Simulations have also shown that the redistribution of angular momentum from tidal interactions and minor mergers can trigger bar formation (Noguchi, 1987; Gerin et al., 1990; Elmegreen et al., 1991; Miwa & Noguchi, 1998; Lang et al., 2014). Observationally, the picture is less clear, with studies finding contradictory results in regard to the correlation of bar presence with environment (Lin et al., 2014; Casteels et al., 2013). However, controlling for stellar mass, Méndez-Abreu et al. (2012) found that tidally-induced bar formation is dependent on host stellar mass, with bar formation being limited in low-mass galaxies and enhanced in massive galaxies following interactions.

The main epoch of bar formation is suggested to be around $z \approx 0.70-1$, which is after the peak of mergers (Lotz et al., 2011) and when galaxies became dynamically colder and more disc-dominated (Kraljic et al., 2012; Melvin et al., 2014; Simmons et al., 2014). However, bars are detected at higher redshift (Costantin et al., 2023; Guo et al., 2023), with Le Conte et al. (2024) reporting a bar fraction of 14% at $z = 2-3$ using the James Webb Space Telescope (JWST). Simulations suggest that bars are long-lived structures (Kraljic et al., 2012; Rosas-Guevara et al., 2020). This is backed up by observation, for example: de Sá-Freitas et al. (2023) report a bar's age to be 7.5 Gyrs old.

Observationally, bars are typically split into two different categories, strong and weak bars. There is no strict definition of what constitutes a strong or a weak bar; bar size is a continuous population (Géron et al., 2021), and classifications are often subjective Athanassoula & Bosma (2003). One definition given by (Nair & Abraham, 2010) is that a bar is strong if it dominates the light distribution of the galaxy, while a weak bar constitutes a small fraction of it. Measures of bar ellipticity and the boxiness of the bar isophotes have been used to separate the bar categories (Athanassoula, 1992a; Abraham & Merrifield, 2000; Laurikainen & Salo, 2002; Erwin, 2004; Gadotti, 2011).

The bar fraction in disc galaxies has been found to vary depending on the wavelength and classification method. Studies using optical data have reported bar fractions of around 23%-52% (Marinova & Jogee, 2007; Barazza et al., 2008; Aguerri et al., 2009; Masters et al., 2011; Buta et al., 2019). Part of the discrepancy likely arises from difficulty in the identification and classification of small

bars. Furthermore, observations made in the infrared, which is less affected by dust absorption, have reported fractions of up to 70% with the highest fractions typically observed using Spitzer on very nearby galaxies, benefiting from higher resolution (Eskridge et al., 2000; Knapen et al., 2000; Erwin, 2018).

The importance of bars comes from their ability to transfer angular momentum from the centre outwards. This traps more stars into bar orbits, which increases the strength of the bar (Sellwood, 1981; Athanassoula & Bosma, 2003; Athanassoula et al., 2013). This process also funnels gas along the bars into the centre, causing an increase in the central mass concentration (CMC) and depleting the galaxy gas content at larger scales (Athanassoula, 1992b; Spinoso et al., 2017; George et al., 2019). The increase in CMC can lead to starbursts and potentially fuel AGN, see Section 1.4 for more on the AGN-bar connection. The impact of a bar on a galaxy is likely dependent on the size of the bar. Géron et al. (2021) found that strong bars facilitate quenching while weak bars do not.

Galaxy rings are circular or elliptical structures of gas, stars and dust and most are believed to be formed through resonances where the orbital frequencies of stars and gas synchronize with the pattern speed of a galactic bar or spiral arm (Buta & Combes, 1996; Buta, 2017). In some cases, they can also be formed through mergers (Lynds & Toomre, 1976).

1.3.4.1 Measuring Galaxy Structures

Beyond visual and colour classifications of galaxies, the spatial distribution of light in galaxies and their components can be quantified using a parametric function, such as Sérsic (1968) profiles. The Sérsic profile can be expressed as an intensity profile in the form:

$$I(r) = I_e \exp\left[-b_n \left\{\left(\frac{r}{r_e}\right)^{1/n} - 1\right\}\right] \tag{1.11}$$

where $I(r)$ is the intensity at radius r, I_e is the intensity at the effective radius r_e, which encloses half the light, n is the Sérsic index that determines the shape of the light profile, and b_n is a constant depending on n. Figure 1.6 shows the shape of the light profile as a function of the Sérsic index n.

Different galaxy structures have different mass distributions and, consequently, different light distributions. Thus, fitting multiple Sérsic profiles to a galaxy can measure their relative contributions. The fitting of Sérsic profiles is often done using 2D image fitting tools which employ error-minimisation/optimisation to fit profiles (e.g., GIM2D:Simard et al. (1999, 2002); GALFIT: Peng et al. (2002, 2010); IMFIT: Erwin (2015); lenstronomy: Birrer & Amara (2018); Galight:Ding et al. (2021)) and have been shown to produce robust results. See Chapter 4 for a more detailed breakdown of the fitting process.

Extensive work has found that the discs of galaxies follow exponential profiles (Kormendy, 1977; Kent, 1985; Weiner et al., 2001; Simard et al., 2011). A Sérsic index of $n = 1$ follows an exponential distribution and is thus routinely used to fit the disc components of galaxies (Allen et al., 2006; Simmons & Urry, 2008). However, the exact reason why the discs of galaxies follow an exponential profile so closely is still a matter of debate (Elmegreen et al., 2005; Bournaud et al., 2007; Dutton, 2009; Vera-Ciro et al., 2014; Herpich et al., 2017; Wu et al., 2020; Wang & Lilly, 2022).

Higher Sérsic indices become increasingly associated with dispersion-supported structures such as classical bulges and elliptical galaxies. Many studies fix the Sérsic index of these structures to $n = 4$, which follows a de Vaucouleurs profile (de Vaucouleurs, 1948). However, classical bulges and elliptical Sérsic indices can typically range from $3 \lesssim n \lesssim 8$. Therefore, many studies set the Sérsic index for bulges as a free parameter (Graham, 2001; Ravindranath et al., 2004; Graham & Scott, 2013).

As pseudo-bulges are disc-like, they typically have Sérsic indices of $\approx 1 - 2$. Many studies have found that a cut at $n = 2$ is sufficient to separate most pseudo and classical bulges. However, there is a significant overlap in the measured Sérsic index of classical and pseudo-bulges due to the natural distribution as well as measurement errors (Fisher & Drory, 2008; Gadotti, 2009).

The light profile of a galaxy bar typically has a flatter central profile that quickly truncates at higher radii and is often fit with a Sérsic index of 0.5 (Peng et al., 2002; Gadotti, 2009) (also known as a Gaussian profile) but can range between $0.2 \lesssim n \lesssim 0.8$ (Kruk et al., 2018). Extra structures such as spiral arms

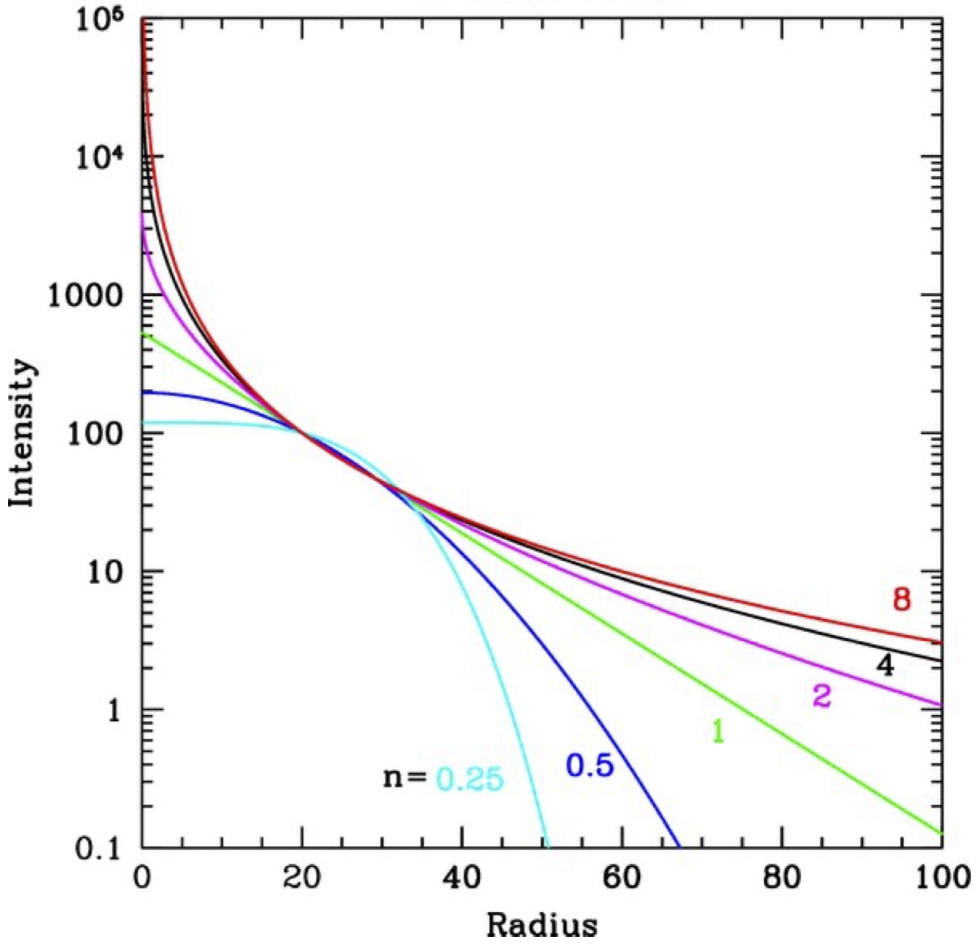

Figure 1.6: The Sérsic function for a range of Sérsic indices, for a constant R_e and I_e (Peng et al., 2010).

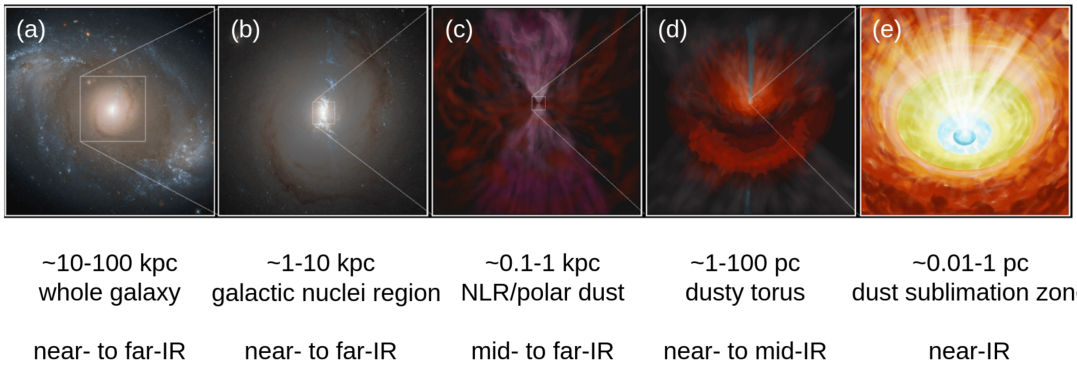

Figure 1.7: Illustration showing the scale of different components for AGN host galaxies and their contribution to the IR emission. Taken from Lyu & Rieke (2022)

and rings can also be fit but require more complex functions involving Fourier modes and truncation function (Peng et al., 2010).

Many studies also fit galaxies with a single Sérsic profile, regardless of morphology. Studies have found that a Sérsic index of $n = 2$ is suitable to separate bulge- and disc-dominated galaxies (Gadotti, 2009). This can be useful for images with lower-resolution data where multi-component fitting is less reliable. However, the relation has a significant scatter and can only be used as a binary estimation. This estimation of bulge/disc dominance has also been used as a proxy for early- and late-type galaxies (Zhuang & Ho, 2023). However, early-type galaxies can have significant disc structures (Kormendy & Richstone, 1995; Cappellari et al., 2011), and there is uncertainty in the relationship between the Sérsic index and B/T ratio. Thus, single Sérsic classification should be used with caution (Vika et al., 2015).

1.4 SMBH-Galaxy Co-evolution

SMBHs and galaxies exist on completely different spatial and mass scales. The accretion disc of an AGN typically has radius on scales less than a parsec, whereas the host galaxy's effective radius may be on the order of 10^5 parsecs. Figure 1.7 depicts the difference in SMBH and galaxy scale. Therefore, it seems unlikely that an AGN can impact a galaxy on a global scale. However, simple calculations

can show the energy released by the AGN accretion process is many times the binding energy of the host galaxy (Fabian, 2012). The binding energy of an elliptical galaxy (E_{gal}) can be approximated as:

$$E_{gal} \approx M_{gal}\sigma^2 \tag{1.12}$$

where M_{gal} is the total galaxy mass and σ is the velocity dispersion of the galaxy, while the energy released over the lifetime of a BH can be given by:

$$E_{bh} = \nu M_{bh}c^2 \tag{1.13}$$

where ν, the radiative efficiency, is typically taken to be 10%. Therefore, assuming a mass ratio of 0.001 between the SMBH and host galaxy, the ratio between energy released and binding energy can be given by:

$$\frac{E_{bh}}{E_{gal}} = (\frac{c}{\sigma})^2 10^{-4} \tag{1.14}$$

The average velocity dispersion of an elliptical galaxy is ≈ 200 km s^{-1}. Thus, for a typical galaxy, the energy released by an AGN is enough to unbind it ≈ 200 times over. Therefore, only a tiny fraction of the energy released has to be transferred into the baryonic content of the galaxy to have a significant impact on galaxy evolution. For example, for star formation to take place, cool gas needs to reach a critical density. However, if energy is imparted into the gas through expelling or heating gas, star formation can effectively be shut down (Croton et al., 2006; Rosario et al., 2013; Heckman & Best, 2014; Hopkins et al., 2016). This process is known as AGN feedback and is typically split into two different modes: the quasar/radiative mode and the kinetic/jet mode, driven by the two modes of AGN accretion described in Section 1.1.1. AGN feedback can also enhance star formation by compressing cold gas through outflows (Ishibashi & Fabian, 2012; Silk, 2013; Zubovas et al., 2013; Combes, 2017), while supernova feedback can limit the gas supply to the nuclear region via the injection of turbulence or by depleting the gas reserves (Schartmann et al., 2009; Hopkins et al., 2016).

The first suggestion that AGN feedback is a process that shapes the evolutionary history of galaxies comes from early simulations of galaxy formation based on the Λ-CDM models. The luminosity and mass function of galaxies from these early simulations were irreconcilable with observational measurements, as they significantly over-predicted the high and low ends of the distributions (Silk & Rees, 1998; Croton et al., 2006; Somerville et al., 2008). This indicated that there was a quenching process limiting galaxy star formation, particularly at the high- and low-mass ends of the distributions. This is illustrated in Figure 1.8, taken from Silk & Mamon (2012). At the low-mass end, supernova feedback is invoked as the main quenching mechanism (Dekel & Silk, 1986; Powell et al., 2011, although there is some evidence that AGN may also play a role in quenching dwarf galaxies; Kaviraj et al. 2017). However, the gravitational potential well of massive galaxies is too strong for stellar processes alone to quench a massive galaxy. Therefore, a more powerful mechanism, such as AGN feedback, is required. The incorporation of AGN feedback has thus been used numerous times in simulations to bring the high mass and luminosity ends of the functions into alignment with observations (Baugh et al., 1998, 2005; Kauffmann et al., 1999b,a; Somerville et al., 2001; Kitzbichler & White, 2006; Dubois et al., 2016)

Potential evidence of an evolutionary link between SMBHs and their host galaxies can be seen in the stellar mass growth histories of galaxies and the mass growth histories of SMBH. Observational studies have shown that the black hole accretion rate density (BHARD) and star formation rate density (SFRD) follow conspicuously similar trends. This can be seen in Figure 1.9, which shows that they both peak at around $z \approx 1 - 3$, with the bulk of their mass growth occurring around this epoch, with a downturn at later redshifts. This would be consistent with SMBH and galaxies influencing each other or sharing a similar fueling mechanism (Chapman et al., 2005; Silverman et al., 2009; Aird et al., 2010; Silk & Mamon, 2012; Wardlow et al., 2011; Simpson et al., 2013).

While there is strong theoretical evidence that AGN activity is linked to galaxy evolution, the role of AGN in quenching star formation is still observationally unclear. A number of conflicting studies have found that AGN hosts have enhanced (Koss et al., 2011; Shimizu et al., 2017), reduced (Schawinski et al., 2007; Silverman et al., 2008; Leslie et al., 2016; Lacerda et al., 2020) or typical SFRs

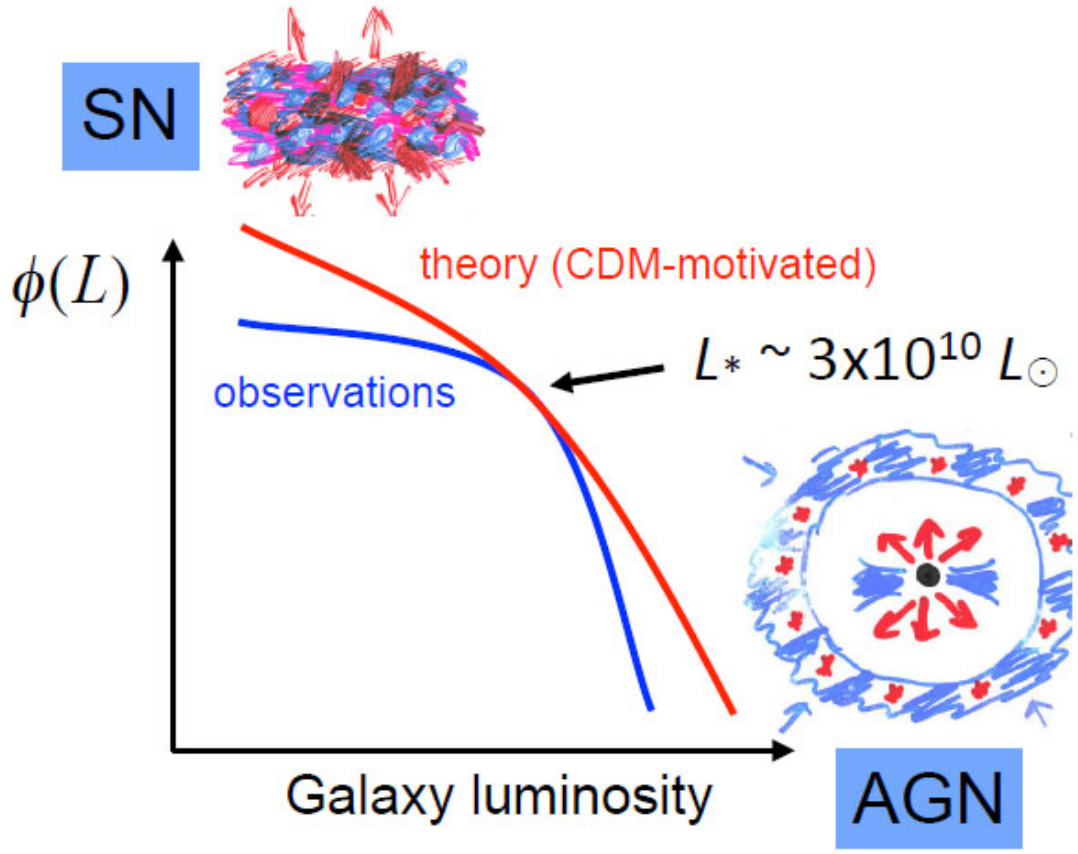

Figure 1.8: Cartoon showing the role of AGN and supernova feedback in shaping the observed galaxy luminosity function. Taken from Silk & Mamon (2012).

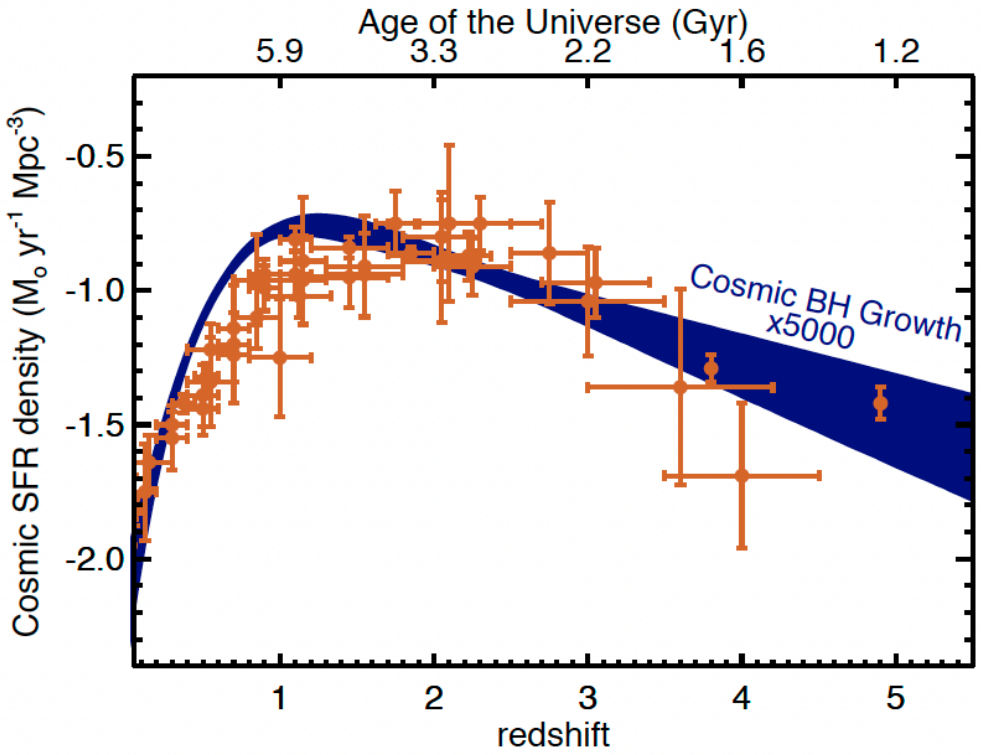

Figure 1.9: Volume averaged cosmic SFR density and BH mass accretion density as a function of redshift. The points are SFR density taken from Madau & Dickinson (2014) and the solid line is the X-ray derived BH mass accretion density taken from Aird et al. (2010) and is scaled by a factor of $\simeq 5000$. The similarity of their evolution suggests they are linked via some mechanism. Figure is taken from Harrison et al. (2014)

(Bongiorno et al., 2012; do Nascimento et al., 2019). Strong evidence comes from Smethurst et al. (2016) who found Type 2 AGN have recent rapid drops in their SFR and Lammers et al. (2023), who found that local AGN quenching the central SFR will have limited impact on global SFR. However, it should be noted that the different selection criteria in these studies may be sampling different sections of the diverse AGN population (Pouliasis et al., 2019).

1.4.1 Scaling relations

A significant amount of work was focused on understanding the co-evolution of SMBHs and their host galaxies, which has uncovered a number of different scaling relations between different properties (See Kormendy & Ho, 2013, for a review). However, as these relations are empirical, they are strongly affected by selection effects, sample size, and data quality. Thus, there is still strong debate over which relations are the most fundamental and how they evolve. Building a robust framework of this will provide important insights into what is driving the evolution of SMBH and galaxies across cosmic time.

1.4.1.1 Black Hole and Galaxy Velocity Dispersion

One of the most important BH-galaxy scaling relations is the $M_{BH} - \sigma$ relation, which relates the black hole's mass to the galaxy's velocity dispersion (Magorrian et al., 1998; Merritt & Ferrarese, 2001; Gebhardt et al., 2000; Tremaine et al., 2002; Gültekin et al., 2009; McConnell & Ma, 2013; Kormendy & Ho, 2013; Ho & Kim, 2014; Sahu et al., 2019b). An example of the $M_{BH} - \sigma$ relation is shown in Figure 1.10, taken from Sahu et al. (2019b) with M_{BH} plotted against σ. The $M_{BH} - \sigma$ relation provides important insights into co-evolution and is used to scale BH mass measurements. However, the origin and the slope of the $M_{BH} - \sigma$ relation have been subjects of significant debate. There are two theoretical explanations for the establishment of a relation, driven by the different modes of AGN feedback. The first explanation is based on the conservation of momentum (Fabian, 1999; Fabian et al., 2002; King, 2003, 2005). This scenario can be approximated by an Eddington-limited AGN driving the gas content of

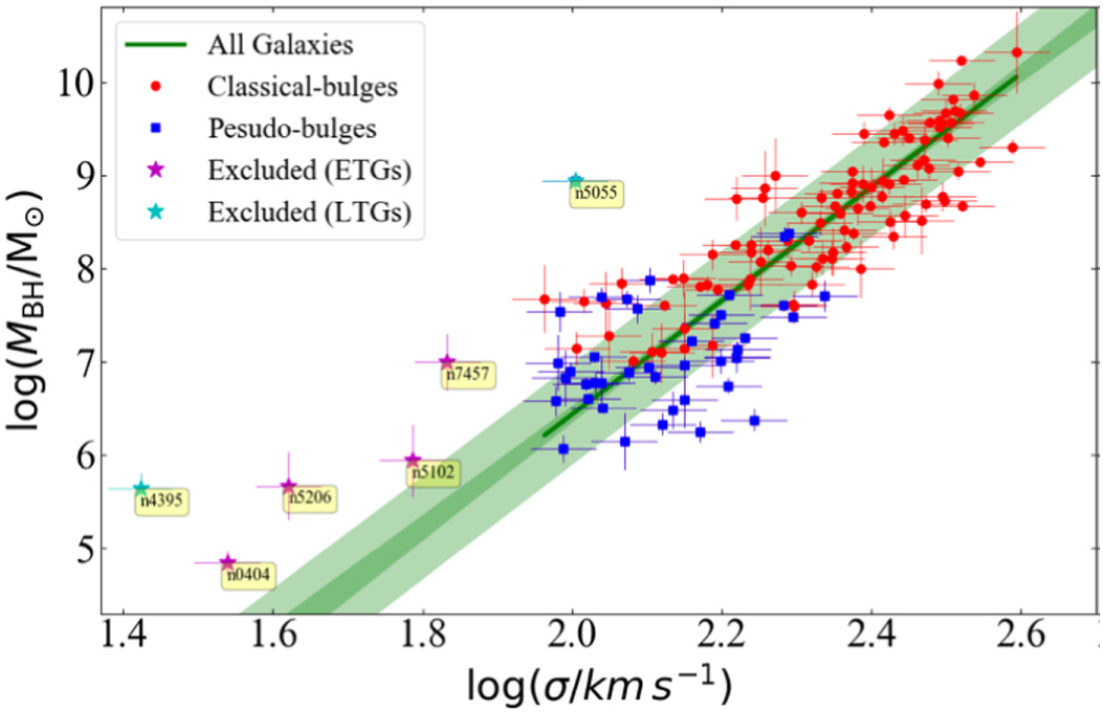

Figure 1.10: Black hole mass versus central velocity dispersion relation. The dark green line shows the best-fit relation, with the dark green shaded region indicating the $\pm 1\sigma$ uncertainty in the slope and intercept. The light green shaded region represents the $\pm 1\sigma$ scatter in the data. Red circles and blue squares denote galaxies hosting classical and pseudo-bulges, respectively. Figure taken from Sahu et al. (2019b).

a galaxy to the edge through radiation pressure. The derivation of this scenario leads to the relation given by:

$$M_{BH} = \frac{f\sigma^4\sigma_T}{\pi G^2 m_p}, \tag{1.15}$$

where f is the gas fraction of the galaxy, σ_T is the Thomson cross-section, and m_p is the mass of a proton. Therefore, we expect in this scenario that $M_{BH} \propto \sigma^4$. However, the energy-driven feedback is based on the energy required to prevent the collapse of gas content within the galaxy (Silk & Rees, 1998). This is achieved by equating the approximate energy of the collapsing gas with the Eddington luminosity. The required BH mass is thus approximated as:

$$M_{BH} \approx \frac{f\sigma^5\sigma_T}{4\pi G^2 m_p c}. \tag{1.16}$$

Therefore, we expect in this scenario that $M_{BH} \propto \sigma^5$. Numerous attempts have been made to measure the power-law of the $M_{BH} - \sigma$ relation, with a significant disparity in the measured slope, typically ranging from 3-8. The early observations reported mixed results, with Ferrarese & Merritt (2000) reporting a relation of $M_{BH} \propto \sigma^{4.80\pm0.50}$, supporting the energy model, while Gebhardt et al. (2000) reported $M_{BH} \propto \sigma^{3.75\pm0.30}$, supporting the momentum model. The difference between these relations and others was eventually revealed to be due to different treatment of errors and the choice of symmetrical or non-symmetrical regressions (Ferrarese et al., 2001; Kelly, 2007).

Another point of contention is whether different galaxy types follow the same relation. It has been frequently reported that the normalisation in the relation for barred and unbarred galaxies is different, and they should be analysed separately, as joint analysis will result in a steeper relation (Graham & Driver, 2007; Graham et al., 2011; Graham & Scott, 2013). This is supported by simulations from Hartmann et al. (2014) that suggested the kinematics of a bar can increase velocity dispersion by 20%, shifting galaxies right on the relation. However, more recent studies have found they follow the same relation, and the previous offset may be due to low sample size and the misclassification of bars, particularly weak bars (Savorgnan & Graham, 2016; Sahu et al., 2019b).

Bars are often linked to pseudo-bulges (Kormendy & Kennicutt, 2004), so the potential discrepancy associated with bars may be due to bulge type. This was suggested by Ho & Kim (2014), who found a lower normalisation for pseudo-bulges and suggested that different relations should be used when scaling SMBH mass. However, work by Sahu et al. (2019b) using a larger sample found that pseudo and classical bulges follow the same relation, noting that bulge classification method may have an effect on the recovered relations. There is also evidence that core-Sérsic galaxies, which are the most massive galaxies that undergo multiple dry mergers, follow a steeper relation (McConnell & Ma, 2013; Volonteri & Ciotti, 2013; Davis et al., 2019; Graham, 2023). However, this may be due to the limited σ range of core-Sérsic galaxies.

Another uncertainty in the $M_{BH} - \sigma$ relation is a potential selection bias in the dynamically measured SMBH sample. The bias may arise from the selection requirements for dynamic modelling, such as the SMBH sphere of influence being near the resolution limit of the telescope. Moreover, different dynamical tracers and modelling methods can produce irreconcilable mass measurements (Dominiak et al., 2024). This bias has been highlighted by a number of studies (Bernardi et al., 2007; Batcheldor, 2010; Gültekin et al., 2011; Morabito & Dai, 2012), more recently Shankar et al. (2016), found that the galaxy stellar mass-velocity dispersion of galaxies with dynamically detected SMBHs is significantly offset to higher velocities when compared to a large unbiased sample of active galaxies selected from SDSS. Therefore, the scaling relation derived from dynamically detected BHs may be sampling a biased population. Moreover, if the normalisation in the $M_{BH} - \sigma$ relation is wrong, the scaled mass derived from RM and SERM is also significantly biased. However, some have argued that the reported offset may be due to not distinguishing core-Sérsic and Sérsic galaxies, and to the misclassification of LTG as ETG in the selection of inactive SDSS galaxies, as they follow a lower normalisation on the $M_{gal} - \sigma$ relation (Sahu et al., 2019b). There is also debate as to whether the bias could be explained by discrepancies in the stellar mass scales between SDSS galaxies and the SMBH galaxy samples (Sahu et al., 2023; Shankar et al., 2025).

1.4.1.2 Black Hole-Stellar Mass Relations

The most cited mass relation is the $M_{BH} - M_{bulge}$ relation (also referred to as $M_{BH} - M_{sph}$), where M_{bulge} refers to the stellar mass of the galaxy bulge. An example of this relation is shown in Figure 1.11 taken from Kormendy & Ho (2013) and shows M_{BH} plotted against M_{bulge}. The nature of this relation, its evolution, and how it applies to different galaxy types have long been controversial. Early results, with extremely limited sample sizes dominated by massive elliptical galaxies, suggested a tight linear relation (Dressler & Richstone, 1988; Kormendy & Richstone, 1995). These samples were significantly expanded with HST, which allowed for tight constraints on BH mass and spatial decomposition of components. However, these larger studies revealed a more complex picture; the inclusion of lower-mass galaxies led to significantly steeper relations (Laor, 1998; Wandel, 1999; Salucci et al., 2000; Laor, 2001). This resulted in a significant debate on the steepness and normalisation of the relation and whether different populations followed different (or no) relation(s) and should be treated separately.

The separation of galaxies into different classifications is a complex issue, with different authors using a variety of methods to draw different conclusions with essentially the same data. Moreover, sample sizes are not large enough to cover the vast array of different galactic types, which include early/late type, core-Sérsic/Sérsic galaxies, presence of a bar, bar strength, classical/pseudo bulges, concentration, colour, bulge-to-total (B/T) ratio, and mass. Significantly larger sample sizes are needed to control for each of these properties with a statistically significant population.

One example is the division between core-Sérsic galaxies and Sérsic galaxies, as first reported by Graham (2012), who found a break in the $M_{BH} - L_{bulge}$ (bulge luminosity) and $M_{BH} - M_{bulge}$ relations. They reported that the Sérsic galaxies followed a much steeper relation than the more massive core-Sérsic galaxies. This could provide important insights into the mechanism of AGN fueling, as Sérsic galaxies are driven by gas-rich mergers and secular evolution, and a steeper relation indicates a higher fractional growth of the SMBH. In contrast,

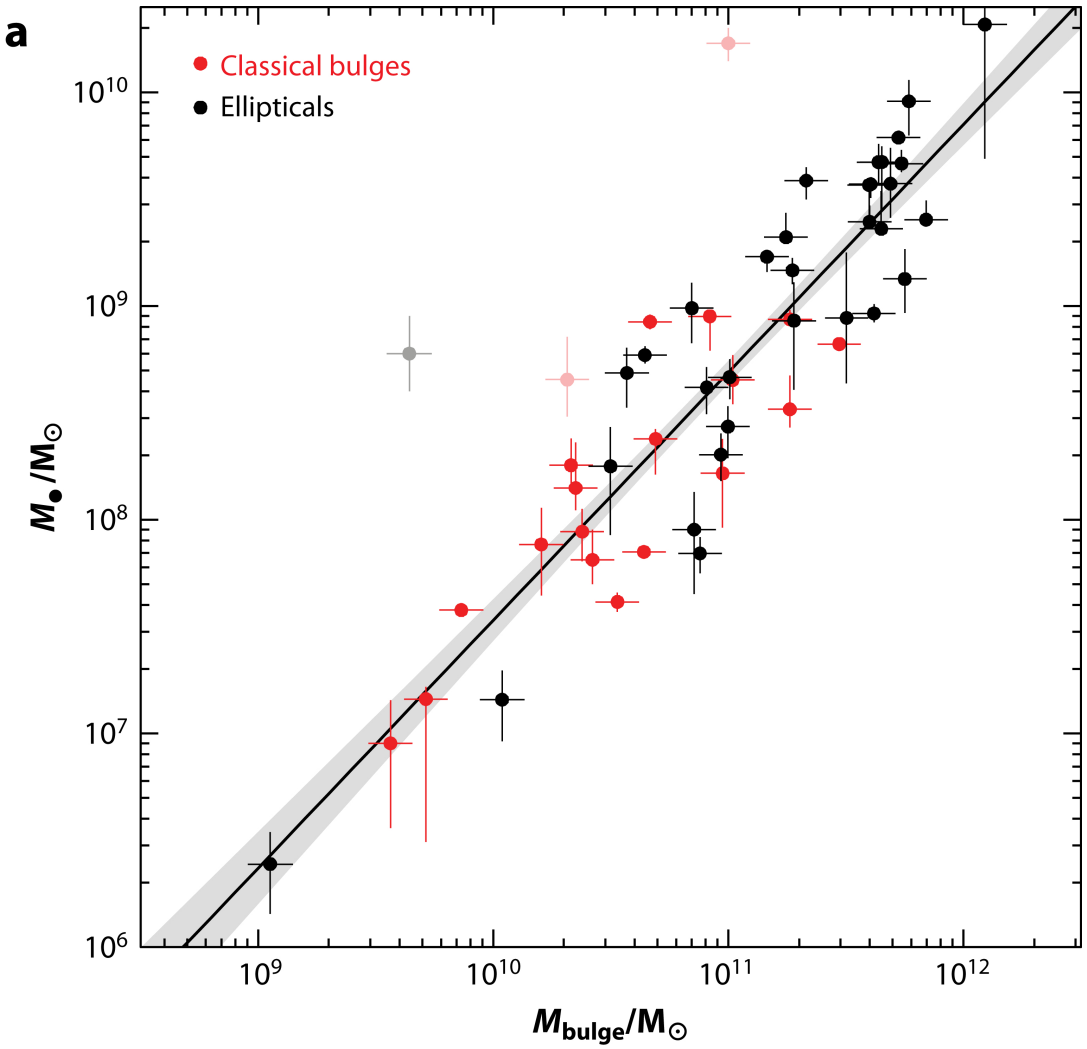

Figure 1.11: Black hole mass versus bulge stellar mass. The black line shows the best-fit relation, with the shaded region indicating the $\pm 1\sigma$ uncertainty in the slope and intercept. The red circles denote classical bulges and the black circles denote elliptical galaxies. Figure taken from Kormendy & Ho (2013).

the shallower, nearly linear relation suggests hierarchical growth with dry mergers. However, when controlling for just early-type galaxies, there is no statistical difference between the core-Sérsic and Sérsic galaxy relations (Saglia et al., 2016; Sahu et al., 2019a). This supports earlier claims that late-type galaxies (LTGs) follow a steeper relation than ETGs (Salucci et al., 2000).

Some have also argued that pseudo-bulges and classical bulges follow different relations. This was most notably highlighted in the review by Kormendy & Ho (2013), who claimed that SMBHs co-evolve with elliptical galaxies and classical bulges but not with pseudo-bulges, irrespective of mass. They also reaffirmed an unbroken linear relation and suggested that mixing morphological types gives steeper relations. Therefore, the driver of co-evolution has to be linked to a process that drives both morphological changes and mass growth, thus supporting the notion that co-evolution is driven by galaxy mergers.

Mergers, specifically major mergers, are closely linked with morphological transformation, as mentioned in Section 1.3. The kinematics of mergers result in angular momentum loss, which triggers the large-scale inflow of cold gas. Simulations have found the inflow rates to be consistent with the fueling requirements of even the most luminous AGN as well as global starbursts (Di Matteo et al., 2005; Hopkins et al., 2006; Peng, 2007). Observationally, this is supported by studies finding that the fastest-growing SMBHs are typically found in ongoing mergers (Volonteri et al., 2006; Urrutia et al., 2008; Glikman et al., 2015; Trakhtenbrot et al., 2017).

Another aspect of mergers is the subsequent merger of the SMBHs. This gives mergers an averaging effect as both the galaxy and SMBH merge. Simulations have shown that this averaging effect would tighten an existing relation (Peng, 2007; Hirschmann et al., 2010; Jahnke & Macciò, 2011). The increased merger rate of the highest-mass elliptical galaxies should thus produce the tightest relation. However, the merger of gas-poor discs with under-massive black holes may create an elliptical galaxy with a significantly under-massive SMBH (e.g., Graham & Sahu, 2023; Graham, 2023). This hierarchical assembly governed by the central limit theorem provides a formation mechanism independent of AGN feedback, although it is unclear to what degree mergers drive the co-evolution relation or if it is tightening an existing relation.

When compared with a mass-controlled sample drawn from the field, most surveys find a statistically insignificant or no elevation in AGN activity or median accretion rate in ongoing mergers or for galaxies with features indicative of recent merger activity (post-mergers) (Grogin et al., 2005; Hasinger et al., 2005; Allevato et al., 2011; Schawinski et al., 2011; Kocevski et al., 2012; Cisternas & Jahnke, 2015; Marian et al., 2019; Silva et al., 2021). Moreover, recent large-scale cosmological simulations have shown that merger-related processes contribute only a fraction of the SMBH mass growth (McAlpine et al., 2020; Smethurst et al., 2024). In the Horizon-AGN cosmological simulation (Martin et al., 2018), only $15-35\%$ of SMBH mass growth is attributed to mergers since $z=3$. Thus, most SMBH growth is driven by secular processes. Similarly, it is estimated that 77% of the total stellar mass growth occurs through secular evolution. This indicates that co-evolution may be dominated by secular evolution.

An important test of the role of secular processes and the merger-driven scenario is to examine galaxies where secular processes can be the only mechanism driving SMBH and galaxy growth, such as in the case of AGN hosted in extremely disc-dominated galaxies (Martig et al., 2012). Smethurst et al. (2019) detected outflows in 10 of a sample of 12 extremely disc-dominated AGN host galaxies, with a mean outflow rate of $1 M_{\odot} \mathrm{yr}^{-1}$, consistent with that of the broader AGN population. Subsequent work by Smethurst et al. (2021) found that the outflow velocities in these AGN-hosting galaxies are approximately 30 times greater than the escape velocity of the galaxy at the maximum detected radial extent of the outflows; similar results were found by (Bohn et al., 2022). This suggests that the outflows are sufficient to cause a feedback effect on the galaxy, such as expelling gas and heating the halo. The velocities, and consequently the kinetic energy injection rates and momentum, are on average higher than the typical AGN population while still within typical ranges. This was expected as the sample was selected for higher luminosity AGN. Moreover, a recent simulation study found that AGN feedback can reduce star formation by 30% in isolated disc galaxies (Sivasankaran et al., 2025).

The detected outflows in these galaxies thus necessitate a larger inflow to fuel AGN activity, central star formation and the central gas reservoir. Simulations of spiral arms and bars predict an inflow rate an order of magnitude higher than

the outflows detected in disc-dominated AGN host galaxies (Shlosman et al., 1989; Regan & Teuben, 2004; Davies et al., 2009; Lin et al., 2014; Fanali et al., 2015; Slater et al., 2019). However, the observational evidence linking spiral arm/bar structures and AGN activation is tenuous. Many studies have found no statistically significant link between these structures and AGN incidence (Martini et al., 2003; Lee et al., 2012; Cheung et al., 2015; Goulding et al., 2017). However, a recent study by Garland et al. (2023) using a colour-, volume-, and mass-matched sample found that barred galaxies have a higher AGN fraction. They also showed that there is a dependence on bar type, they found the AGN fraction for strongly barred, weakly barred, and unbarred galaxies to be $\approx 30\%$, $\approx 23\%$, and $\approx 14\%$, respectively. Another study by (Marels et al., 2025) found that prominent bars correlate with higher nuclear activity. These two studies are in good agreement with some recent simulations (Kataria & Vivek, 2024). However, significantly larger samples are required to control for the large parameter space and isolate the specific dependencies.

These active, highly disc-dominated galaxies are significantly at odds with the $M_{BH} - M_{bulge}$ paradigm as the BH masses, derived from broad lines, are significantly overmassive compared to their insignificant bulges. The decomposition of 101 of these galaxies by Simmons et al. (2017) and Fahey et al. (2025) found that the total stellar mass of these galaxies was consistent with the $M_{BH} - M_{bulge}$ scaling relation of massive ellipticals by Häring & Rix (2004). In contrast, the bulge components were inconsistent with the bulge relation. They found that the galaxies with reliable bulge measurements were typically offset by 1 dex in the bulge relation. Moreover, a significant portion had no detectable bulge and, thus, may be even larger outliers. The detection of strong outflows when investigating a subset of this sample by Smethurst et al. (2021) suggests that feedback may be impacting these galaxies, potentially driving co-evolution of the SMBH total stellar mass of the galaxy and not just the bulge. Observational evidence suggests that the galaxy disc progenitors form by $z > 3$ (e.g., Lelli et al. 2021; Roman-Oliveira et al. 2023; Ferreira et al. 2023; Jacobs et al. 2023; Robertson et al. 2023, this predates the peak of cosmic SMBH growth, potentially carrying information about co-evolution. Recent findings from Winkel et al. (2025) show

that the galaxy-wide stellar velocity dispersion of LTGs correlates with M_{BH}, which suggests that SMBHs do co-evolve with galaxy discs.

The earliest studies focused on massive ellipticals where $M_{bulge} \approx M_*$, where M_* is the total stellar mass, so comparing the $M_{BH} - M_{bulge}$ and the $M_{BH} - M_*$ relations was not meaningful. Beyond the extremely disc-dominated already mentioned, there is some evidence of a $M_{BH} - M_*$ relation across the broader population. Studies by Läsker et al. (2014) and Savorgnan & Graham (2016) found that M_{BH} correlates equally well with L_{Total} (total luminosity) as it does with L_{bulge}. A study by Sahu et al. (2019a) looking at 76 ETGs and 40 LTGs with dynamically detected SMBH found that the correlation in the bulge and the total stellar mass relations were comparable, with the total relation producing a steeper slope. Crucially, they found that the ETGs with disc components are systematically offset from the bulge relation by 1.3 dex, while they follow the same relation for total stellar mass. Therefore, the total stellar mass relation is significantly more reliable than the bulge relation for ETGs when highly accurate bulge decomposition is not available. However, they found that LTGs are in better agreement with the bulge relation of ETGs than the total relation. A similar result was also found by Greene et al. (2020), who found that inactive SMBHs in LTGs fall 1.2 dex below ETGs.

However, recent work by Zhuang & Ho (2023) found that early and late-type galaxies follow very similar $M_{BH} - M_*$ relationships for a sample of $\approx$ 11500) active galaxies at $z < 0.35$. For galaxies with a total stellar mass of $M_* = 10^{11} M_\odot$, the difference between the relations is only 0.28 dex, which is significantly smaller than the 0.4 dex associated with single-epoch virial mass estimation. Moreover, the active galaxies as a population have a significantly lower normalisation in the relation. A similar result was found by Reines & Volonteri (2015), who found that SMBHs very local ($z < 0.05$) active galaxies were around 1.2 dex less massive than the dynamically detected sample, with Sturm & Reines (2024) finding that the discrepancy also persists in the bulge relation. Studies have also found that classical and pseudo-bulges of active galaxies follow the same relation (Bennert et al., 2021; Winkel et al., 2025), while (Saglia et al., 2016) suggest that dense pseudo-bulges follow the same relation as classical bulges.

Cosmological simulations have also produced evidence to support a $M_{BH} - M_*$ relation. Martin et al. (2018) and Smethurst et al. (2024) found that the $M_{BH} - M_*$ relation in the Horizon-AGN simulation was tighter than the $M_{BH} - M_{bulge}$ relation. They also found a strong dependence on the B/T ratio for the normalisation galaxies on the $M_{BH} - M_{bulge}$ diagram, with low B/T galaxies having significantly higher normalisations. In contrast, the $M_{BH} - M_*$ diagram showed no dependence on the B/T ratio. The dependence on B/T persists regardless of the merger history. However, it is most pronounced in galaxies with no mergers since $z = 2$. They find that mergers can reduce the scatter in the relation, but co-evolution is independent of mergers and bulge growth. Moreover, simulations have also suggested the majority of bulge growth is a result of disc instabilities, rather than mergers, including in bulge-dominated galaxies and bulges with high Sérsic index, which are likely classical (Parry et al., 2009; Martig et al., 2012; Gargiulo et al., 2017; Du et al., 2021). An observational study by Bell et al. (2017) found the stellar halos of some massive classical bulges are inconsistent with a merger origin, further highlighting the role of secular processes.

1.5 This Thesis

In this introduction, we have laid the foundations of AGN–galaxy co-evolution and highlighted some of the contradictory findings in the field. The main focus of the following chapters is on the morphological dependence of SMBH–galaxy co-evolution. A swath of unresolved questions persists, motivating continued research. In this thesis, we contribute to addressing the following questions.

- Why do different samples of low redshift Type 1 AGN hosted in disc-dominated galaxies produce disparate $M_{BH} - M_*$ scaling relations?
- Where do low redshift Type 1 AGN lie on the $M_{BH} - M_*$ and $M_{BH} - M_{bulge}$ diagrams?
- How does the location of Type 1 AGN on the $M_{BH} - M_*$ and $M_{BH} - M_{bulge}$ diagrams depend on the B/T ratio?

- Where do Type 1 AGN host galaxies with different morphologies lie on the $M_* - R_{eff}$ relation?

In Chapter 2, we build an empirical model of SMBH growth based on observational distributions. In Chapter 3, we investigate the selection of three samples of Type 1 AGN in disc-dominated galaxies, which produced seemingly disparate results. In Chapter 4, we use multi-component 2D decomposition of HSC images to measure the structural components of a large sample of Type 1 AGN host galaxies and assess the morphological dependence, as indicated by the B/T ratio, of the $M_{BH} - M_*$, $M_{BH} - M_{bulge}$ and $M_* - R_{eff}$ relations. In Chapter 5, we summarise our findings and discuss their implications in the context of AGN–galaxy co-evolution, highlighting potential directions for future research.

Chapter 2

Creating a Large Sample of Mock Type-1 AGN

The observed relations between supermassive black holes (SMBHs) and their host galaxies such as the black hole (BH) mass–galaxy scaling relations have become key diagnostics in understanding galaxy evolution (Kormendy & Ho, 2013; Greene et al., 2020). Moreover, the study of AGN luminosity space density is a key statistical tool that can constrain the abundance and growth history of SMBHs. It has revealed a connection between star formation and SMBH accretion histories, hinting at a shared evolutionary pathway (Soltan, 1982; Boyle & Terlevich, 1998; Delvecchio et al., 2014; Aird et al., 2015).

However, there is still no consensus on the exact form of these relations, how they evolve over time, or how they depend on galaxy parameters such as morphology and the physical processes that connect them. For example, studies investigating the relation between total stellar mass (M_*) and BH mass (M_{BH}), using different methods and selection criteria, have found varying results. Reines & Volonteri (2015) and Sturm & Reines (2024) found that the local relation traced by accreting SMBHs has a normalisation over an order of magnitude lower in black hole mass for a given total stellar mass than the canonical scaling relation traced by inactive galaxies. However, other studies of low-redshift AGN have found less extreme differences or comparable normalisations (Simmons et al., 2017; Bennert

et al., 2021; Zhuang & Ho, 2023; Fahey et al., 2025). Each of these studies utilises Type 1 AGN so that their black hole mass estimates are reasonably well constrained, and they sample from the same extragalactic surveys. Yet their different results are seemingly contradictory.

Each selection method may suffer from unique selection effects and systematic biases, which could influence their results in different ways (Jones et al., 2017). Moreover, the relations derived from dynamical modelling of inactive galaxies may also be sampling a biased population. Constraints, such as requiring a highly resolved SMBH sphere of influence, may introduce poorly understood selection effects that bias the sample (Shankar et al., 2016, 2019). For AGN samples, different selection choices may result in sampling distinct subsets of the broader AGN population. For example, high-redshift studies are clearly biased towards the most massive and highly accreting SMBHs due to flux limitations (Suh et al., 2020; Mountrichas, 2023). On the other hand, low-redshift studies may not be able to sample large enough volumes to capture the rarest (i.e., most luminous and/or massive) accreting SMBHs. Accounting for selection effects presents a significant challenge, as the specific biases involved are often unclear or multifaceted. One way to investigate their impact is to simulate the underlying population and apply different selection criteria. This requires accurate evolutionary histories of SMBHs.

AGN produce highly luminous emission across the electromagnetic spectrum, which is directly linked to the accretion rate. However, extracting such histories from observational data is challenging. AGN inclination angle (Antonucci, 1993; Kauffmann et al., 2003), large amounts of cold gas in the ISM, and stellar processes (Fornasini et al., 2018) can obscure or contaminate AGN emission. This makes constructing an accurate census of AGN activity across cosmic time difficult. However, X-ray emission is a near-ubiquitous signature of AGN and can penetrate high column densities up to $N_e \sim 1.5 \times 10^{24}$ cm^{-2} (Della Ceca et al., 2008; Kocevski et al., 2015). Therefore, X-ray observations provide a robust tracer of SMBH accretion across cosmic time.

As the active phases of SMBHs are episodic and highly variable on short timescales, relative to galactic processes (Hickox et al., 2014; Yang et al., 2016), early studies found weak dependence on host galaxy properties, such as star

formation rate (Aird et al., 2012; Harrison et al., 2012). However, once variability on galactic timescales is accounted for, the mean BH accretion rate is found to be redshift-dependent and correlated with both stellar mass and star formation rate (SFR) (Hickox et al., 2014; Yang et al., 2017, 2018; Zou et al., 2024).

In this chapter, we consider the results of multiple past studies and combine them to build an empirical model of SMBH growth. We evolve a mock population of SMBHs based on a heavy seed model from $z = 4.25$ to $z = 0$. Our goal is to construct a realistic sample of the underlying Type 1 AGN population. This will also allow us to investigate the impact of selection effects on the properties of a recovered sample of AGN. Throughout the chapter, we adopt a flat cosmology with $\Omega_\Lambda = 0.7$ and $H_0 = 70$ km s^{-1} Mpc^{-1}.

2.1 Mock population synthesis

In this section, we present an empirically driven methodology to evolve a population of SMBHs from relatively early times to the present day. The subsections below describe the initial population of a SMBH mass function, the growth rates and duty cycles used, and the details of how we evolved this mock population in time steps (ΔT) from $z = 4.25$ to $z = 0$.

2.1.1 SMBH masses at z = 4.25

To assign the initial BH mass in our mock population we draw from a theoretical mass function at $z = 4.25$ from Natarajan & Volonteri (2012). Their mass function is based on a heavy seed model of SMBH formation, where massive seeds form from the direct collapse of pre-galactic discs (Lodato & Lopes, 2006; Lodato et al., 2007). In this scenario $M_{BH} \approx 10^5$–10^6 M$_\odot$ SMBHs can form at high redshift ($z > 15$). Recent observations from the *James Webb Space Telescope* of high redshift ($z > 6$) SMBHs with $M_{BH} = 10^{10}$ M$_\odot$ favour a heavy seed model for their formation (Pacucci et al., 2023; Yue et al., 2024). We use a theoretical mass function to avoid potential selection bias in the locally observed BH mass function. Additionally, as the lower limit for the mass function from Natarajan &

Volonteri (2012) is $10^7 M_\odot$ we extend it to $10^{4.5} M_\odot$ to fully cover our mass range, assuming it remains constant. We choose a flat extrapolation in order to minimise its potential effects versus extrapolating a declining or increasing mass function. However, we note that reasonable variations of this choice do not significantly affect our later results.

2.1.2 SMBH growth histories

In order to evolve the mock SMBH population to $z = 0$, we need to assign a realistic BH growth rate and duty cycle, where the duty cycle is the fraction of the time a SMBH is an AGN. However, we cannot assign a single duty cycle and growth rate, as studies have shown that they both evolve with redshift and change as a function of mass, star formation rate and compaction (Aird et al., 2018, 2019, 2022).

We base our growth rates on Aird et al. (2018, hereafter A18), who used deep *Chandra* (Weisskopf et al., 2002) X-ray imaging to measure the probability distribution of specific black hole accretion rates ($\lambda_{\rm sBHAR}$) for galaxies selected from four of the CANDELS fields and the UltraVISTA survey (Skelton et al., 2014). They adopted a Bayesian framework to account for the sensitivity limits of *Chandra* and to constrain the probability distributions of the SMBH accretion rates, correcting for incompleteness in X-ray detections. Moreover, as the motivation for this mock population is based on unobscured AGN, any bias against obscured AGN in the A18 distributions is not a major concern.

To derive a SMBH accretion rate, they assumed a fixed scaling between $M_{\rm BH}$ and $M_\star$ of 0.002. This gives an approximation for M_{BH} that can be used to approximate the Eddington luminosity (L_{Edd}). Then applying bolometric correction to the X-ray luminosity, they can measure a $\lambda_{\rm sBHAR}$. This can be written as

$$\lambda_{\rm sBHAR} = \frac{k_{\rm bol} L_X}{1.3 \times 10^{38}\,{\rm erg\,s^{-1}} \times 0.002\,\frac{M_*}{M_\odot}} \tag{2.1}$$

where L_X is the $2-10$ keV X-ray luminosity and $k_{\rm bol}$ is the bolometric correction factor, assumed to be constant at a value of 25 (Aird et al., 2018). As the

Eddington ratio is defined as ($\lambda_{\rm Edd} = L_{\rm bol}/L_{\rm Edd}$), then $\lambda_{\rm sBHAR} \approx L_{\rm bol}/L_{\rm Edd}$. Although this is inaccurate on an individual level, it is appropriate for a large population study. A more direct measure of $\lambda_{\rm Edd}$ requires a measurement of M_{BH}, which is limited by obscuration and by the feasibility of observing a large sample of emission lines across a broad redshift range.

Using this, they then determined the evolution of $\lambda_{\rm sBHAR}$ as a function of stellar mass. Their stellar mass range was $10^{8.5} < M_* < 10^{11.5} M_\odot$ with a redshift range of $0 < z < 4$.

We convert the assigned $\lambda_{\rm sBHAR}$ into an accretion rate using the equation

$$\dot{M}_{\rm BH} = \frac{\lambda_{\rm sBHAR} L_{\rm Edd}}{\eta c^2} \tag{2.2}$$

where η is the radiative efficiency and is set to a value of $\eta = 0.1$ (Thorne, 1974) and we assume $\lambda_{\rm sBHAR} = \lambda_{\rm Edd}$. This accretion rate is then used to calculate the M_{BH} for the next time step (ΔT).

$$M_{\rm BH}^{\rm New} = M_{\rm BH}^{\rm Old} + \dot{M}_{\rm BH}^{\rm New}\, \Delta t \tag{2.3}$$

where $M_{\rm BH}^{\rm New}$ is the SMBH mass at the end of the current snapshot and $M_{\rm BH}^{\rm Old}$ is the SMBH mass at the beginning of the snapshot.

As AGN growth is periodic, only a small subsample of SMBHs will become active at any given instant. We select the active SMBHs using the duty-cycle distributions from A18, who characterise the duty cycle as a function of stellar mass and redshift. In A18, the duty cycle is defined as the fraction of SMBHs growing at $\lambda_{\rm sBHAR} > 0.01$. They calculate the AGN duty cycle for each stellar mass and redshift bin using their measurements of $p(\log \lambda_{\rm sBHAR} | M_*, z)$, by integrating the probability distribution according to the following equation:

$$f(\lambda_{\rm sBHAR} > 0.01) = \int_{-2}^{\infty} p(\log \lambda_{\rm sBHAR} | M_*, z)\, d \log \lambda_{\rm sBHAR}\ . \tag{2.4}$$

2.1.3 Evolving the mass function

The first step is to assign the initial SMBH mass. The stellar mass bins from A18 are $10 < \log(M_*/M_\odot) < 10.5$, $10.5 < \log(M_*/M_\odot) < 11$, $11 < \log(M_*/M_\odot) < 11.5$. A18 also gives distributions for lower-mass bins. However, they do not span the full redshift range. Moreover, the samples motivating this mock construction are covered by the three mass bins that have already been stated, so we omit the other mass bins. For each stellar mass bin, we randomly sample the SMBH mass function from Natarajan & Volonteri (2012) to populate the bins. We emphasise that we do not assume a $M_{BH} - M_*$ relation in assigning BH mass, as we are just evolving a BH population, not simulating galaxy growth. We need realistic overall count of galaxies at different stellar masses and to account for differences across bins. However, we limit the maximum BH mass in the $10 < \log(M_*/M_\odot) < 10.5$ mass bin. Moreover, we assign slightly different numbers of BHs to each galaxy mass bin to reflect the different number densities of these galaxies at $z = 0$ taken from Song et al. (2016). We note that SMBHs do not change galaxy mass bins. While this is not true in reality, the purpose of evolving this mass function is *not* to co-evolve the BHs with host galaxies. The purpose of these mocks is to apply reasonable growth rates and duty cycles to the BHs based on the A18 measurements.

The distributions in A18 are split into the following redshift bins: $z = 0.1 - 0.5, 0.5 - 1.0, 1.0 - 1.5, 1.5 - 2.0, 2 - 2.5, 2.5 - 3$ and $3.5 - 4$. As we evolve to $z = 0$ and begin at $z = 4.25$, we extend the first and last redshift bins to cover them and assume that the distributions are unchanged. We evolve the population with time steps of length $\Delta t = 1$Myr. For each timestep and mass bin, we select a subsample to become active, according to the appropriate duty cycle. We opt to use duty cycles as opposed to sampling from the whole specific accretion rate distribution, as low accretion rates contribute negligibly to the total mass growth, and excluding them greatly improves computational efficiency. The selection of SMBHs in a given timestep is independent of other time steps. We also do not enforce a minimum or maximum duration of activity once a black hole switches from inactive to active, as individual accretion episodes may be similar to or less than our chosen ΔT (Schawinski et al., 2015). In any case, this does not

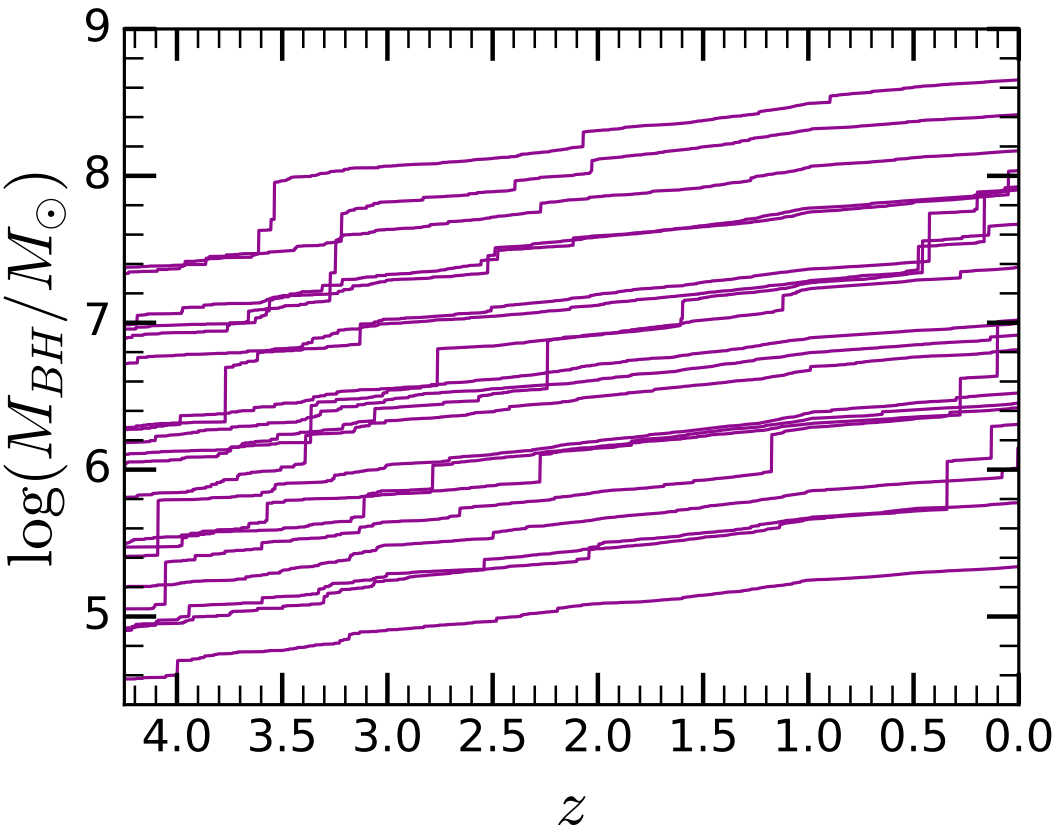

Figure 2.1: A selection of SMBH growth histories as a function of redshift. Black holes generally grow relatively slowly from $z = 4.5$ to $z = 0$, with a range of individual growth episodes. The model behaves realistically with long periods of slow growth and rapid high accretion phases.

affect cumulative statistics for an observation of a mock population (Hopkins & Hernquist, 2009c). For the SMBHs selected to grow, we assign a $\lambda_{\rm sBHAR}$ by drawing from the probability distributions from Figure 5 in A18. In Figure 2.1 we show the BH mass growth history for a selection of SMBHs. Most growth is slow, with limited episodes resulting in growth of at most ~ 0.5 dex in black hole mass.

2.2 Observing the mock population

To create a catalogue of Type 1 AGN, we first assume that each SMBH will be "observed" once, and thus randomly choose a mock-observation redshift from $0.001 \leq z \leq 0.25$ for each AGN. We note that we use the $z = 0$ mass of the SMBHs, which does not have a significant effect averaged over the population. We set the redshift distribution in such a way as to preserve a constant number density with redshift. For every SMBH, we assign an accretion rate based on the appropriate probability distribution of λ_{sBHAR}. We use this to derive an X-ray and bolometric luminosity, which can be used in the derivation of the flux.

2.2.1 Type 1 AGN

AGN are often split into two sub-classes, namely Type 1 and Type-2 AGN. Type 1 are characterised by the presence of broad optical emission lines, produced by Doppler broadening of emission lines in the broad line region of the AGN. Type-2 AGN lack these broad emission lines, due to obscuration by Compton-thick material. The main explanation for the origin of these two subclasses is the obscuration from the torus in the AGN unification model (Antonucci, 1993). However, obscuration can also indicate a weaker AGN, incapable of expelling the surrounding gas and dust in the galactic centre (Hopkins et al., 2006; Somerville et al., 2008; Circosta et al., 2019). Therefore, AGN luminosity and galaxy properties need to be taken into account when assigning an obscuration class, as samples of Type 1 and Type-2 AGN can have different properties. As X-ray wavelengths are less impacted by obscuration, they can be used to predict the likelihood of optical obscuration. For this we use results from Merloni et al. (2013), who studied 1310 AGN from the XMM-COSMOS point-like source catalogue (Hasinger et al., 2007; Cappelluti et al., 2009). They found a strong relation between optical obscuration and X-ray luminosity that is slightly host-mass dependent but approximately redshift independent between $0.3 < z < 3.5$. For each SMBH we assign their class based on the obscuration probability at their X-ray luminosity and mass bin.

In the left panel of Figure 2.2 we show the SMBH mass density function (BHDF) of our mock at $z = 4.25$ and of the mock Type 1 AGN at $z = 0$, and in

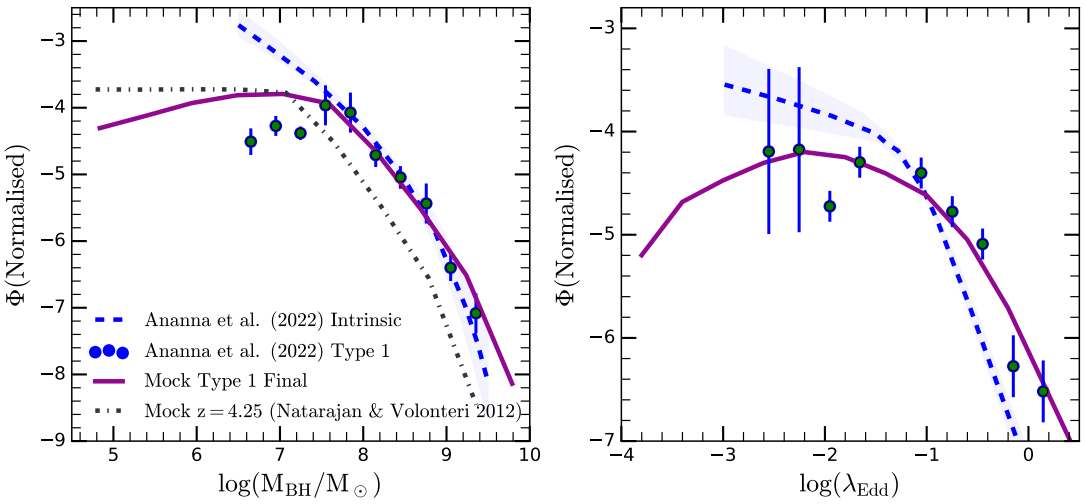

Figure 2.2: BH mass (left) and Eddington ratio (right) density functions of the Type 1 AGN mock population, scaled to match Ananna et al. (2022). The black dash-dot line represents the mass function of SMBH at $z = 4.25$ and the purple line represents the mass function of the Type 1 AGN sampled between $0.001 \leq z \leq 0.25$ in the mock. The blue data points are observed values at $z \leq 0.3$ from Ananna et al. (2022), plotted with 1σ error bars; the dashed blue line is their predicted intrinsic population with a 1σ error region. The mock population grows in a realistic way between the starting and ending redshift of the simulation and the final populations are similar to observed distributions.

the right panel we show the Eddington ratio density function (ERDF) of Type 1 AGN. As a comparison, we also include density functions of SMBH mass and Eddington ratio of Type 1 AGN from Ananna et al. (2022). Their sample utilises optical spectroscopic measurements and X-ray spectral analysis of 366 Type 1 AGN from the Swift/BAT AGN Spectroscopic Survey DR2 (Koss et al., 2017, 2022). Their optical spectroscopic analysis allows for BH mass measurements using broad emission lines, allowing for a more direct measurement of $\lambda_{\rm Edd}$. They also account for observational biases to predict intrinsic density functions. We find a seemingly realistic evolution of the mass function from $z = 4.25$ to the mock observed AGN. The BHMF is in good agreement with the observed and intrinsic BHMFs from (Ananna et al., 2022) at $M_{BH} > 10^{7.5} M_{\odot}$.

The ERDF is also similar to the observed function. This suggests that our application of $\lambda_{\rm sBHAR}$ is broadly similar to $\lambda_{\rm Edd}$. However, the intrinsic function measured by Ananna et al. (2022) is significantly steeper; this is in part due to our sampling of lower SMBH masses, which required a higher $\lambda_{\rm Edd}$ to obtain a Type 1 classification due to the dependence on X-ray luminosity. Moreover, their obscuration level is not dependent on luminosity, which may contribute to the higher density of low $\lambda_{\rm Edd}$ and low mass AGN in their intrinsic function.

2.2.2 Conclusion

The motivation of this work is to generate a diverse and realistic population of Type 1 AGN without assuming co-evolution. We use high-quality observations of intrinsic populations and make reasonable assumptions and extrapolations where necessary. Using observations of SMBH accretion rate constraints, in the form of probability distributions of specific black hole accretion rates ($\lambda_{\rm sBHAR} \propto L_{\rm bol}/M_{\star}$) as a function of redshift and stellar mass from Aird et al. (2018), we evolve a population of SMBHs to $z = 0$. Using the relation between X-ray luminosity and obscuration, we constructed a sample of Type 1 AGN. In Chapter 3 we implement these mocks in the analysis of the selection effects and how they shape samples of Type 1 AGN.

Chapter 3

The Role of Selection Bias in shaping AGN Scaling Relations

3.1 Introduction

Active galactic nuclei (AGN) are often highlighted as a fundamental aspect of galaxy evolution. This is supported by the observation of scaling relations between supermassive black holes (SMBH) and the properties of their host galaxy (Kormendy & Ho, 2013). Two of the most notable relate the mass of the SMBH to that of the bulge and to the total stellar mass of the host galaxy (Häring & Rix, 2004; Kormendy & Ho, 2013). However, as these relations are empirical relationships, an important and commonly utilised tool in astrophysics, they are susceptible to selection effects in the collected data. These limitations are partly why the mechanism(s) driving these relations, how they evolve with redshift and how fundamental they are, are still actively debated (Peng et al., 2006; Alexander et al., 2008; Schulze & Wisotzki, 2014; Mountrichas, 2023).

It is important to ascertain in what context co-evolution is present, and with what galactic properties it is associated, as that may indicate which is the main mechanism driving the inflow of gas from kiloparsec scales, which facilitates accretion. Mergers, specifically mergers with mass ratios of at least 1:4 between the secondary and primary galaxy, have previously been suggested as potential

drivers of co-evolution (Marconi & Hunt, 2003; Häring & Rix, 2004). If this is the primary mechanism for SMBH growth, we would expect massive BHs to be only found in merger remnants. These are elliptical-type galaxies, or the bulges of disc-type galaxies which persist after a disc reforms following a gas-rich merger (Hopkins et al., 2009; Pontzen et al., 2016). However, work by Bell et al. (2017) suggests bulge growth is not solely driven by merger-related processes.

While bulges, i.e. elliptical galaxies or bulge-dominated disc-galaxies, do host SMBHs, and there is evidence that bulge mass ($M_{\rm bulge}$) correlates to black hole mass ($M_{\rm BH}$) in observations and simulations (e.g. Kormendy & Ho, 2013; Volonteri et al., 2016) we also see luminous (quasar-like) BH growth in disc-dominated galaxies. These galaxies have had quiet baryon accretion histories and are unlikely to have had a significant merger since $z \sim 2$ (Martig et al., 2012), though their BH luminosities are typically more moderate (e.g., Schawinski et al., 2011, 2012; Simmons et al., 2011, 2012; Kocevski et al., 2012). Moreover, $M_{\rm BH}$ has also been shown to correlate with the stellar mass, M_*, in some disc galaxies (e.g., Cisternas et al. 2011b; Simmons et al. 2013, Simmons, Smethurst & Lintott 2017). This indicates secular processes are also drivers of SMBH growth, with smooth accretion of cold gas to the central SMBH (Kormendy & Kennicutt, 2004; Sancisi et al., 2008), which in turn may drive feedback (e.g., Smethurst et al., 2019, 2021).

Recent observational and theoretical work has suggested that SMBH growth in the absence of mergers (i.e., due to secular processes) is the *dominant* means of growth (e.g., Mechtley et al., 2016; Martin et al., 2018; Marian et al., 2019; McAlpine et al., 2020). This could indicate that the growth of SMBHs in disc-dominated galaxies, which have had limited merger histories, is not atypical. Therefore, isolating galaxies with a merger-free history is a way of probing this dominant means of SMBH growth. However, most samples have focused on the co-evolution of BHs with galaxies of early-type morphologies (indicative of an evolutionary history involving significant mergers) and hosting luminous AGN (for a review, see Kormendy & Ho, 2013). This is in part due to the challenges of isolating galaxies whose growth has been free of significant mergers and whose SMBH masses can be reliably estimated, limiting the size of observational samples where the examination of merger-free co-evolution is possible. Studies that have

included investigation into co-evolution in disc-dominated galaxies have presented divergent results, such as Reines & Volonteri (2015) and Simmons, Smethurst & Lintott (2017), whose best-fit $M_{\rm BH}$-M_* relations, where $M_{\rm BH}$ is plotted against M_*, differ in their y-intercept by a factor of ~ 1 dex. In particular, the Simmons et al. relation is consistent with Häring & Rix (2004), while Reines & Volonteri is significantly below it. The latter would suggest that mechanisms that drive bulge growth are tied to SMBH growth, whereas the former implies that the growth of the SMBH is linked to the gravitational potential of the galaxy. In other words, one result indicates that they are sampling different populations, while the other indicates that they are sampling different parts of the same population.

In this work, we attempt to reconcile the results of three studies, which present the contradictory correlation between AGN and the total stellar mass of disc-dominated galaxies. Furthermore, we investigate whether they can be unified into a single relationship that is more representative of the underlying population. We then apply selection functions based on the redshift-flux distributions of each study to the mock Type 1 AGN population outlined in section 2 to create artificial samples, each drawn from the same underlying distribution. We then compare the samples derived from the mock population with the observed samples to determine whether the three observational samples are consistent with being drawn from the same underlying population. We subsequently examine the combined population represented by the concatenation of the 3 studies, as a means of probing merger-free SMBH growth and co-evolution at $z < 0.25$.

In Section 3.2 we describe the three observational samples, including their described selection functions and the black hole-galaxy relations that each observes. We also investigate the strength of secondary selection biases in each sample, which were not explicitly reported by each study. In Section 3.3, we describe the method used to sample the mock population of AGN. We present our results in Section 3.4. We discuss their implications and further analyse the three samples in Section 3.5.

Where necessary we adopt a cosmology consistent with Λ-CDM, with $H_0 = 70$ km s^{-1} Mpc^{-1}, $\Omega_m = 0.3$ and $\Omega_\Lambda = 0.7$

3.2 Data

This study aims to investigate the impact of selection effects on the observed differences in scaling relations from multiple studies of disc-dominated AGN host galaxies and determine whether they can be unified into a single scaling relation.

We selected three studies that include disc-dominated galaxies and whose results substantially differ. We require that the samples in these studies contain unobscured (Type 1) AGN, as the relations between their optical broad-line properties and mass produce very reliable estimates of black hole mass (e.g., Greene & Ho, 2005). The three works from which we draw samples are Reines & Volonteri (2015), Simmons, Smethurst & Lintott (2017), and Bennert et al. (2021). Below we briefly describe each study, highlighting their motivations, selection methods, and the resultant biases when analysed in a wider context. The general properties of these samples can be seen in Figure 3.1.

3.2.1 Reines & Volonteri (2015)

The aim of the Reines & Volonteri (2015, hereafter RV15) study was to create a baseline for $M_{\rm BH} - M_*$ relations for higher redshift galaxies by quantifying the differences between the local $M_{\rm BH} - M_{\rm bulge}$ and $M_{\rm BH} - M_*$ relations, using techniques utilised at higher redshifts. They also compared the relationship for different morphological classifications.

The driving motivation behind this is that direct methods of black hole (BH) mass measurements, such as dynamical measurements, are not available at higher redshift. Thus, indirect measurements are used, which have larger uncertainties. Moreover, limitations to spatial resolution and sensitivity mean that the decomposition of stellar and bulge masses generally becomes less reliable at higher redshifts. Studies therefore typically compare the total stellar mass for high-redshift galaxies to low-redshift galaxy bulge mass. RV15 examined how this comparison may impart bias.

RV15 drew their sample from the NASA-Sloan Atlas (NSA) (Aihara et al., 2011), which is derived from Sloan Digital Sky Survey (SDSS; York et al., 2000) Data Release 8 (DR8; Abazajian et al., 2009; Aihara et al., 2011) and contains

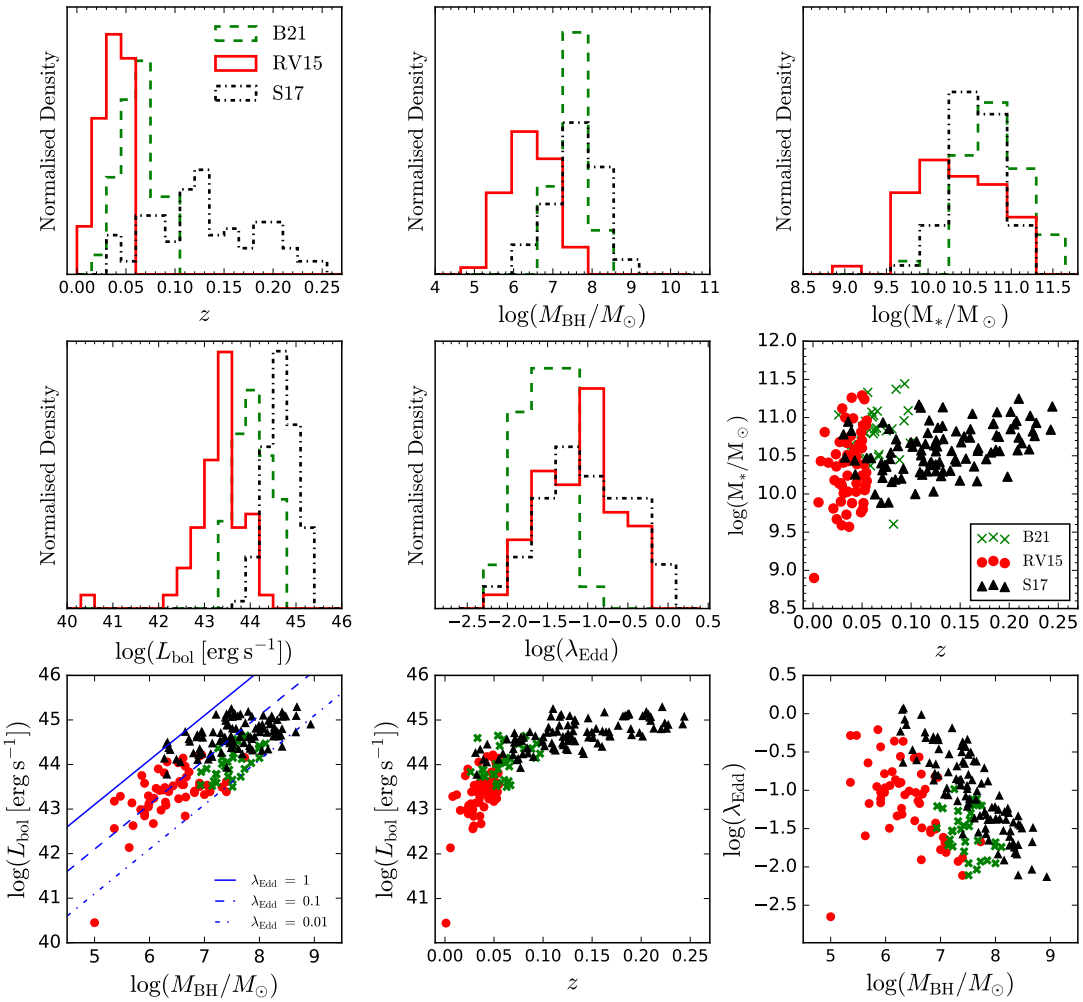

Figure 3.1: Sample Distributions: Normalised distributions for redshift (z), black hole mass ($M_{\rm BH}$), galaxy stellar mass (M_*), bolometric luminosity ($L_{\rm bol}$) and Eddington ratio ($\lambda_{\rm Edd}$). The red solid line represents the sample from Reines & Volonteri (2015) (RV15), the green dashed line represents the sample from Bennert et al. (2021) (B21) and the black dash-dot line represents the sample from Simmons et al. (2017) (S17). While the M_* distributions are similar, the other properties are divergent. **Sample Relations:** Relations for M_* vs z, $L_{\rm bol}$ vs $M_{\rm BH}$, $L_{\rm bol}$ vs z and $\lambda_{\rm Edd}$ vs $M_{\rm BH}$. For reference we show lines of constant Eddington ratios of $\lambda_{\rm Edd} = 1$ (solid), $\lambda_{\rm Edd} = 0.1$ (dashed) and $\lambda_{\rm Edd} = 0.01$ (dot-dashed). The samples appear to be sampling different parts of the same underlying and continuous population.

a reanalysis of SDSS optical photometry and spectroscopic data at redshifts $z \leq 0.055$. RV15 searched the NSA catalogue for objects with broad Hα emission as well as narrow emission-line ratios indicative of AGN. To reduce contamination, RV15 only selected BHs that occupy the AGN region of the [OIII]/Hβ vs [NII]/Hα BPT (Baldwin, Phillips & Terlevich, 1981; Kewley, Groves, Kauffmann & Heckman, 2006) diagram and the Seyfert region of the [OIII]/Hβ vs [SII]/Hα diagram.

RV15 determined BH masses using the well-established single-epoch spectroscopic BH scaling relations between BH mass and the FWHM and the luminosity of the Hα line. These relations are based on the assumption that the broad-line region (BLR) is kinematically dominated by the mass of the BH. RV15 followed the same approach as described in Greene & Ho (2005) and Richards et al. (2006a), but used the updated radius-luminosity relationship from Bentz et al. (2013). For bolometric luminosity, RV15 used the conversion between $L_{\mathrm{H}\alpha}$ and L_{5100}, which can subsequently be converted to L_{bol} using $L_{\mathrm{bol}} = 10.3L_{5100}$ (Greene & Ho, 2005; Richards et al., 2006a). For the total stellar mass of the galaxy, M_*, RV15 used mass-to-light ratios for i band data, M/L_i, as a function of $g-i$ colour (following Zibetti et al., 2009). During this process, they removed any system where the AGN luminosity dominates the integrated photometry. This removed a small number of AGN, adding bias against higher M_{BH}/M_* systems; this gave a sample of 244 Type 1 AGN. RV15 also included an additional 8 dwarf galaxies hosting Type 1 AGN from their previous work (Reines et al., 2013). These additional objects were missed in the RV15 analysis due to a higher threshold for detection. Additionally, 1 of these 8 objects has no broad line detection in the Reines et al. (2013) paper; however, a review by Baldassare et al. (2015) with higher resolution spectroscopy identified broad emission. RV15 also included a dwarf galaxy known as Pox 52 from Thornton et al. (2008). However, as the dwarfs were drawn from a different selection method and they occupy a different host mass range to the other samples, we exclude them from our analysis.

In order to assign morphologies to their sample, RV15 cross-matched their sample with a catalogue of automatically morphological classified galaxies from Huertas-Company et al. (2011). Only 121 of 244 galaxies in RV15 were in the Huertas-Company et al. (2011) catalogue; we refer to the galaxies that received

classification as HC11 and ones that did not as unclassified-HC11. The galaxies in HC11 were divided into four morphological classes: Sab (45), Scd (15), S0 (39) and E (22). We consider the late-type (Sab, Scd) subsample of RV15, consisting of 60 galaxies, for comparison in this study. We also performed our own independent visual classifications of the full RV15 sample of 244 AGN host galaxies. Our classifications consist of three categories: active-mergers, disc-dominated, and bulge-dominated galaxies.

Following visual classifications, we reject 2 Sab+Scd galaxies as they are actively merging and 9 as they are not disc-dominated; additionally, 13 S0s show clear signs of being disc-dominated (e.g. prominent spiral arms, or edge-on morphology with only a small bulge) and are moved into the disc-dominated category. By removing 11 and adding 13 galaxies from Sab+Scd we conclude that 62 of the HC11 classed galaxies are disc-dominated. Finally, following visual classification, we class 76 of the 123 unclassified-HC11 galaxies as disc-dominated galaxies.

In total, we classify 138 galaxies as disc-dominated galaxies, which we refer to hereafter as T-RV15; this includes 89 galaxies not classed as late-type in the morphological analysis of RV15. The significance of these previously mis- or unclassified is further discussed in Section 3.2.5.

3.2.2 Simmons, Smethurst & Lintott (2017)

The primary goal of the Simmons et al. (2017, hereafter S17) study was to investigate the growth rate of SMBHs within the merger-free regime. They focused on whether luminous AGN and their merger-free host galaxies are consistent with established scaling relations. The often-cited paradigm that mergers are required to rapidly grow SMBHs and drive co-evolution was the motivation behind this study.

S17 drew their initial sample from Edelson & Malkan (2012, specifically their W2R sample). W2R is comprised of 4,316 sources identified using multi-wavelength data from the Wide-Field Infrared Survey Explorer (WISE; Wright et al., 2010b), Two Micron All-Sky Survey (2MASS; Skrutskie et al., 2006) and the ROSAT All-Sky Survey (RASS; Voges et al., 1999). This method uses the multi-wavelength nature of AGN emission, specifically infrared colours and X-ray information, to

select AGN with a very high confidence rating. Sources in this sample have a confidence rating of > 95 per cent, which produced a pure yet incomplete sample. This selection also favours luminous AGN, which aligns well with the science goals of S17.

S17 cross-matched sources from W2R with galaxies from SDSS DR8 and found a match within three arcsecs for 1,844 sources, with 74% having redshifts. They limited the redshift selection to $z < 0.25$, as the morphological classifiability of disc-dominated galaxies is reduced at higher redshifts within SDSS. Following a visual inspection of the SDSS colour images, they found 137 candidate disc-dominated AGN host galaxies, of which 101 have spectroscopic observations from either SDSS (96 sources) or INT-IDS (5 sources). S17 used the same broad emission line relation method as RV15 to estimate BH mass (Greene & Ho, 2005). However, they used a recalibrated version of Shen et al. (2011). To measure total stellar mass, S17 use the relations between stellar mass, absolute galaxy r-band magnitude, and $u - r$ galaxy colour (corrected for galactic extinction; Schlegel et al., 1998). They removed the AGN contribution to the luminosity and colour of each galaxy by subtracting the flux in SDSS `psfmag` from the flux in `modelmag`. S17 derive AGN bolometric luminosities from the WISE W3 band, using the correction factor of $L_{\rm bol} \approx 8 \times L_{\rm W3}$ derived from Richards et al. (2006a), where L_{W3} is derived from:

$$L_{W3} = \left(\frac{4\pi d^2}{10^{-2}, \mathrm{m}^2}\right)\left(\frac{c}{\lambda}\right)\left(\frac{F_{\nu,0}}{1 \times 10^{23}, \mathrm{Jy}}\right) 10^{\left(\frac{M_{W3}}{-2.5}\right)}. \tag{3.1}$$

The S17 sample was subsequently targeted by an *HST* snapshot programme (HST-GO-14606; for further details see Smethurst et al., 2019; Garland et al., 2023; Fahey et al., 2025), which confirmed the strongly disc-dominated nature of the sample. We have removed the four elliptical interlopers from the original sample: the final sample from S17 that we consider contains 97 disc-dominated galaxies hosting luminous AGN. The overall sample we consider spans redshifts $0.03 < z < 0.25$ and black hole masses $2 \times 10^6 \mathrm{M}_\odot < \mathrm{M_{BH}} < 9 \times 10^8 \mathrm{M}_\odot$.

3.2.3 Bennert et al. (2021)

The Bennert et al., (2021, hereafter B21) sample comes from the fourth in a series of papers (Bennert et al., 2011; Harris et al., 2012; Bennert et al., 2015) with the stated aim of creating a robust local baseline of the black hole mass scaling relations of type 1 AGN for comparison with high redshift studies. In the fourth paper, they investigated the slope and intrinsic scatter in local scaling relations and their dependence on morphological features.

The sample of B21 was drawn from a parent sample, originally described in Bennert et al. (2011), of Type 1 AGN host galaxies identified in SDSS DR6 (Adelman-McCarthy et al., 2008) via optical luminosity and Hβ FWHM. They limited the sample to $0.02 < z < 0.1$ in redshift and $M_{\rm BH} > 10^7$ $\rm M_\odot$ in black hole mass. The redshift cut was to ensure that both the Ca triplet and a bluer wavelength region were accessible to measure stellar kinematics and that the objects were well resolved; the $M_{\rm BH}$ cut allowed B21 to focus on the detailed study of higher-mass systems, which were lacking in samples previously studied. Based on visibility during their Keck observing run, they selected 332 candidate objects, of which 111 objects were observed with Keck. B21 determined stellar kinematics for 84 galaxies in that subset. To measure stellar mass, they used five different bands (HST UVIS/$F814W$, SDSS g, r, i, z) with a Bayesian stellar-mass estimation code and with priors on age, metallicity and dust content of the galaxy. 66 of these 84 galaxies were subsequently imaged with *HST*-WFC3 and also had persistent broad Hβ emission in both SDSS and Keck/LRIS spectra.

As with the other two samples, we consider only disc-dominated galaxies where $M_{\rm bulge}/M_* < 0.3$ and where the galaxies are not actively merging. We note that our qualitative results do not depend on the specific choice of bulge-to-total ratio threshold for disc-dominated selection, within reasonable limits. Following these cuts, the subsample from B21 that we consider has 34 disc-dominated galaxies.

B21 determined the black hole masses for the sample based on the second moment of the broad Hβ emission line determined by Keck spectroscopy. The L_{5100} continuum luminosity was used as a proxy for BLR size and combined with the width of Hβ to estimate $M_{\rm BH}$. B21 derived their own virial factor (f) by matching the $M_{\rm BH} - \sigma$ relation to Kormendy & Ho (2013), resulting in

$\log f = 0.97$. B21 did not determine bolometric luminosity for their sample. In order to add bolometric luminosities for the B21 sample to Figure 3.1, we correct the WISE W2 luminosities to $L_{\rm bol}$ based on the corrections of Richards et al. (2006a). We discuss these luminosities further in Section 3.2.4 below.

3.2.4 Combining Samples

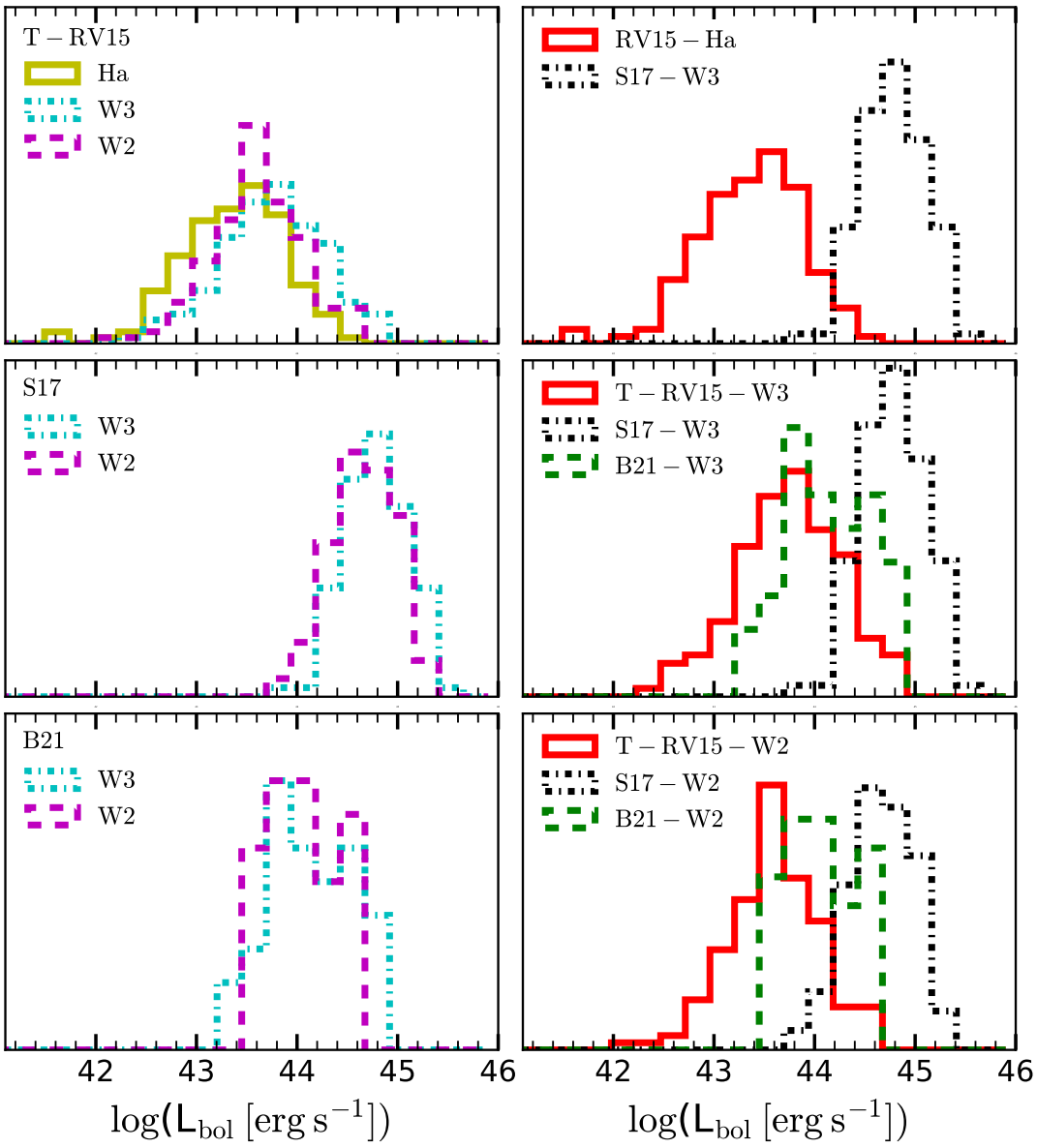

Figure 3.2: Comparison of bolometric luminosity derived by different methods. **Left:** Comparison of bolometric luminosity derived from Hα (RV15 only) in olive, W3 in cyan and W2 in magenta. RV15 is plotted at the top, S17 in the middle and B21 at the bottom. **Right:** The distributions as presented in original paper, with B21 using the W3 method. The middle plot is using W3 and on the bottom is using W2. Using the same method for bolometric luminosity estimation reduces the differences between the samples.

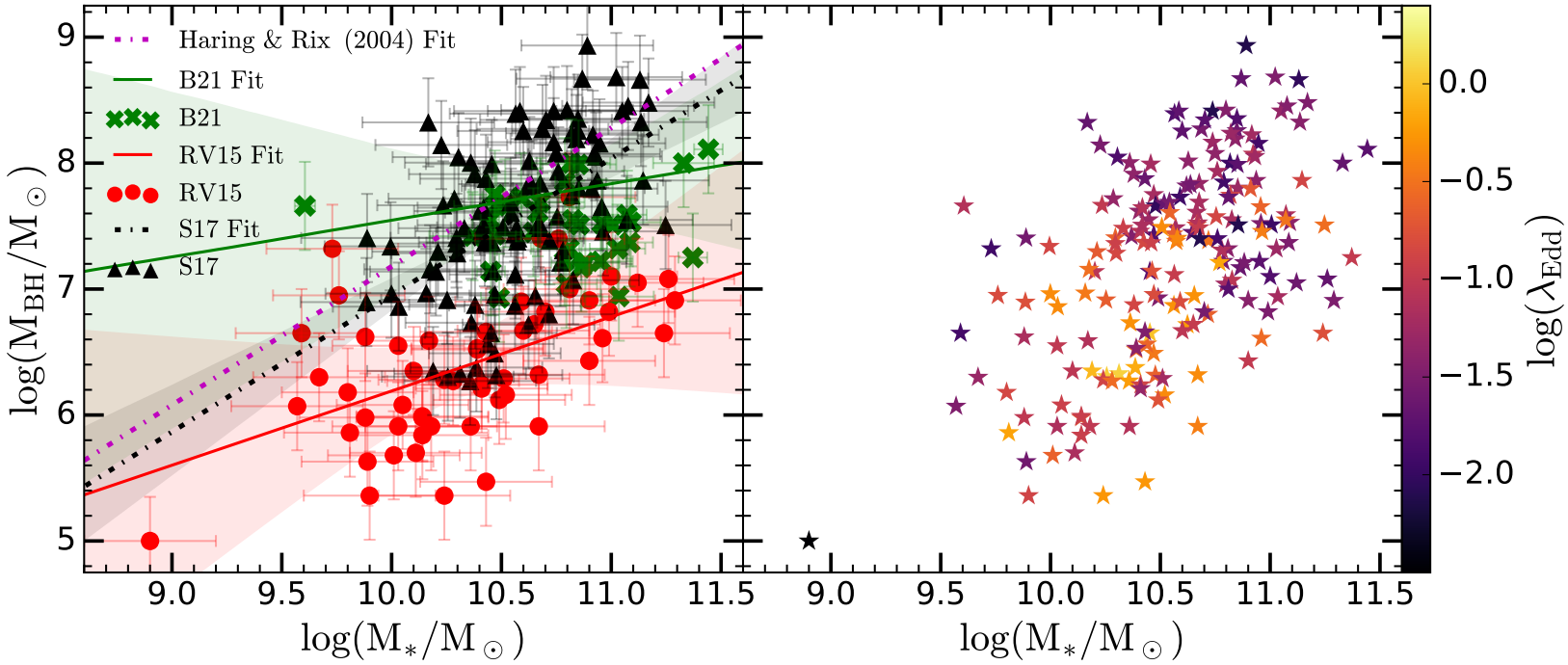

Figure 3.3: Left: Red solid line and circles represent RV15, green solid line and crosses represent B21, black dashed line and triangles represent S17. The pink dot-dashed line represents the Häring & Rix (2004) co-evolution relation. **Right:** Same as the left panel but with trend lines removed and all shapes plotted as stars for clarity and λ_{Edd} plotted as colour.he samples populating different parts of the diagram

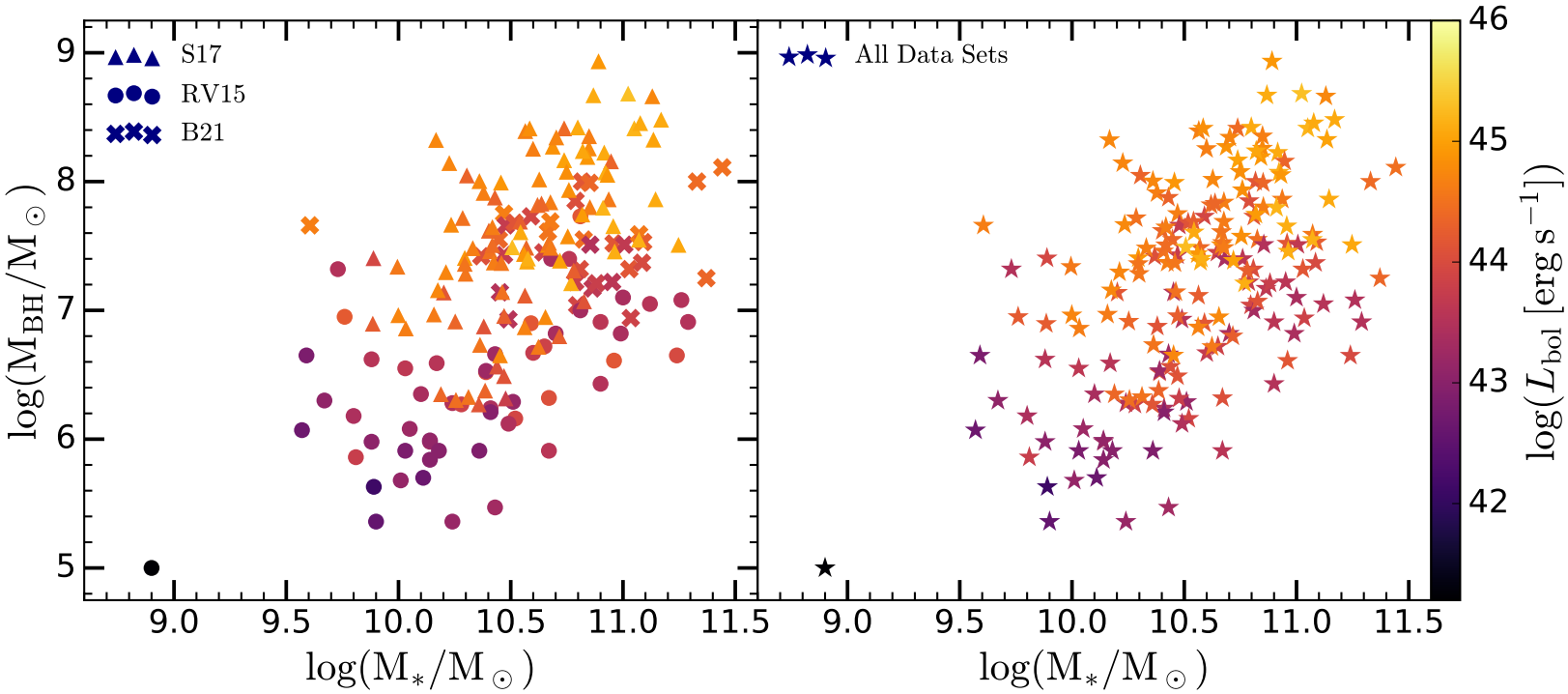

Figure 3.4: Black hole–total stellar mass relation for all three samples with colour representing L_{bol}. In the left plot, triangles represent S17, circles represent RV15, and crosses represent B21; in the right plot, they are all represented as stars. Bolometric luminosity appears to be an indicator of whether an AGN will fall on the established relation, consistent with the samples being drawn from the same underlying population.

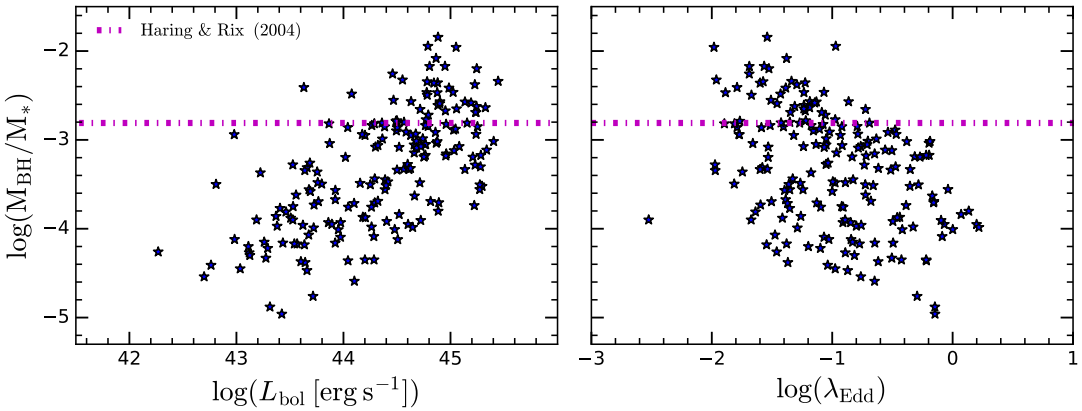

Figure 3.5: Black hole stellar mass ratio as a function of L_{bol} (left) and λ_{Edd} (right). The pink dot-dashed line represents the mean constant ratio of the local relation by Häring & Rix (2004) at 0.0015.

The three samples take different approaches to AGN bolometric luminosity. RV15 converted broad-line $L_{\mathrm{H}\alpha}$ derived from SDSS spectra to L_{5100}, then to L_{bol}; S17 converted WISE L_{W3} to L_{bol}; and B21 did not use bolometric luminosity in their analysis. For consistency across the samples we re-derive bolometric luminosities for each sample using the same method.

We use the infrared bolometric correction from (Richards et al., 2006a) to estimate bolometric luminosity, as in the S17 sample. However, as the WISE W3 12μ band has a broad throughput range at $7-18\mu$, it may be contaminated by star formation. Therefore, we also derive a bolometric luminosity from the WISE W2 4.6μ band, which has a narrower throughput at $4-5.5\mu$.

In Figure 3.2 we compare the bolometric luminosity reported by each study to luminosities derived via infrared corrections. We find a slight difference between the L_{bol} measured from W2 and W3 for S17 and B21. The L_{bol} measured from W2 is, on average, slightly lower than W3, with it being 0.1 dex and 0.05 dex lower for S17 and B21, respectively. This is well within the error of L_{bol}, which is +0.15 dex and -0.25 dex and comes from the uncertainty in the bolometric correction (Richards et al., 2006a). For T-RV15, we find an offset between the infrared and $L_{\mathrm{H}\alpha}$-derived luminosities. We find that the W2 derived luminosity is on average higher by 0.2 dex, while the W3 derived luminosity is on average higher by 0.3 dex and has a larger scatter. This offset may be due to the fact

that $L_{\mathrm{H}\alpha}$ from RV15 is the host continuum removed luminosity.

We opt to use the WISE-derived luminosity as we use L_{bol} as a third parameter in our analysis, and we want to avoid having BH mass and luminosity derived from the same measurement. Since the W2-derived luminosity aligns more closely with $L_{\mathrm{H}\alpha}$ and there is less scatter than with W3, we adopt it as the L_{bol} estimator for all samples in our analysis. However, our results do not significantly change if we adopt W3.

Each study covers different redshift ranges (Figure 3.1), which translates to sampling different volumes. This is partially responsible for the small detection overlap between the samples, with no black holes being shared between all three samples and only three appearing in at least two samples. However, of the 71 unclassified discs that appear in the T-RV15 sample but not RV15, 11 appear in the B21 sample. The $\log M_*$ - $\log z$ plot demonstrates this limited overlap. While the galaxy mass distributions of the samples are similar, with mean masses of $\log(M_*/\mathrm{M}_\odot) = 10.4$, 10.6, and 10.7 for RV15, S17 and B21 respectively, the properties of the AGN hosted in the galaxies such as BH mass, bolometric luminosity are significantly divergent. For the Eddington ratio, S17 and RV15 have similar distributions, while B21 lacks a higher Eddington ratio AGN. Most notable is the difference in BH mass, where the logged means are $\log(M_{\mathrm{BH}}/\mathrm{M}_\odot) = 6.44$, 7.60, and 7.54 for RV15, S17 and B21 respectively.

Figures 3.3 and 3.4 demonstrate how the dissimilar distributions of the samples translate to significantly different $\log M_{\mathrm{BH}}$ - $\log M_*$ relations. We plot $\log M_{\mathrm{BH}}$ against $\log M_*$ for each sample, with $\log \lambda_{Edd}$ and $\log L_{\mathrm{bol}}$ plotted as a colour gradient in Figure 3.3 and Figure 3.4, respectively. In Figure 3.3 we fit linear regression models (using a Bayesian method that includes uncertainties for both $\log M_{\mathrm{BH}}$ and $\log M_*$, as described in Kelly 2007) to each sample. As a comparison, we include the fit for a sample of early-type galaxies from Häring & Rix (2004, hereafter HR04), which have morphologies indicative of major mergers during their evolutionary history (Hopkins & Hernquist, 2009b). Comparison with this relation, considered one of the canonical black hole-galaxy relations, provides a means of comparing the merger-free samples of RV15, S17 and B21 to co-evolution attributed to merger-driven processes.

There is a significant disparity in the location of the samples in relation to the HR04 $M_{\rm BH} - M_*$ relation. The RV15 relation falls significantly below the HR04 relation, though a small number of sources lie on it. This study, taken alone, suggests that disc-dominated galaxies co-evolve differently with their central black holes than elliptical galaxies. On the other hand, the S17 sample of disc-dominated AGN host galaxies is in good agreement with the HR04 relation (consistent within 1σ), suggesting that secular processes and minor mergers lead to the same co-evolution as major mergers. Due to the small sample size and the high minimum $M_{\rm BH}$ cut, the best fit for the B21 sample is a nearly flat linear fit. However, most sources fall within 3σ of the HR04 relation, indicating significant secular growth of these SMBHs.

Considered together, these disparate samples give a conflicting view of the nature of co-evolution between SMBHs and galaxies. We plot $\log \lambda_{Edd}$ and $\log L_{\rm bol}$ as additional parameters in Figures 3.3 and 3.4 to check for commonality between the samples. There is an apparent trend in the bolometric luminosity across the combined sample. The bolometric luminosity seems to be a predictor of where a BH will lie on the HR04 relation. This can be seen in Figure 3.5, which shows the $M_{BH} - M_*$ mass ratio as a function of L_{bol}. A slightly weaker trend can also be seen in $\lambda_{\rm Edd}$. This is an observational indication that these samples may be taken from a continuous underlying population. If this is the case, it implies that sample selection and bias are the reasons for the differences between the samples. We discuss the implications of using bolometric AGN luminosity as an additional parameter in an analysis of co-evolution in Section 3.5.

3.2.5 Examining the bias of the samples

The selection function of a sample imparts a bias that affects the sample in multiple ways—some more obvious than others. Each study is careful to describe their selection choices, and most of the biases discussed below are also acknowledged and justified in the original works. Understanding these biases is critical for interpreting comparisons between the samples.

All three studies selected only Type 1 AGN, a requirement which makes lower-luminosity and lower-mass AGN slightly less likely to be selected (Merloni et al.,

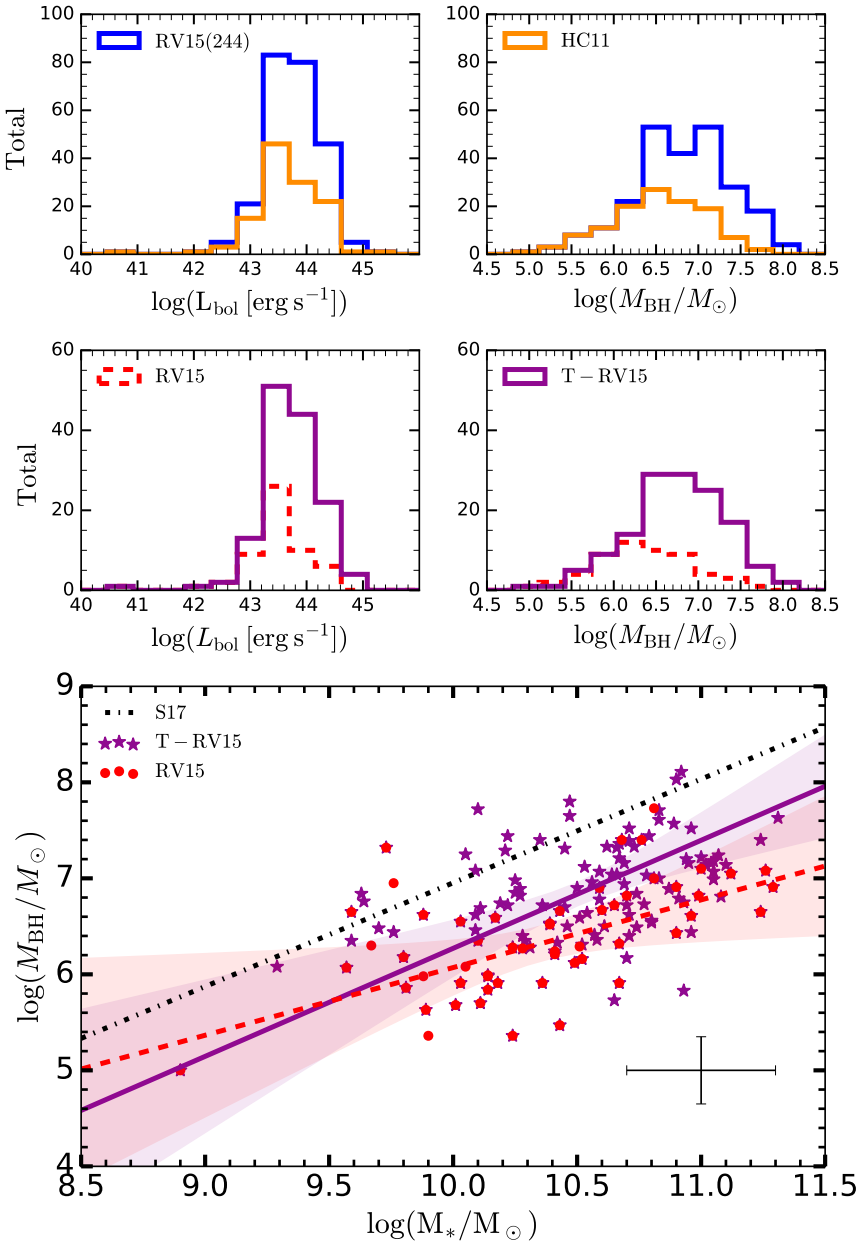

Figure 3.6: Top: The bolometric luminosity and BH mass of the original RV15 sample (blue dashed line) and the galaxies that received a classification (solid orange line). Middle: Same as above for the galaxies classified as discs in RV15 (red dashed line) and our disc classifications (solid purple line). Bottom: The BH vs total stellar mass relation for disc galaxies in RV15 (red dots and dashed line) and for our classifications (purple stars and solid line) with a 3σ error region around both. A significant number of disc galaxies were not included in the original sample; these were also more likely to be higher luminosity and mass.

2013). Moreover, all used SDSS data in their selection procedures. The reliance on SDSS spectra introduces a bias against low-mass AGN, or those whose spectra are strongly dominated by stellar emission. In such cases, components like broad Hα become increasingly difficult to identify and separate from the stellar continuum.

RV15 and S17 also used SDSS imaging to determine host galaxy morphologies, which introduces a bias against galaxies that are too small or too distant to have clearly resolved morphologies in SDSS. However, the low redshift range of the RV15 sample somewhat mitigates this bias. Furthermore, follow-up work on the S17 sample using HST found that 97 out of 101 morphological classifications were correct, suggesting their morphological classification process was robust.

Each study also introduced different biases due to their specific selection criteria and scientific goals. RV15 excluded AGN that outshone their host galaxies, biasing against high-luminosity and likely higher-mass black holes. In contrast, S17 only included AGN with at least a 95% confidence level in their multi-wavelength selection, biasing against low-luminosity AGN (and therefore also against lower-mass SMBHs). B21 applied a lower mass cut of $M_{\rm BH} > 10^7 M_{\odot}$, introducing a direct bias against low-mass AGN. These choices are each clearly described in the respective manuscripts.

There may also be less explicit selection effects within the samples. As an initial check, we reviewed the reported black hole masses for sources that are shared between studies. The mean BH mass difference between B21 and T-RV15 (11 sources in common) is $\Delta M_{\rm BH} = 0.12$ dex; between the single AGN shared by B21 and S17 it is 0.09 dex; and for the two AGN shared by S17 and RV15, the mean difference is 0.30 dex, with RV15 reporting a higher mass in both cases. This slightly larger discrepancy can be attributed to S17 using a Lorentzian fit for the Hα line profile in these sources, which typically yields a slightly lower FWHM—and hence lower BH mass—than a Gaussian fit. Notably, correcting for this difference would amplify the apparent disagreement between the RV15 and S17 results, making it unlikely to be the source of the discrepancy.

As the samples generally agree on the properties of AGN shared between them, it is unlikely that one study's measurements are systematically biased compared to the others. To further investigate, we reviewed the selection procedures of

each study for potential errors or overlooked biases. In doing so, we uncovered an unexpected mass bias in the RV15 sample, stemming from the morphological classification of galaxies.

In RV15, galaxy morphologies were assigned by cross-matching with the catalogue from Huertas-Company et al. (2011), in which morphologies were automatically assigned using a machine-learning approach trained on SDSS images. However, this catalogue only provides classifications for galaxies in the SDSS DR6 spectroscopic sample. As a result, galaxies in DR7 but not DR6 lack classifications. Moreover, the HC11 catalogue was not trained on AGN host galaxies, which may impact its applicability.

Of the 244 galaxies in the RV15 parent sample, only 121 had morphological classifications in HC11. Upon examining the 121 classified and 123 unclassified galaxies, we found that AGN in the unclassified galaxies had, on average, higher $M_{\rm BH}$ and $L_{\rm bol}$ than those in the classified group. The top panels of Figure 3.6 show that most low-mass and low-luminosity AGN received a morphology classification, whereas most high-mass and high-luminosity AGN did not. This trend is also evident when comparing RV15 late-type galaxies to T-RV15 disc-dominated galaxies, as seen in the middle panel of Figure 3.6.

This bias manifests as an offset of 0.4 dex at $M_* = 10^{10.5} M_\odot$ between the $M_{\rm BH} - M_*$ relations of RV15 and T-RV15. Many of the newly classified galaxies are consistent with the HR04 relation. While this helps to explain part of the gap between RV15 and S17, it does not resolve it entirely, indicating that other selection function differences also play important roles.

To quantify the extent to which selection functions account for the apparent discrepancies between samples, we apply them to a mock population. The synthesis of this mock population is described in Chapter 2.

3.3 Mock AGN Population Sampling

We perform four iterations of sampling on the mock population to mimic selection biases found in observational samples. We first apply any redshift or BH mass cuts specified by the observational sample for each sample selection. Next,

we construct a selection function based on each sample's bolometric flux and redshift distribution, applying a Gaussian smoothing. We impose hard limits at the extremities of the selection function. These limits effectively prevent the over-selection of samples with low flux values. This selection gives us four samplings of the mock population, which are selected using the observed samples' selection functions. These new samples are referred to as SA_RV15 for RV15, SA_T-RV15 for T-RV15, SA_S17 for S17 and SA_B21 for B21. The flux-redshift distributions are shown in Figure 3.7. The solid grey contours represent the unsampled population, the purple contours represent the sampled population, and the coloured dots represent the parent samples, following their respective colour codes.

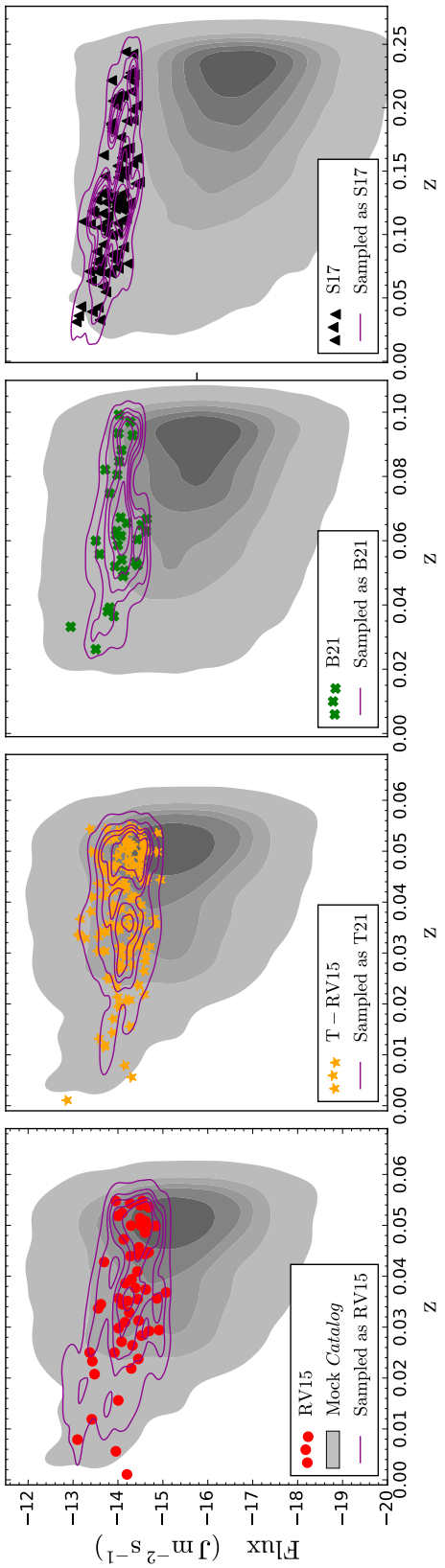

Figure 3.7: Bolometric flux vs redshift selection function, the red, orange, green and black points represent the RV15, T-RV15, B21 and S17 samples respectively. Shaded contours show the unsampled population within a redshift range corresponding to that of the observed study in each panel. The purple lines represent the mock population after sampling using the observational selection function. The parameter space sampled by each of the studies lie within the parameter space of the mock population.

Table 3.1: Results from the observed-sampled K-S test (see Figure 3.8).

Sample	p_{Lbol}	p_{MBH}	p_z	p_{flux}	$p_{\lambda\mathrm{Edd}}$
RV15	0.77	0.09	0.68	0.63	0.11
T-RV15	0.55	0.29	0.70	0.86	0.19
S17	0.70	0.52	0.61	0.83	0.39
B21	0.67	0.72	0.80	0.79	0.23

3.4 Results: Statistical reproduction of properties

Every observed sample lies within the redshift-flux parameter space of the mock population, as shown by Figure 3.7. This should be expected if the simulation is an accurate representation of the real population. In Figure 3.8 we show the normalised $\log L_{\mathrm{bol}}$, $\log M_{\mathrm{BH}}$, z, flux, and λ_{Edd} for the RV15, T-RV15, S17 and B21 samples compared to the sampled mock observations. An initial visual inspection indicates that most of the properties of the samples have been reproduced. To further quantify this, we perform a statistical analysis of these distributions. Specifically, we implement the commonly used p-values (p_{ks}) from the Kolmogorov-Smirnov (K-S) (Kolmogorov, 1933) test to see if the null hypothesis of samples drawn from the same population can be rejected. The p_{ks} are shown in Table 3.1.

Each sample's flux, redshift and luminosity are well reproduced with $p_{ks} \gg 0.05$. However, the M_{BH} of SA_RV15 has a low p_{ks} due to oversampling high mass SMBH. However, p_{ks} for M_{BH} is improved for SA_T-RV15. SA_S17 and SA_B21 show good statistical agreement, with most distributions having p values > 0.5. Overall, we find that most parameters, namely $\log M_{\mathrm{BH}}$, $\log L_{\mathrm{bol}}$ and z, have high K-S test p values. Thus, the null hypothesis cannot be ruled out; this result is consistent with the hypothesis that the seemingly disparate observed samples are drawn from the same underlying continuous population.

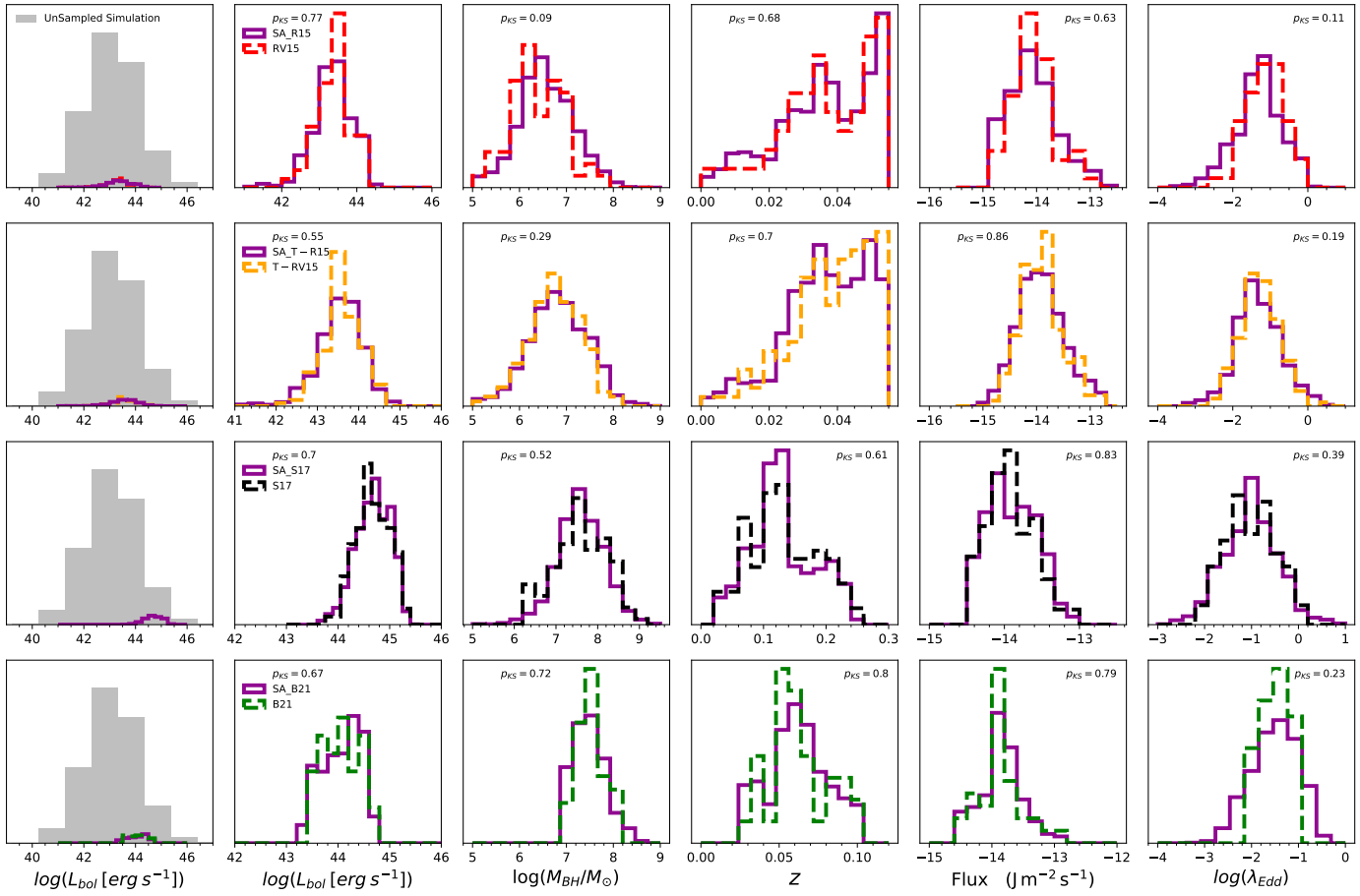

Figure 3.8: Normalised distribution of the RV15 (top), T-RV15 (top-middle), S17 (bottom middle) and B21 (bottom) samples compared to the sampled mock population. RV15 is shown as a red dashed line, T-RV15 is shown as an orange dashed line, S17 as a black solid line and B21 as a green dashed line. The sampled mock population (SA) is shown as a solid purple line and the unsampled population is shown as faded grey bars. Each row starts with the bolometric luminosity of the observational sample and the sampled mock population compared to the unsampled mock population followed by the comparison between the observed and sampled mock properties. The order of the plots is bolometric luminosity, BH mass, redshift, flux and Eddington ratio. Overall there is good statistical agreement between the observed and mock data.

3.5 Discussion

On first inspection, the three samples appear to sample three distinct populations, giving contrasting pictures of black hole–galaxy co-evolution. The discrepancy is partly explained by the fact that many high-mass SMBHs in disc-dominated galaxies were missed in the construction of the RV15 sample. Some of these missed galaxies align with the S17 and the HR04 relations. However, this is not enough to explain the difference between the samples.

By mimicking the selection of each sample on a mock population of AGN, we have shown that they are consistent with being drawn from the same underlying population (Figure 3.8). Our model did not make any prescriptions for the galaxy morphology, so these BHs are also consistent with being drawn from the whole AGN population. This reinforces the mounting evidence for the importance of secular processes in the growth of BHs. This is also seemingly consistent with recent studies such as Zhuang & Ho (2023) who found that early and late-type AGN galaxies follow the same BH–stellar mass relation.

We note that it would be beneficial to demonstrate how these selection biases impact the slope or normalisation of the recovered relation. However, our model did not include a prescription for the host galaxies. Simply assigning masses based on an assumed relation with a scatter would just recover the slope and normalisation of the assumed underlying relation when sampled through our selection functions, as they are based on redshift and AGN flux. Properly investigating the impact of these selection biases would require a simulated population of SMBHs that includes galaxy properties and a variety of underlying correlations/no-correlation mixes in the population, which is out of scope of this work.

The mock sampling implies that the differences between the samples result from each study applying different selection functions to the same population. Thus, it is appropriate to consider these disparate samples as one sample of the underlying population. In Figure 3.9 we show the M_{BH}–M_* relation for the S17, B21, and T-RV15 samples combined. As a comparison, we also include the relation from Greene et al. (2020), which is derived from dynamical

$M_{\rm BH}$measurements of local, inactive galaxies and includes both early and late-type galaxies. We also include the relation from Zhuang & Ho (2023), which is derived from low redshift ($z < 0.35$) AGN galaxies and also includes both early and late-type galaxies. Where there is overlap between samples, we adopt the values of $M_{\rm BH}$, M_*, and $L_{\rm bol}$ from the more recent of the relevant papers in order to avoid double counting. We note that other choices to avoid double-counting (e.g. averaging reported double values) do not change our results. We find that the uncertainty of the slope of our fit is consistent with both relations. Our relation can be written as:

$$\log M_{\rm BH} = (1.81 \pm 0.30) \log M_* - (11.98 \pm 3.51) \tag{3.2}$$

and has a scatter of 0.81 dex and a Pearson's correlation coefficient (Pearson, 1896) of 0.46. The quoted slope and intercept are given by the median of 10,000 draws from the posterior probability distribution of the parameters. However, as we have shown, the sample is a biased sampling of the underlying population and our relation may also be biased. We also find the trend in bolometric luminosity remains with the inclusion of the T-RV15 sample, which includes unclassified disc galaxies from the original RV15 sample.

The fact that the samples can be drawn from the same underlying population motivates us to further investigate the finding of bolometric luminosity trending across the $M_{BH} - M_*$ diagram. Taken at face value, the trend suggests that the mass of a black hole is related to the mass of the host galaxy and the luminosity of the BH. We interpret this as the BH–stellar mass relation being a planar relation with bolometric luminosity as the third parameter.

Figure 3.10 shows the BH mass - galaxy stellar mass - bolometric luminosity plane as a 3D plot. We have fitted a plane to the data using a bootstrap sampling method (sampling 10^4 times with replacement within the uncertainties of each point) and plotted a three-dimensional error region. The plane can be described by:

$$\log M_{\rm BH} = (0.33 \pm 0.13) \log M_* + (0.63 \pm 0.01) \log L_{\rm bol} - (24.14 \pm 1.50) \tag{3.3}$$

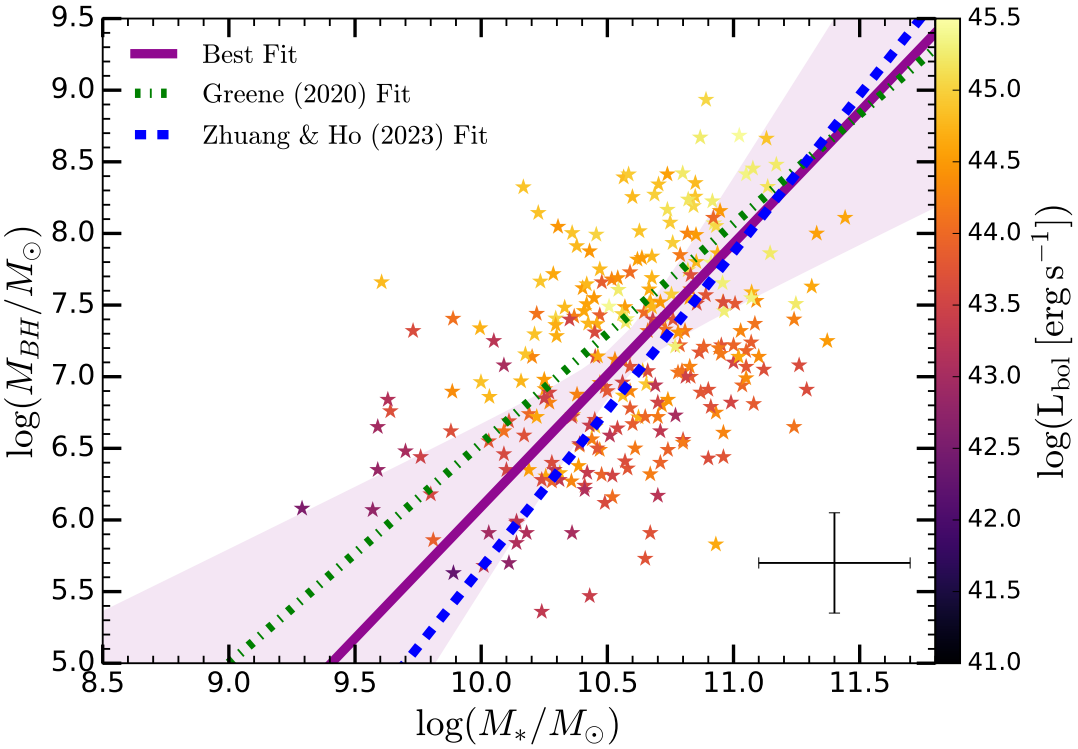

Figure 3.9: Relationship between M_{BH} and M_* for T-RV15, S17 and B21 combined. The best fit is shown as a solid purple line, and the uncertainty in the slope is shown as a purple-shaded region. The trend lines for dynamically measured SMBHs from Greene et al. (2020) and for AGN from Zhuang & Ho (2023) are shown as a green dash-dash line and a blue dashed line, respectively. The best-fit line is consistent with both the dynamical and the AGN samples.

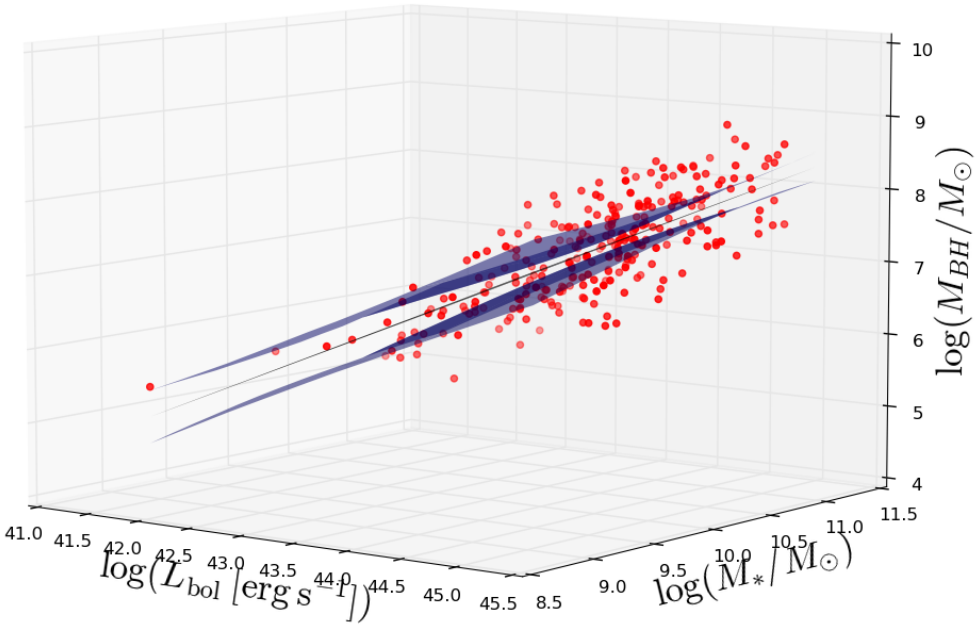

Figure 3.10: 3D plane plot of black hole mass vs total stellar mass vs bolometric luminosity. The best fit plane is plotted in black and a 3σ error region is marked by the blue planes. Figure 3.11 shows different projections of this plot in 2D. The inclusion of bolometric luminosity produces a tighter relation.

and is a much tighter relation with less scatter than the two-dimensional fit, without bolometric luminosity.

Figure 3.11 compares the BH - stellar mass relation, the BH - bolometric luminosity relation, and a projection of the plane relation on the right. Including both bolometric luminosity and stellar mass produces the tightest relation. At a given stellar mass a factor of 10 increase in $L_{\rm bol}$ corresponds to an increase in $M_{\rm BH}$ of 0.56 dex, or a factor of 3.6 increase. For a constant $L_{\rm bol}$ a factor of 10 increase in stellar mass translates to an increase of 0.25 dex, or a factor of 1.8 increase. However, the question of whether this is a fundamental plane or an observed plane arises.

Our current understanding of SMBH growth suggests that SMBHs undergo a significant amount of 'flickering', a change in their Eddington ratio on short timescales (Ulrich et al., 1997; Schawinski et al., 2015). If this is true, we would not necessarily expect the mass of a BH at a given galaxy mass to be related

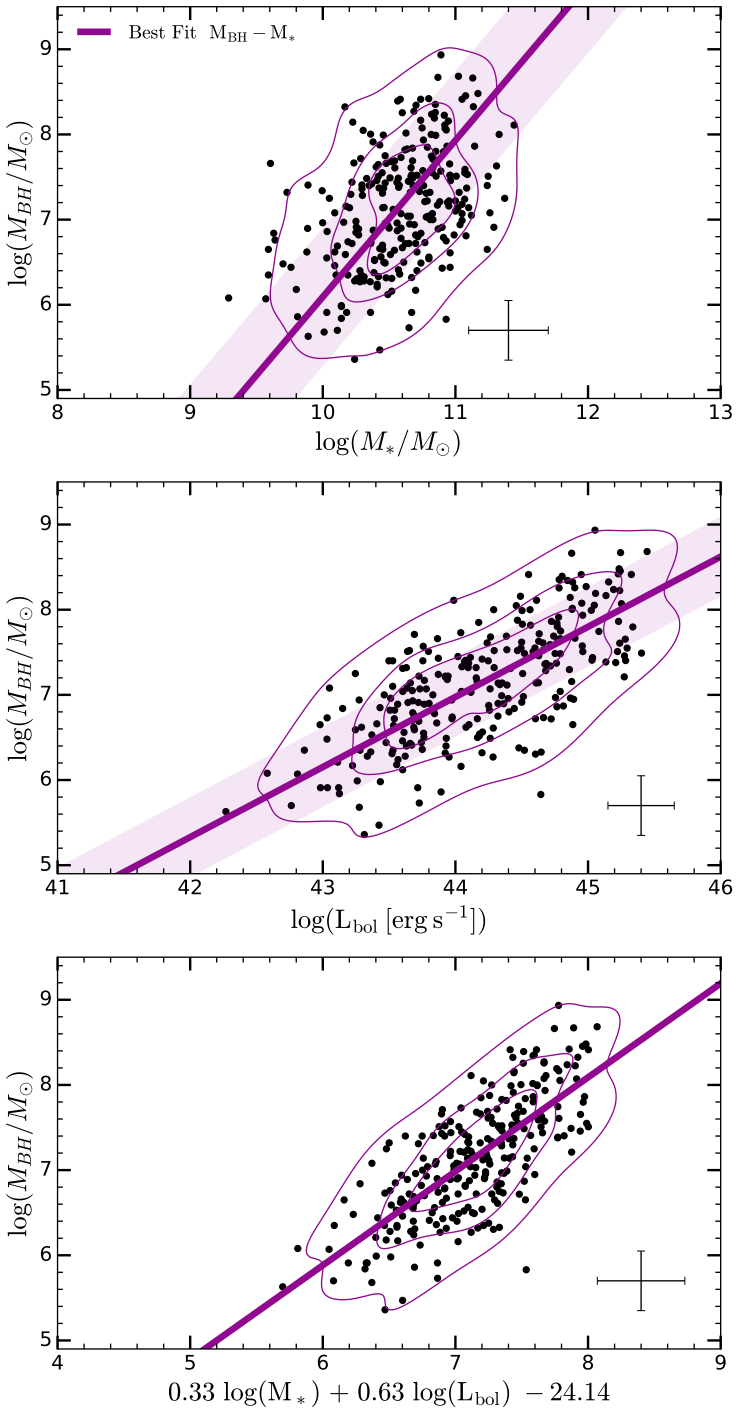

Figure 3.11: Left: Black hole - total stellar mass relation for T-RV15, S17 and B21 combined and the abundances matched relation for the mock population, Purple contour lines show distribution in each plot. **Middle plot:** Bolometric luminosity plotted against BH mass. **Right plot:** The best-fitting plane is shown in projection for the black hole - galaxy stellar mass - bolometric luminosity plane. Including bolometric luminosity as a third parameter plane produces a tighter fit with less scatter.

to bolometric luminosity in the way we have observed. Thus if this plane is in fact fundamental it would have a significant impact on our understanding of the nature of BH growth. It would suggest that the observed growth rate for an AGN is typical during its active phase. However, as bolometric luminosity directly links to the mass growth rate, we are able to determine whether it is possible for these BHs to grow to such masses within the fundamental plane model.

In order to evaluate the viability of a fundamental plane, we developed two simplistic models to assess the period of active mass growth necessary for each BH to reach its observed mass at its current bolometric luminosity starting from a seed mass of $M_{\rm BH} = 10^4\,{\rm M}_\odot$. The first model assumes that BHs grow at the Eddington limit until they reach their observed luminosity, representing a physically plausible scenario. Conversely, the second model assumes BHs grow at their current bolometric luminosity regardless of the Eddington limit. In Figure 3.12 we plot BH mass against the ratio between growth time and the Hubble time for both plots. This ratio is analogous to the duty cycle, which is the fraction of time a BH is active. A duty cycle of 10% is often cited as typical. In both models, a large number of BHs require atypically high-duty cycles, with some requiring a period much longer than the age of the Universe to grow their black holes to the given masses at the observed luminosity.

These two models are idealised scenarios, yet they suggest unreasonably high-duty cycles. Therefore, it is likely that the dependence on bolometric luminosity is a selection effect and that probing lower magnitudes would diminish this observational plane. This will become significantly easier with deeper surveys and with upcoming activations of the next generation of telescopes.

As we have discussed, each sample is inherently biased in different ways, which has resulted in the sampling of different regions of the BH mass - stellar mass - bolometric luminosity parameter space, which when viewed together gives rise to the plane relation in Equation 3.3. The S17 sample was biased towards high luminosity BHs which, in turn, biases against low-mass BHs. For a given flux limit, a lower BH mass requires a higher Eddington ratio for detection, resulting in the lowest mass BHs in the S17 sample being near or super Eddington. Therefore, AGN hosted in lower mass galaxies in the S17 samples are likely to be closer to HR04 relation and have a higher bolometric luminosity. Moreover, due

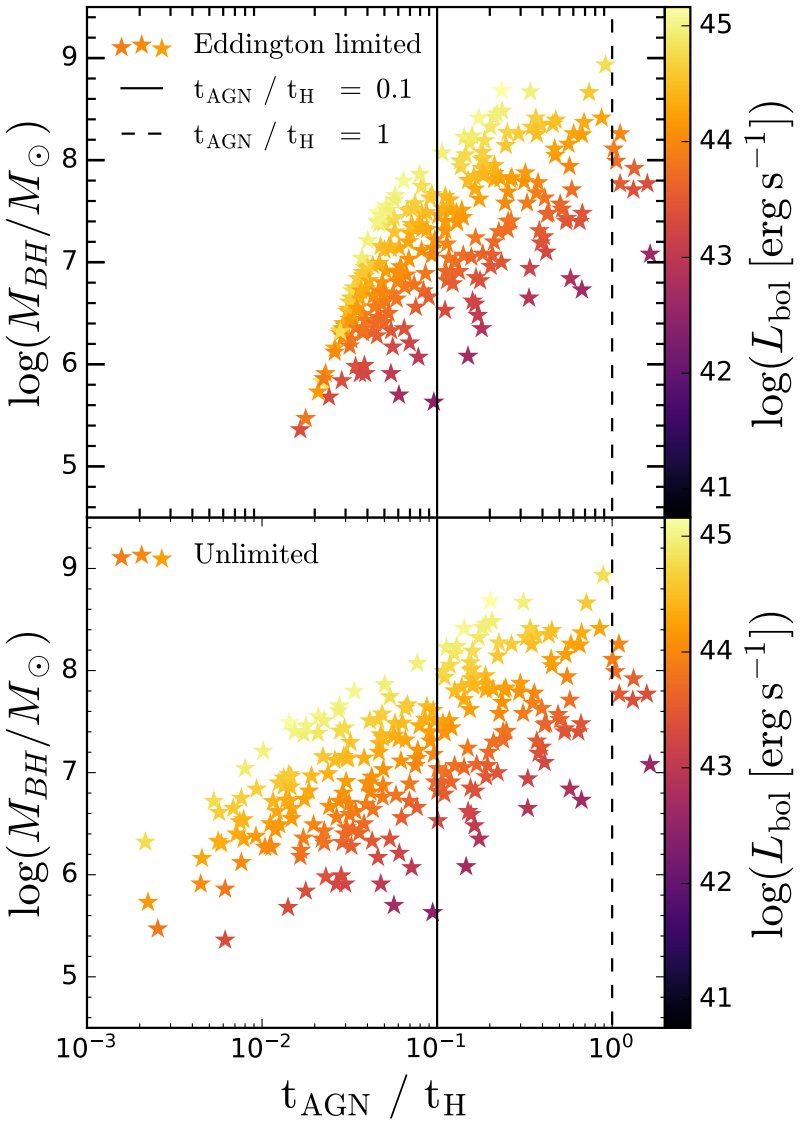

Figure 3.12: Black hole mass versus time taken for a BH to reach its mass at its current growth rate as a fraction of the Hubble time (analogous to a duty cycle). Points are T-RV15, S17 and B21 combined; points are coloured by bolometric luminosity. The solid vertical line represents a BH being active for 10% of the Hubble time and the dashed line represents activity duration equal to the Hubble time. Top: The Eddington limited model. Bottom: Unlimited growth model (super-Eddington growth possible). A significant number of these BHs require growth times which are either much longer than expected or physically impossible in these idealised scenarios; thus it is likely these BHs have previously grown at much higher rates.

to the decrease in flux intensity with distance, higher redshifts required higher luminosity for detection. Despite the fact that higher luminosity BHs have a lower number density (see luminosity functions, e.g. Aird et al., 2015; Fotopoulou et al., 2016), the increasing volume with redshift means higher luminosity BHs are likely to be detected, whereas low luminosity AGN are less likely to be detected. These higher redshift high luminosity AGN are likely to be of higher mass, which are likely in higher stellar mass galaxies. Therefore, high-mass galaxies in the S17 sample are likely to be closer to HR04 relation and have a higher bolometric luminosity.

The bias in the RV15 sample was against highly luminous and thus, massive BHs, which was partly amplified by bias in using the HC11 catalogue. While the additional AGN from our reclassification increased scatter in the relation, it still persists. RV15 was also able to probe lower BH masses than the other samples and probed the smallest volume due to the redshift cut and searching for low-velocity broad lines. This resulted in RV15 galaxies likely to host low-bolometric luminosity AGN that lay below the HR04. Finally, B21 contains a mass cut of $M_{\rm BH} > 10^7$ $\rm M_\odot$, which results in a sample containing higher mass BHs than the RV15 sample, while the lower redshift cut than S17 resulted in less high mass/luminosity BH detections. Therefore, the B21 sample populated the space between the S17 and RV15 samples. The combination of the selection effects of these samples results in an observational plane that forms between $M_{\rm BH}$, M_*, and $L_{\rm bol}$.

This observational plane can potentially be used as a rough predictor of BH mass when stellar mass and AGN bolometric luminosity are known. This could be useful in samples of heavily obscured AGNs, where other mass estimates are unavailable and measurements of L_{5100} are not possible. However, using this plane (or any luminosity-based plane) to predict black hole masses must consider whether the selection function of the new sample is similar enough to that of the sample(s) used to create the plane for the predictions to apply. For example, this plane might be useful in predicting black hole masses for obscured AGN drawn from SDSS data once a correction for the different selection functions of obscured versus unobscured AGN is applied to both the predicted values and the uncertainties. However, there are expected intrinsic differences in observed

masses and luminosities of Type 1 vs 2 AGN that might systematically bias such a process. Applying a plane like this to predict black hole masses in the next generation of deeper extragalactic surveys would first require careful consideration of the new AGN and galaxy selection functions.

It is clear that AGN hosted in disc-dominated galaxies are a complex and diverse population. The population consists of over-massive, highly accreting BHs as well as under-massive, slowly accreting BHs, in galaxies of similar mass and morphology. This raises the question of the fundamentality of the $M_{\rm BH} - M_*$ relation and whether these three samples represent the whole population or merely the limit of detectability. If the true relation extends down to BH masses on the order of $10^4\,{\rm M}_\odot$, they will fall below the detection threshold for S17 and B21; however, it is not immediately clear why RV15 would be limited to $M_{\rm BH} > 10^5\,{\rm M}_\odot$. It may be due to the use of narrow-line diagnostic diagrams in classifying AGN, which compare emission line ratios in a galaxy to determine whether AGN or star formation is dominant. However, as highlighted by Cann et al. (2019), black hole mass can affect location on these diagrams, potentially moving systems into the composite or H2 region, as demonstrated by the dwarf galaxies missed in the initial RV15 analysis. Therefore, it is difficult to conclusively rule out the existence of such low-mass BHs. However, recently, (Mezcua & Domínguez Sánchez, 2024) showed that using BPT diagrams with integrated SDSS spectra misses 80% of $M_{BH} < 10^6 M_\odot$ AGN detected with resolved spectroscopy and pixel by pixel BPT analysis.

It is clear that major merger histories are not the only determining factor of the location on the galaxy-black hole diagram. Detailed investigation of the internal structure, low surface brightness features, composition and local environments, as well as more comprehensive and inclusive AGN selection with current and next-generation instruments, may elicit more subtle correlations in this parameter space. Moreover, it is not clear how this population folds into the general AGN population. Graham & Sahu (2023) explain how under-massive BHs in discs form due to mergers reforming discs; however, it is not clear where over-massive BHs in disc-dominated and bulgeless galaxies fit in. This is compounded by the fact that our mock observations suggest that AGN in disc-dominated galaxies have properties consistent with the population as a whole. In regards to comparisons

between simulations and observations, this study emphasises the need for careful analysis of the selection effects in the observational sample used as a comparison or for tuning to local relations.

3.6 Summary and Conclusion

We investigated the role of selection effects in shaping the $M_{\rm BH} - M_*$ relation for three samples of disc-dominated Type 1 AGN host galaxies. The three samples are from Reines & Volonteri (2015) (RV15) containing 65 AGN, Simmons et al. (2017) (S17) containing 97 AGN, and Bennert et al. (2021) (B21) containing 34 AGN. They all drew galaxies from SDSS and measured the BH mass using broad emission lines. Although they are all low redshift, they span different low-redshift ranges: RV15 covers $0.001 < z < 0.055$, B21 covers $0.026 < z < 0.10$, and S17 covers $0.031 < z < 0.25$, significantly reducing overlap between them.

For AGN detection and classification, RV15 employed BPT diagrams, S17 used multi-wavelength classifications from Edelson & Malkan (2012), which included infrared colours and X-ray information, while B21 used X-ray emission and SDSS spectra. We visually classified the host galaxy morphologies for each study and only included those that we determined to be disc-dominated. Additionally, for B21 we applied a constraint of $B/T \leq 0.3$. This included the visual classification of 252 galaxies in the RV15 study, resulting in the identification of an additional 81 disc-dominated galaxies. This resulted in a sample of 138 galaxies, which is referred to as T-RV15. The unclassified galaxies in RV15 are on average more massive and luminous than the classified galaxies, which creates a bias in the RV15 sample, resulting in a $M_{\rm BH} - M_*$ that differs by 0.4 dex in $M_{\rm BH}$ at a stellar mass of $10^{10.5} M_*$.

However, this does not resolve the difference between the relations of the samples, which have seemingly similar galaxies yet they produce different scaling relations. Bolometric luminosity seems to trend across the sample, suggesting a continuous population, which can be interpreted as samples being drawn from the same underlying population. This is reinforced by our mock population producing

similar distributions when the observed flux-redshift functions are applied. Moreover, the mock catalogue was not tuned for morphology, suggesting the samples are consistent with being drawn from the entire galaxy population.

In a further review of the bolometric luminosity trend, which links the samples, we find that it tightens the $M_{\rm BH} - M_*$ relation when included as the third parameter, to form a $M_{\rm BH} - M_* - L_{\rm bol}$ plane. However, this is an observed plane, as opposed to a fundamental plane, as the required growth histories of many of the BHs are inconsistent with the plane relation. The plane likely arises from the combination of the selection effects when the three samples are viewed together. Moreover, BH mass and bolometric luminosity are estimated using the luminosity relations, so a relation between them is not surprising and justifies using bolometric luminosities and BH masses derived from different wavelengths. However, the relation is tightest with the inclusion of all three parameters. This observed plane may be useful as a mass predictor where there is difficulty determining BH mass for studies with parameters similar to this one. However, we urge caution as it is not a fundamental plane.

Overall, bulge/disc morphology, which is strongly connected to merger history, cannot be the only factor in driving black hole growth, as morphology is not a reliable indicator of where a galaxy will sit on the $M_{\rm BH} - M_*$ relation. Furthermore, the physical origin of these differences is not clear; further work exploring their environments, internal structure, composition, and larger and/or more inclusive selections with future and current surveys (*HSC*, *JWST*, *Euclid*, *Roman*, etc.) may shed light on the driving force behind the populations.

Chapter 4

Morphological dependence of the Black hole Bulge and Total stellar mass relations

4.1 Introduction

In Chapters 2 and 3, we established that disc-dominated Type 1 AGN host studies are consistent with being drawn from the overall SMBH population rather than having different underlying SMBH properties than those hosted in galaxies with other morphologies. This provides yet more evidence that SMBH-galaxy co-evolution may be dominated by whatever processes dominate the overall growth of SMBHs, but these chapters did not directly probe the relationship between bulge growth and SMBH growth.

Given the evidence that mergers may not be dominant in driving either SMBH or bulge growth, determining the dependence of bulge to total stellar mass (B/T) ratio on the $M_{\rm BH}$ – M_* and the $M_{\rm BH}$ – $M_{\rm bulge}$ relations could give important insights into the nature of co-evolution. Understanding the structural differences between inactive and AGN host galaxies can also give insights into AGN activation and co-evolution. Recent studies have suggested that the sizes of AGN host

galaxies lie between those of star-forming galaxies (SFGs) and quiescent galaxies (QGs) (Silverman et al., 2019; Li et al., 2021, 2024), the latter defined as systems with $\log(\mathrm{sSFR}/\mathrm{yr}^{-1}) \equiv \log(\mathrm{SFR}/M_*) < -11.5$. This suggests that compaction processes may be linked to AGN activation.

Part of the difficulty in comparing the bulge and the total stellar mass relations arises from the challenge of accurately determining bulge mass, especially in the presence of a highly luminous AGN. One primary method for measuring bulge mass is two-dimensional (2D) image decomposition, where the AGN point source (PS) is modelled as a point spread function and galaxy components such as bulges, discs, and bars are represented by different light profiles (most commonly Sérsic 1968 profiles; *e.g.*, Simmons & Urry, 2008; Kim et al., 2008; Bruce et al., 2016). Accurate decomposition of structural components requires spatial resolution that large-scale surveys, like the Sloan Digital Sky Survey (SDSS) and the Panoramic Survey Telescope and Rapid Response System (Pan-STARRS) (Chambers et al., 2016), cannot achieve beyond the very local universe. While the *Hubble Space Telescope* (*HST*) offers exceptional spatial resolution and a well-understood PSF, it is limited by its field of view which restricts the sample size. In contrast, the 8m class ground-based telescope *Subaru* and its Hyper Suprime-Cam (HSC) provide much higher resolution than SDSS and Pan-STARRS, with a median seeing of 0.6 arcsec and area coverage of 1200 deg^2, significantly larger than *HST* surveys. This allows for structural analysis of a large sample of luminous Type 1 AGN (Kawinwanichakij et al., 2021).

In this study, we compare the $M_{\mathrm{BH}} - M_*$ and the $M_{\mathrm{BH}} - M_{\mathrm{bulge}}$ relation and investigate the dependence on morphology, through the B/T ratio, for 415 Type 1 AGN at $z < 0.35$ using data from HSC. We also investigate the $M_* - R_{eff}$ relation as a function of morphology. We use multiwavelength 2D decomposition to reliably estimate stellar mass and multi-component 2D decomposition to estimate the B/T ratios of the galaxies. As reliable measurements of B/T and other parameters are fundamental to this study, we run an extensive analysis on synthetic AGN to estimate errors for each galaxy. This is done by matching AGN host galaxies to at least 15 inactive galaxies across nine metrics and manually adding an artificial point source, scaled to match the point source to the bulge flux ratio. In Section 4.2, we describe our sample selection and measurements

of BH properties. In Section 4.3 we describe our analysis of the HSC sample, using 2D image decomposition to separate the light from the AGN, the bulge, the disc, and the bar components. We also describe our total and bulge stellar mass estimation. In Section 4.4 we describe the construction and analysis of the synthetic AGN sample. In Section 4.5 we present our results and discuss findings regarding the relations between the mass of the BH and that of the total and bulge stellar mass and the error analysis. We also discuss the mass-size relation for our AGN sample. Finally, in Section 4.6 we summarise our results and give our conclusions. Where necessary, we adopt a cosmology consistent with Λ CDM, with $H_0 = 70$ km s^{-1} Mpc^{-1}, $\Omega_m = 0.3$ and $\Omega_\Lambda = 0.7$.

4.2 Data

4.2.1 Imaging Data

The imaging used in this study is from the third data release of the HSC *Subaru* Strategic Program (HSCSSP) survey (Aihara et al., 2018a, 2022). The HSC is a wide-field imaging camera installed at the prime focus of the *Subaru* 8.2m telescope. The HSC-SSP survey consists of three components; in this work we utilise the Wide layer which covers on the order of 1200 deg^2 in five broad-band filters (Kawanomoto et al., 2018). The 5σ limiting point-source magnitudes are $g = 26.5$, $r = 26.5$, $i = 26.2$, $z = 25.2$, and $y = 24.4$ mag. The typical seeing is $0.79''$ in g, $0.75''$ in r, $0.61''$ in i, $0.68''$ in z, and $0.68''$ in y. We create a catalogue of $z < 0.35$ HSC galaxies by querying the main HSC catalogue using the following criteria for each of the five optical bands:

1. `specz_redshift` < 0.35
2. `isprimary` = True
3. `nchild` = 0
4. `pixelflags_edge` = False
5. `pixelflags_bad` = False

6. `pixelflags_crcenter` = False

7. `pixelflags_bright_object` = False

8. `pixelflags_bright_objectcenter` = False

These selection criteria ensure there is no duplication and that objects affected by cosmic rays, nearby bright objects, or saturation are excluded. This resulted in a sample of 362,962 galaxies.

Figure 4.1 shows a random selection of 40 HSC i-band images of AGN host galaxies ranging from $z = 0.07$ to $z = 0.33$. The mean redshift of the sample is $z = 0.20$ with minimum and maximum values of $z = 0.05$ to $z = 0.35$ respectively.

4.2.2 Broad-line AGN Sample

We draw our AGN sample from two Type 1 AGN catalogues, the Sloan Digital Sky Survey (SDSS) DR16 QSO catalogue (York et al., 2000; Lyke et al., 2020) and the catalogue from Liu et al. (2019, hereafter LIU19) which is based on SDSS DR7 (Abazajian et al., 2009) spectra and was used by Zhuang & Ho (2023, hereafter ZH23). We opt to use both catalogues as their differing selections and increased area in DR16 resulted in some AGN only being selected by one catalogue. We cross-match both catalogues to within $1''$ of the HSC sample with i-band images. The HSC-LIU19 cross-match produces 582 matches and the DR16 catalogue produces 388 matches, of which 235 are not in LIU19, giving 817 candidates.

To ensure reliable structural fitting in the image decomposition, we perform visual inspection of all galaxies and exclude those undergoing mergers, exhibiting irregular morphologies, or are affected by line-of-sight superpositions. This results in the removal of 184 galaxies from the sample giving 633 candidates. However, 51 of these galaxies are not covered in all 5 HSC bands.

While we draw our initial sample from the two catalogues, we perform our own analysis of the SDSS spectra, using a method described in detail in Ren et al. (2024) and briefly outlined below.

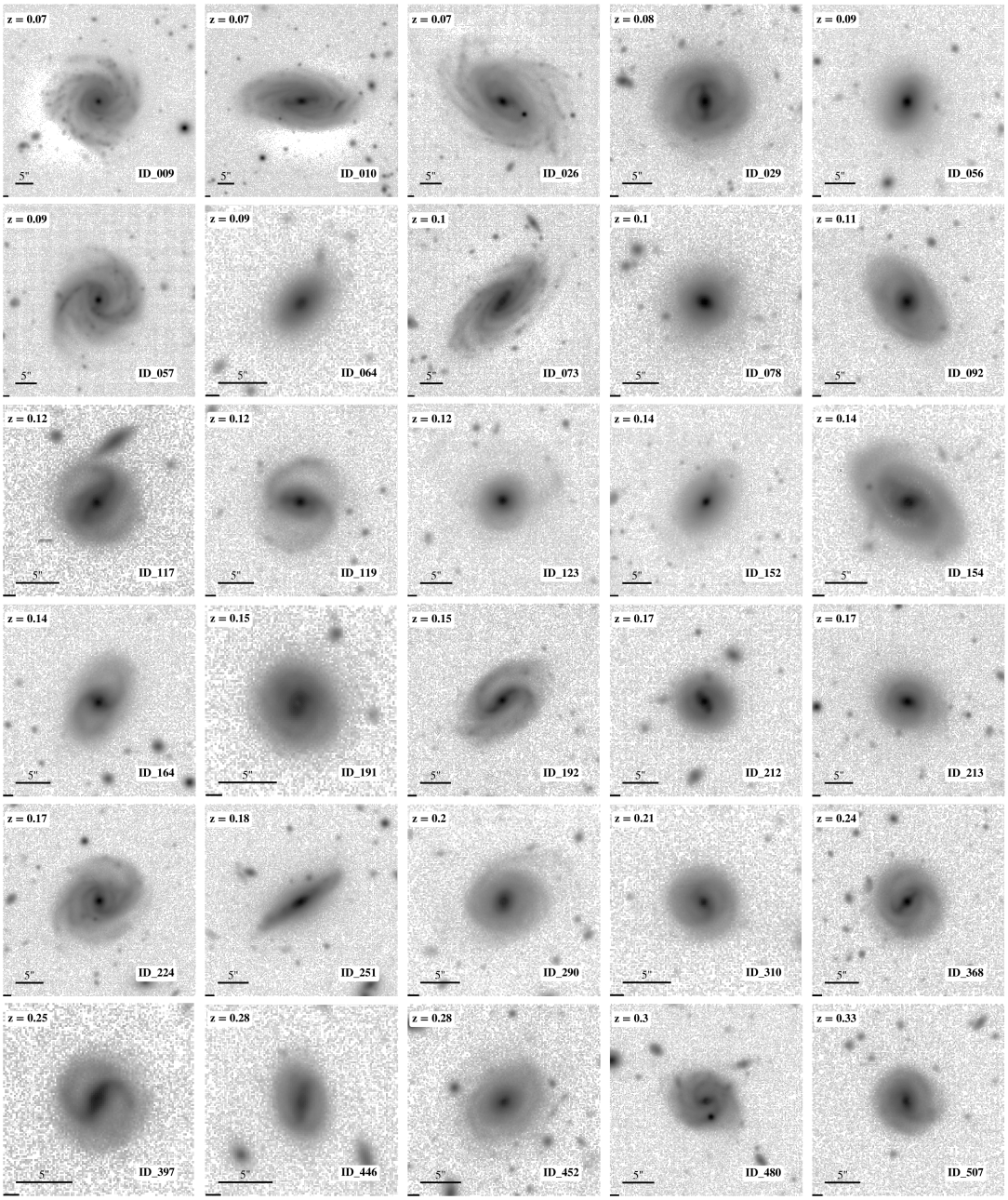

Figure 4.1: A selection of HSC *i*-band images of AGN host galaxies across the redshift range of the sample with point sources removed.

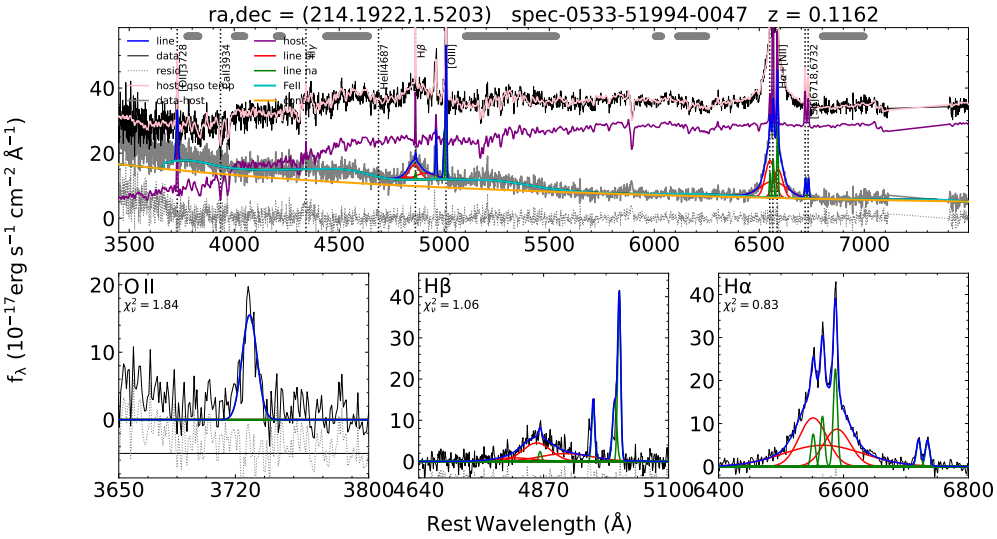

Figure 4.2: Spectrum of a broad-line AGN fit using `PyQSOFit`. The top panel shows the fit to the entire spectrum, with the original data shown in black, the host galaxy model shown in purple and the QSO model (Total - Host galaxy) shown in grey. The bottom panels show zoomed in continuum-subtracted fittings of, from left to right, [O II], Hβ + [O III], and Hα + [N II] + [S II]. In the lower panels, broadened individual lines are shown in red, and narrow lines are in green, with the overall line fit in this region shown in blue.

4.2.2.1 Spectral Analysis of Broad-line AGN

We decompose AGN and host galaxy emission using principal component analysis (PCA) combined with a penalized pixel fitting mechanism using the quasar spectral fitting software `PyQSOFit` (Guo et al., 2018). This method markedly improves the fitting of data with low signal-to-noise ratios (SNR), which typically suffers from degeneracy and over-fitting Ren et al. (2024). In Figure 4.2 we show an example fit of an AGN host galaxy spectrum.

4.2.2.2 Black Hole Luminosity and Mass

To estimate the bolometric luminosity ($L_{\rm bol}$), we use the rest frame 5100Å continuum luminosity (L_{5100}) with host emission removed and a bolometric correction from Richards et al. (2006b) such that $L_{\rm bol} = 9.26 L_{5100}$. We utilise the single-epoch virial BH mass estimation method (Vestergaard & Peterson, 2006), which

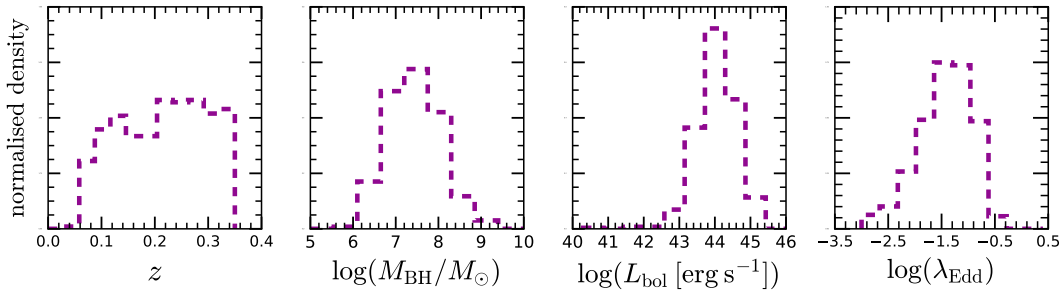

Figure 4.3: General properties of the 415 AGN in the sample. The panels show the normalised distributions of redshift (z, far left), black hole mass ($M_{\rm BH}$, centre left), bolometric luminosity ($L_{\rm bol}$, centre right) and Eddington fraction (λ_{Edd}, far right).

is based on the kinematics of the broad-line region being dominated by the mass of the SMBH and the radius being related to the luminosity (Bentz et al., 2013). For our estimation we use the rest frame Hβ broad emission line width and the 5100Å luminosity, following the host-corrected recipe from Shen et al. (2023):

$$\log\left(\frac{M_{\rm BH}}{\rm M_\odot}\right) = a + b\log\left(\frac{L_{5100}}{10^{44}\ \rm erg/s}\right) + c\log\left(\frac{\rm FWHM_{H\beta}}{\rm km/s}\right) \tag{4.1}$$

where, from Shen et al., $a = 0.85$, $b = 0.5$, and $c = 2$.

The uncertainty in $M_{\rm BH}$ is given by the propagation of uncertainties in L_{5100} and $\rm FWHM_{H\beta}$. The use of conversion factors in these estimations induces additional uncertainties. Therefore, we adopt an additional 0.35 dex uncertainty in BH mass in our sample (Shen et al., 2023).

4.2.2.3 Spectral Analysis Comparison

Both the initial AGN catalogues are derived from large-scale batch fits. In particular, the catalogue of LIU19 was constructed to include low mass and luminosity AGN, which may lead to fitting outflows as broad lines. Moreover, their sample uses $H\alpha$, where $H\beta$ is not detected, while we only use $H\beta$. We find that in the majority of cases where our measurements differ, the reason is poor fitting in the other catalogues. We also visually inspect every AGN fit in our sample

and remove galaxies with poor fits, which removes 147 AGN. However, we note that just adopting the DR16 and LIU19 samples and their measurements (*i.e.,* skipping the additional data cleaning and correction steps) does not change our qualitative results.

In Figure 4.4 we compare BH mass and luminosity for our fits with the measurements from ZH23. We also include a comparison with the BH mass formula from Vestergaard & Peterson (2006, hereafter VP06), which does not correct for host contributions, leading to higher estimations of BH mass. We find that the mass is in good agreement, with our measurement being slightly less massive by 0.1 dex on average. However, there is more scatter in the luminosity measurement, with our measurements being lower by 0.23 dex on average. We note that we find no dependence on morphology impacting the differences between the two fitting processes.

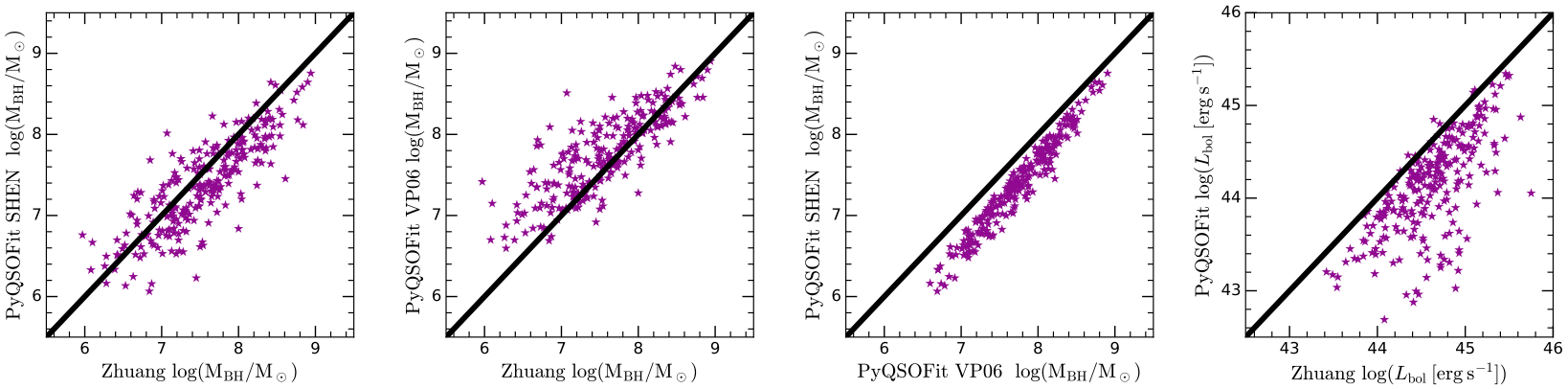

Figure 4.4: The BH properties of the sub-sample with measured properties in ZH23. **Far Left:** BH mass measured using the Shen et al. (2023) formula in PyQSOFit (Equation 4.1) against the ZH23 BH measurements. The median offset is 0.1dex. **Centre Left:** Same as the previous plot but with the VP06 formula; the median offset is 0.2dex. **Centre Right:** BH mass from PyQSOFit using the Shen et al. and the VP06 formulae; the median offset is 0.2dex and highlights the effect of host contamination. **Far Right:** Bolometric luminosity from PyQSOFit and ZH23; the median offset is 0.23dex.

4.3 Image Decomposition

For 2D host decomposition we use the Python-based open-source package GALIGHT (Ding et al., 2021) which provides astronomical data processing tools and performs 2D profile fitting. The GALIGHT 2D profile fitting process is based on LENSTRONOMY (Birrer & Amara, 2018). GALIGHT determines the best fit using Particle Swarm Optimization (Kennedy & Eberhart, 1995) and χ^2 minimisation. In our fits we model the AGN as a scaled PSF and the galaxy components as Sérsic profiles (Sérsic, 1968). We use the PSF generated from the HSC pipeline HSCPIPE v6.7 (Bosch et al., 2018), which uses around 70 stars in the field to characterise the PSF on the CCD (Aihara et al., 2018b; Coulton et al., 2018). To prepare our data for fitting we manually select the radius of the image cutout to ensure the host flux, as well as any companion galaxies, are within the frame.

4.3.1 AGN Host Image Decomposition

We first run a PSF plus single Sérsic fit. To ensure realistic results, we limit the Sérsic index (n) to be within $n \in [0.3; 9]$, which comfortably encloses physical values and reduces catastrophic fitting failures (Ding et al., 2020). This initial fit produces a model of the host and the point source. We then subtract the modelled point source and any companion galaxies from the original image to make a pure galaxy image. We use this pure galaxy image as the input image for the subsequent fits to get constraints on the multi-component galaxy fits. In the final run, we apply a multi-component AGN host fit using the best parameters of both the galaxy and AGN as initial parameters in a fit with multiple galaxy components and an AGN point source in place.

GALIGHT stores information relating to a component in *data_process.apertures*, which includes its position, size, ellipticity, and orientation. We refer to this data product as the aperture and use it to inform the initial conditions of subsequent fits. To increase the chance of finding a global minimum, not a local one, we perform two bulge-disc fits with different starting parameters for the bulge and the disc. In the first run we use the single Sérsic aperture result as the disc starting aperture and add a smaller and round aperture for the bulge. In the

second we used the single Sérsic result as the bulge aperture and applied a larger aperture for the disc initial conditions. For both fits we set the n of the disc component to 1 and set a range for the bulge as $n \in [1; 9]$. We impose constraints such that the disc is required to be larger and more elliptical than the bulge, and the effective radius of the bulge is forced to be between 5% and 95% of the disc's radius. In the majority of cases, the two fits converged; however, in some cases a different starting position will produce a significantly improved fit, based on visual inspection and χ^2 analysis.

For galaxies exhibiting a visual indication of a bar, we apply two fitting methods with different initial conditions. The first method is to take the disc aperture from the Bulge-Disc fit as the initial condition of the bar and place a larger and less elliptical aperture as the initial condition of the disc. The second method is to use a scaled-down version of the disc as the bar initial condition and to use the previous disc fit and the initial conditions for the disc. For both fits we use a circularised version of the bulge from the Bulge-Disc fit as the initial condition of the bulge. We use the parameter constraints from the Bulge-Disc fit as well as additional constraints of the bar being smaller and more elliptical than the disc. Bars typically have a flat central profile that quickly truncates at higher radii, for this reason they are often fit with a Sérsic index of 0.5 (Peng et al., 2002; Gadotti, 2009; Bennert et al., 2021). However, they can range between $0.2 \lesssim n \lesssim 0.8$ (Kruk et al., 2018). After experimentation we find constraining the bar to $n \in [0.3; 0.8]$ produces the most reliable results. As with the Bulge-Disc fitting the two bar fits converged in most cases; however, where they did not, we found that the former method most reliable for galaxies with strong bars that dominate the centre of the galaxy, while the latter is more reliable for galaxies with weak bars.

After fitting the point-source-removed galaxies, we select the best fit based on the Bayesian information criterion (BIC; Kass, R. E 1978) and visual inspection. BIC provides a balance between goodness-of-fit and model simplicity, making it well-suited for distinguishing between models of varying complexity. We use BIC because χ^2 analysis alone is unsuitable to this kind of analysis, as adding additional components will reduce χ^2 in most cases, which can cause over-fitting.

BIC helps to limit over-fitting, since it accounts for the number of free parameters (k) and data points (N). The formula for BIC is given by:

$$\mathrm{BIC} = \frac{1}{2}\chi^2 + k\ln(N) \tag{4.2}$$

We adopt the criteria from Kass & Raftery (1995), where BIC has to improve by a value of 10 to be accepted.

The best-fitting configuration is then used as the initial condition for a fit to the original data with the PS included. In this fit we used "aperture-focus" from GALIGHT, which increases the weight of the initial condition.

In Figures 4.5, 4.6 and 4.7 we show the final decomposition for a selection of galaxies with a range of morphologies. Our iterative batch fitting procedure using GALIGHT does a generally excellent job recovering reasonable fit parameters, even for complex multi-component AGN host galaxies with asymmetric features such as spiral arms.

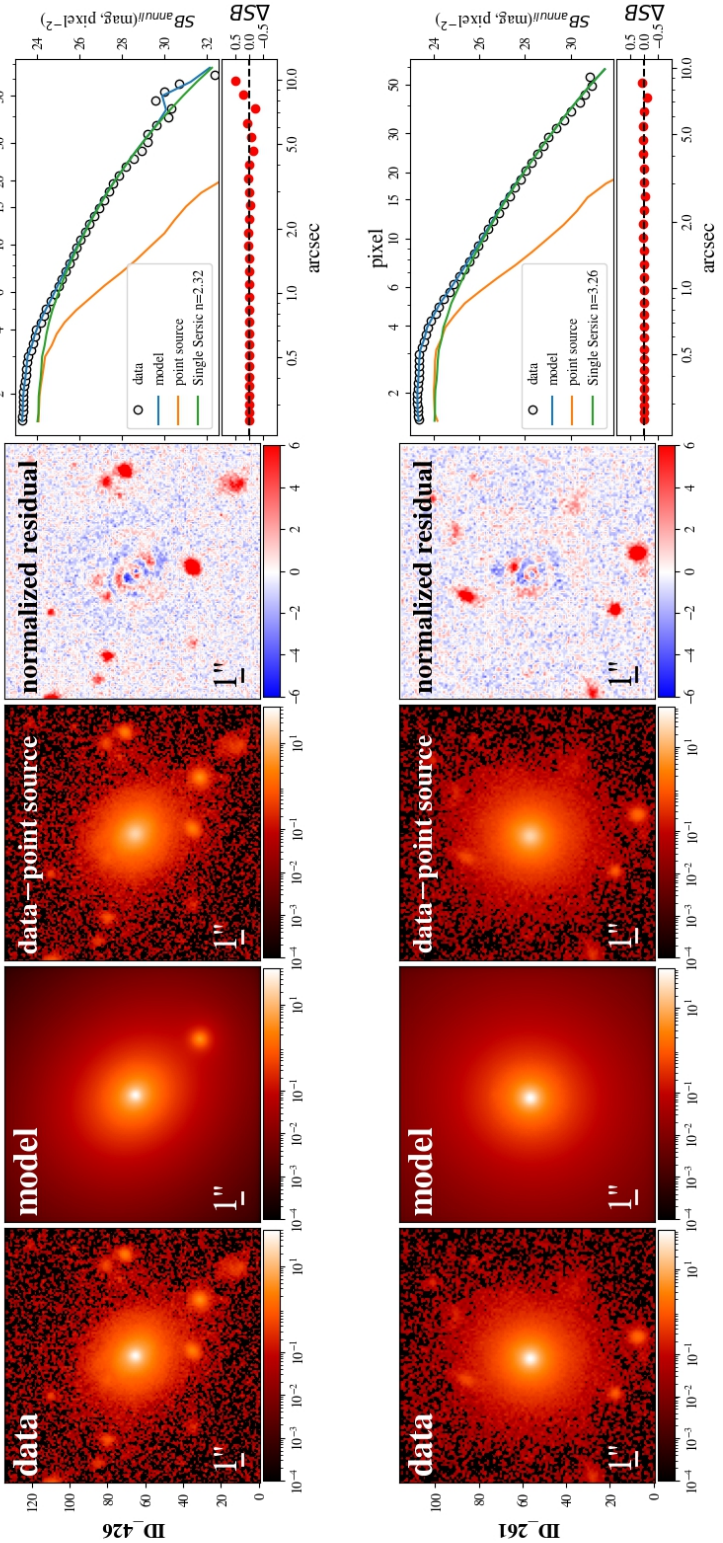

Figure 4.5: Example quasar-host galaxy decomposition for hosts with 1,2 and 3 galaxy components. The plots for each fit from left to right are the original data, the model, the PS-removed galaxy, the host galaxy with components removed, the normalised residuals and, in the rightmost panel of each, the 1D surface brightness profiles (top) and corresponding 1D residual (bottom). The fits from top to bottom are a single-component elliptical galaxy, single-component disc galaxy, 2-component bulge-dominated galaxy, 2-component disc-dominated galaxy and a 3-component barred galaxy.

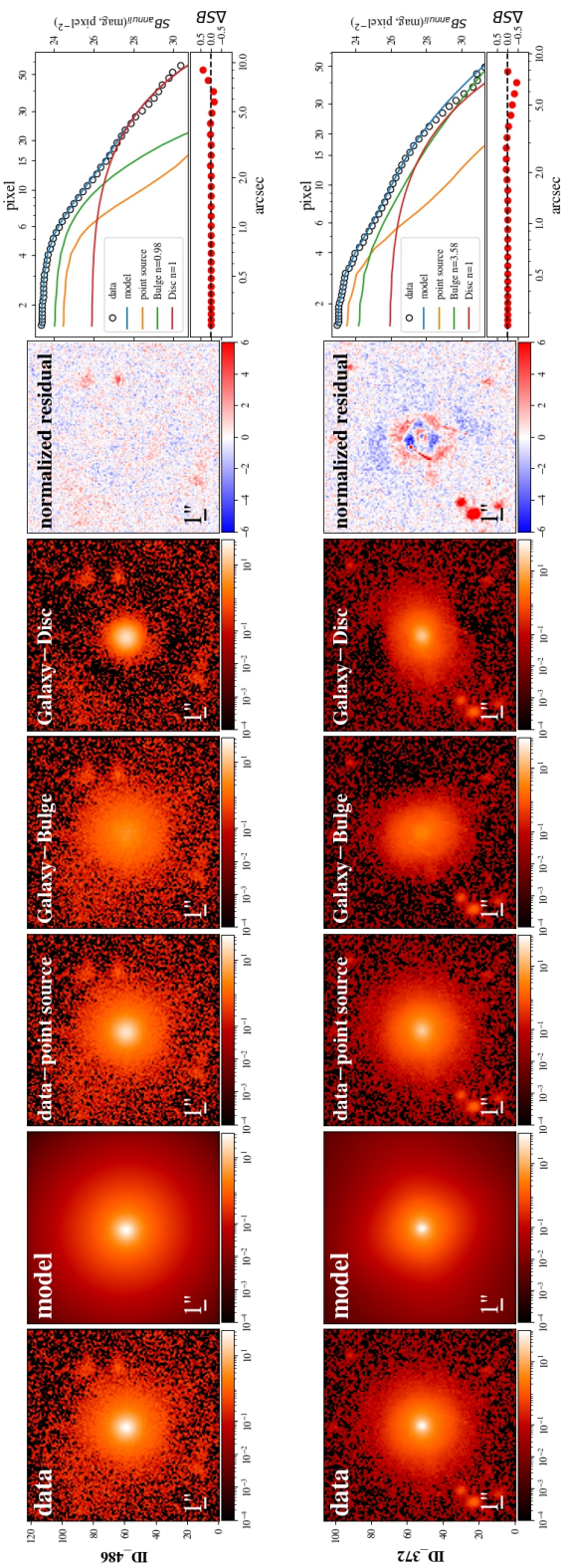

Figure 4.6: Example quasar-host galaxy decomposition for hosts with 1,2 and 3 galaxy components. The plots for each fit from left to right are the original data, the model, the PS-removed galaxy, the host galaxy with components removed, the normalised residuals and, in the rightmost panel of each, the 1D surface brightness profiles (top) and corresponding 1D residual (bottom). The fits from top to bottom are a single-component elliptical galaxy, single-component disc galaxy, 2-component bulge-dominated galaxy, 2-component disc-dominated galaxy and a 3-component barred galaxy.

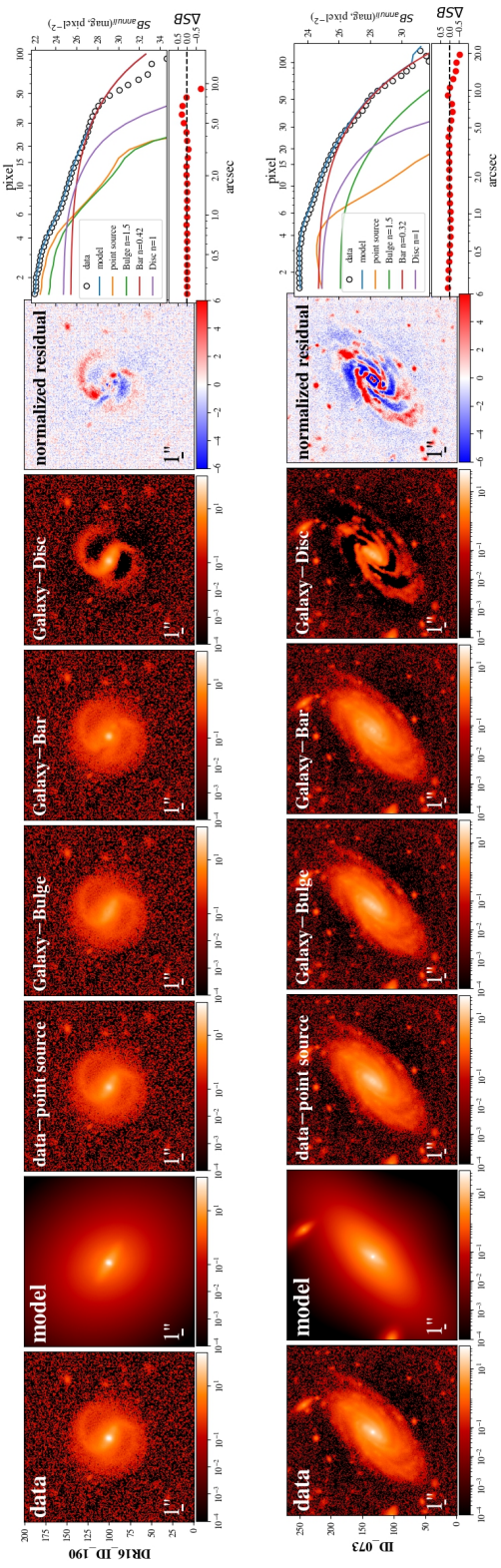

Figure 4.7: Example quasar-host galaxy decomposition for hosts with 1,2 and 3 galaxy components. The plots for each fit from left to right are the original data, the model, the PS-removed galaxy, the host galaxy with components removed, the normalised residuals and, in the rightmost panel of each, the 1D surface brightness profiles (top) and corresponding 1D residual (bottom). The fits from top to bottom are a single-component elliptical galaxy, single-component disc galaxy, 2-component bulge-dominated galaxy, 2-component disc-dominated galaxy and a 3-component barred galaxy.

4.3.2 Stellar mass estimation

We derive the stellar masses of the host galaxies from the SED fitting of the AGN removed photometry of the *grizy* bands. We perform the 2D decomposition of the galaxies in the g, r, z, and y wavebands using the same method as the i-band. However, for the purposes of stellar mass estimation we only use a single Sérsic + PSF and we fix the structural parameters to the i-band results. We then use these quasar removed host fluxes to estimate the stellar mass using the SED fitting code CIGALE (Boquien, 2020; Yang et al., 2020) and use the same parameter configuration as ZH23. We apply flux measurement errors of 10% to the sample, for two reasons: (a) the estimations derived from the MCMC sampling are likely an underestimation, and (b) to account for absolute flux calibration uncertainty and other potential unknown factors.

We assume a single stellar population model by Bruzual & Charlot (2003) with a Chabrier (2003) initial mass function and a parametric "delayed" star formation history. However, we convert the Chabrier (2003) initial mass function, assumed by CIGALE, to that of Kroupa (2001) by scaling the stellar masses by a factor of 1.08 (Madau & Dickinson, 2014), in line with ZH23. We use a dust attenuation law (`dustatt_modified_starburst`) (Calzetti et al., 2000). The models and fitting parameters used in CIGALE are given in Table 4.1. We adopt these simple parametric star formation histories because they have been shown to yield reliable stellar mass estimates, with systematic biases of $\lesssim 10\%$ and scatter of $< 20\%$, for local AGN host galaxies limited to *grizy* bands (Mitchell et al., 2013; Ciesla et al., 2015). An example of a model SED fit to the five band AGN removed flux is shown in Figure 4.8. To ensure that our mass estimates are reliable, we exclude fits where

$$\left| \log \frac{M_*^{\rm bayes}}{M_*^{\rm best}} \right| > 0.3 \ \wedge \ \chi^2_\nu > 1 \tag{4.3}$$

where $M_*^{\rm best}$ is the best-fitting stellar mass estimate and $M_*^{\rm bayes}$ is the Bayesian estimate derived from the mean of the posterior distribution. The stellar mass and its error used in this work is $M_*^{\rm bayes}$. This excludes 20 sources from our sample, giving a final sample of 415.

The total stellar masses of the sample spans the range from $9.6 < \log(M_*/\mathrm{M}_\odot) < 11.6$, with a mean galaxy stellar mass of $6 \times 10^{10}\,\mathrm{M}_\odot$. We find a slight offset between our stellar mass measurement and the ones by ZH23, with our measurement being 0.1 dex lower. However, we note that adopting stellar mass estimates from ZH23 does not change our qualitative results, and this also holds for any combination of our BH or stellar mass measurement.

Table 4.1: SED Fitting Models and Parameters

Parameter	**Input**
e-folding time of the main stellar population: t_{main} (Myr)	1, 50, 100, 250, 500, 750, 1000, 1250, 1500, 2000, 2500, 3000, 3500, 4000, 4500, 5000, 6000, 7000, 8000, 9000, 10000, 12000, 15000, 20000
Age of the main stellar population: t_{main} (Myr)	9.0, 9.5, 10.0, 10.5, 11.0, 11.5, 12.0, 12.5, 13.0
Mass fraction of the latest burst population: f_{burst}	0
Single stellar population	Bruzual & Charlot (2003)
Initial mass function	Chabrier (2003)
Ionization parameter $\log U$	-2.0
Dust attenuation	Modified starburst attenuation law
The colour excess of the nebular lines: $E(B-V)$ (mag)	0.0, 0.001, 0.005, 0.01, 0.03, 0.05, 0.1, 0.2, 0.3, 0.4, 0.5, 0.6, 0.8
Ratio of $E(B-V)$ between stellar continuum and emission line:	0.44

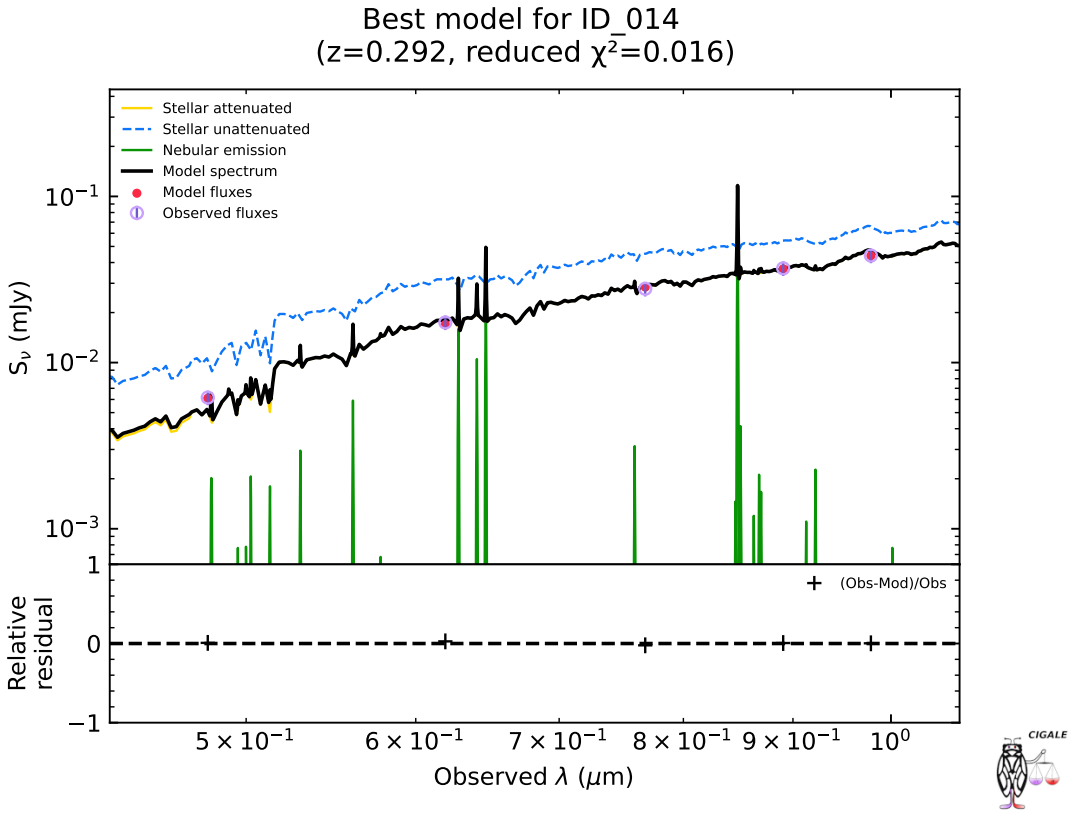

Figure 4.8: Example SED of a galaxy with the quasar component removed through image decomposition. The bottom panel show the normalised residuals between the model and the photometric data.

4.4 Synthetic AGN from Real Galaxies

As we highlighted in Section 4.1, accurate B/T measurements are a pivotal part of analysing the $M_{\rm BH}$ – $M_{\rm bulge}$ relation. The presence of a bright point source has been shown to interfere with the decomposition of galaxy properties (Simmons & Urry, 2008; Kim et al., 2008) and thus requires careful consideration. Furthermore, the different morphological parameters and resolutions of galaxies may result in different levels of reliability in their decomposition. Therefore, to accurately analyse the reliability of our decompositions, we construct a matched sample of 15 inactive galaxies for each unbarred AGN host galaxy in our sample. We limit this matched error analysis to the unbarred galaxies in our sample, as including additional metrics such as the bar-to-total ratio significantly increases the number of inactive galaxies required to create a statistically significant matched sample. For the barred galaxies, we use the results of the unbarred error analysis to assign errors to the B/T ratio. We note that excluding barred galaxies from our analysis does not qualitatively change the results of this study.

We draw the initial sample of inactive HSC galaxies from the Ghosh et al. (2023) catalogue, which also contains measurements of R_{eff}, z, and g, r, i, z, y-band flux measurements, which are used to derive stellar masses using the same method as the AGN sample in Section 4.3.2. To ensure that the inactive sample does not include AGN, we also match our control galaxies with the latest Million Quasars (Milliquas) catalogue v8 (Flesch, 2023), which includes Type-1 and Type-2 AGN. We do an initial selection of the HSC galaxies using $g-i$ colour, redshift, effective radius, and stellar mass to create an initial sample of non-AGN-host galaxies to remove galaxies that fall outside the AGN sample parameter space. We then run these galaxies through the same decomposition and visual classification process as the AGN host galaxies, as outlined in section 4.3.1.

For each AGN host galaxy, we select similar inactive galaxies based on nine criteria. The criteria and the difference tolerances for selection are M_* : 0.5 dex, z: 0.15, $g-i$ colour: 0.3, $R_{eff,Bulge}$: 0.3 dex, n_{Bulge}: 1 dex, single Sérsic axis ratio: 0.2, B/T ratio: 0.3 dex, Pseudo/Classical bulge classification (if present): True/False, and bar: True/False. The inactive galaxies can be assigned to multiple AGN host galaxies, but each AGN host is limited to 15 comparison galaxies.

If more than 15 galaxies fulfil these requirements, we select the best matches based on the sum of the differences to the selection criteria. As some parameters have larger tolerances, we apply different weights so as not to be dominated by a single parameter. The weights are as followed: M_* : 0.15, z: 1, $g-i$ colour: 1, $R_{eff,Bulge}$: 1.3, n_{Bulge}: 0.3, single Sérsic axis ratio: 2, B/T ratio: 1.

The matched inactive galaxies are then converted into synthetic active galaxies by inserting a scaled PSF at the central pixel location, determined from the coordinates in the HSCSSP survey catalogue (Aihara et al., 2018a, 2022). The flux density of the point source is scaled relative to the bulge flux (or the total flux for elliptical galaxies) such that it reproduces the point source to bulge flux ratio measured for the AGN host galaxy to which it is matched. The synthetic active galaxies are then passed through the decomposition processes as outlined in section 4.3.1. We note that a different PSF model is used for inserting a point source and for modelling it during decomposition. In Figure 4.9, we show three inactive galaxies before and after adding a point source. The PSF is scaled so that $F_{ps} = 0.1F_{Bulge}$ in the middle and on the right, it is scaled so that $F_{ps} = F_{Bulge}$.

4.5 Results

This study produced a number of results, and thus this section is organised into multiple subsections. We begin below with a discussion of the parameter recovery assessments described above. Having established the boundaries of reliability and uncertainty in our fitting procedure and datasets, we then present and discuss results on the host galaxy properties and their correlation with black hole properties.

4.5.1 Reliability and Uncertainties in Host Galaxy Fitting

4.5.1.1 Recovery: Point Source and Galaxy Magnitudes

In Figure 4.10 we show the recovery differences (Δ = Output - Input) of the single Sérsic magnitude (m_{Single}), AGN magnitude from single Sérsic fit ($m_{AGN,Single}$) and bulge-disc fit ($m_{AGN,BD}$), the point source-host ratio (L_{PS}/L_{Host}) and point

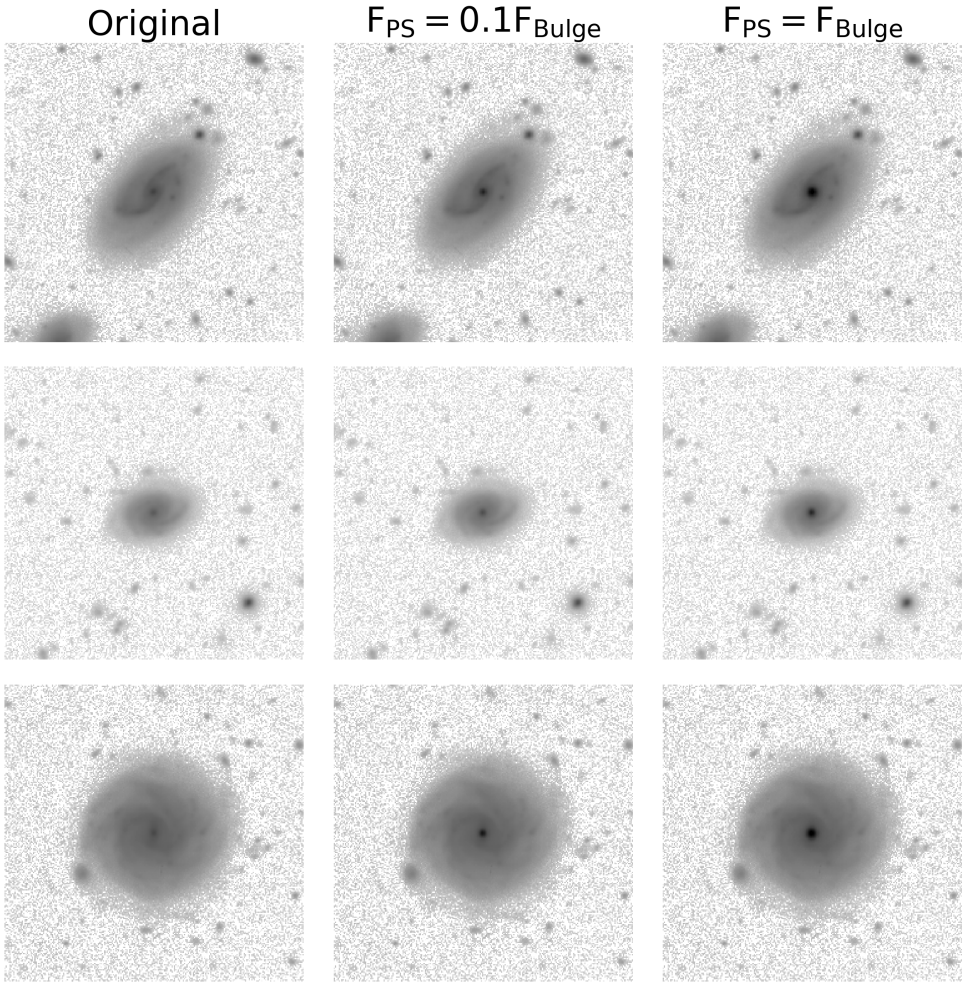

Figure 4.9: HSC i-band images of three inactive galaxies are shown before and after adding a central point source. In the middle column, the PSF is scaled so that $F_{ps} = 0.1F_{Bulge}$ and on the right, it is scaled so that $F_{ps} = F_{Bulge}$. HSC i-band images of three inactive galaxies are shown before and after adding a central point source. In the middle column, the PSF is scaled so that $F_{ps} = 0.1F_{Bulge}$ and on the right, it is scaled so that $F_{ps} = F_{Bulge}$. The point sources simulate AGN emission, allowing assessment of the presence of a bright point source that impacts the decomposition of galaxy structure in this study.

source-bulge ratio (L_{PS}/L_{Bulge}) versus the input values of L_{PS}/L_{Host}, L_{PS}/L_{Bulge}, m_{Single} and m_{AGN} respectively. For m_{Single} we find a constant systematic bias towards slightly overestimating m_{Single} ($\Delta m_{Single} \approx 0.06$ mag; $1\sigma \approx 0.19$ mag). The worst performing parameter is $m_{AGN,Single}$ ($\Delta m_{AGN} \approx -0.15$ mag; $1\sigma \approx 0.80$ mag), which is systematically underestimated and increases as the flux ratio becomes more dominated by the galaxy. There is a slight improvement for $m_{AGN,BD}$ ($\Delta m_{AGN} \approx -0.07$ mag; $1\sigma \approx 0.75$ mag). Overall, the AGN parameter recovery is very good with little or no systematic offset. The differences Δ increase at the extreme ends of most distributions, in ways that we expect (*e.g.,* poorly recovering point-source magnitudes for very faint point sources in bright host galaxies, seen at the lowest values of L_{PS}/L_{Host}). The small average systematic shift in Sérsic magnitude for the single-Sérsic fit does not increase even when the point source is much brighter than the host galaxy.

4.5.1.2 Recovery: Host Parameters

In Figure 4.11 we show the differences between the single Sérsic effective radius ($R_{eff,Single}$), single Sérsic index (n_{Single}), and Sérsic effective radius of the disc ($R_{eff,Disc}$) versus the input value of L_{PS}/L_{Host}, the input value of L_{PS}/L_{Bulge}, and the input and output values for the same parameter, respectively. We find that size measurements are reliable with no systematic offset ($\Delta \log R_{eff,Single} \approx 0.00$ dex; $1\sigma \approx 0.09$ dex and $\Delta \log R_{eff,Disc} \approx -0.03$ dex; $1\sigma \approx 0.10$ dex) or significant dependence on the properties of the galaxy or relative AGN brightness. For n_{Single}, we find that there is a small systematic bias toward lower values ($\Delta \log n_{Single} \approx -0.09$ dex; $1\sigma \approx 0.02$ dex) that increases as a function of L_{PS}/L_{Host}. Overall, the host parameter recovery is good with little or no systematic offset.

4.5.1.3 Recovery: Bulge

In Figure 4.12 we show the differences between B/T, M_{Bulge}, bulge effective radius ($R_{eff,Bulge}$) and bulge Sérsic index (n_{Bulge}) versus the input value of L_{PS}/L_{Host}, the input value of L_{PS}/L_{Bulge}, and the input and output values for

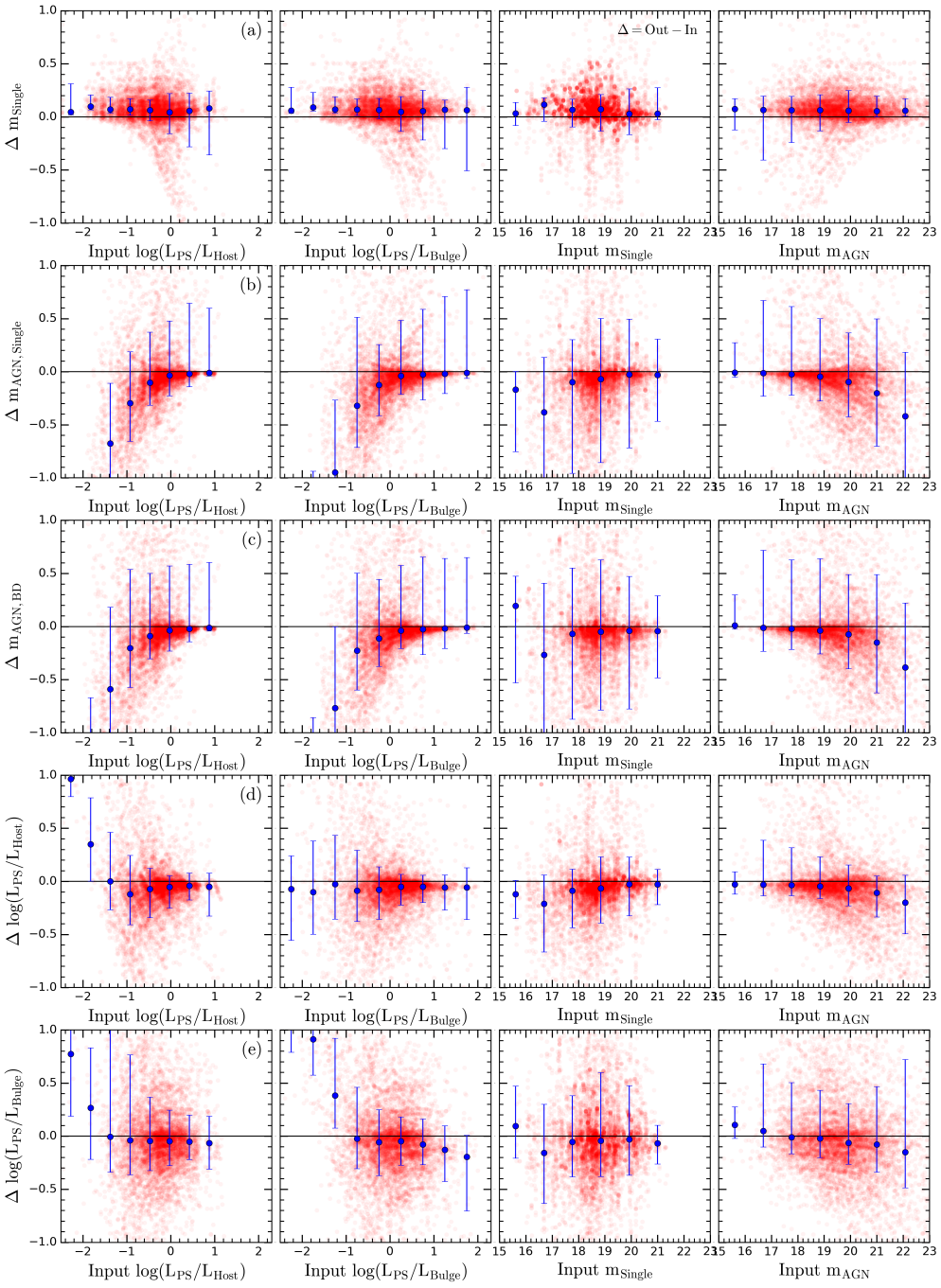

Figure 4.10: The Difference (Δ = Output - Input) between the measured parameters of the synthetic AGN host galaxies and their initial values, which are based on the properties of the inactive galaxies used to generate the synthetic AGN host galaxies. The error bar shows a 1σ distribution. Rows (a-e) show the difference between m_{Single}, $m_{AGN,Single}$, $m_{AGN,BD}$, L_{PS}/L_{Host} and L_{PS}/L_{Bulge} as a function of their input values. The recovered parameters are reliable with little or no systematic offset.

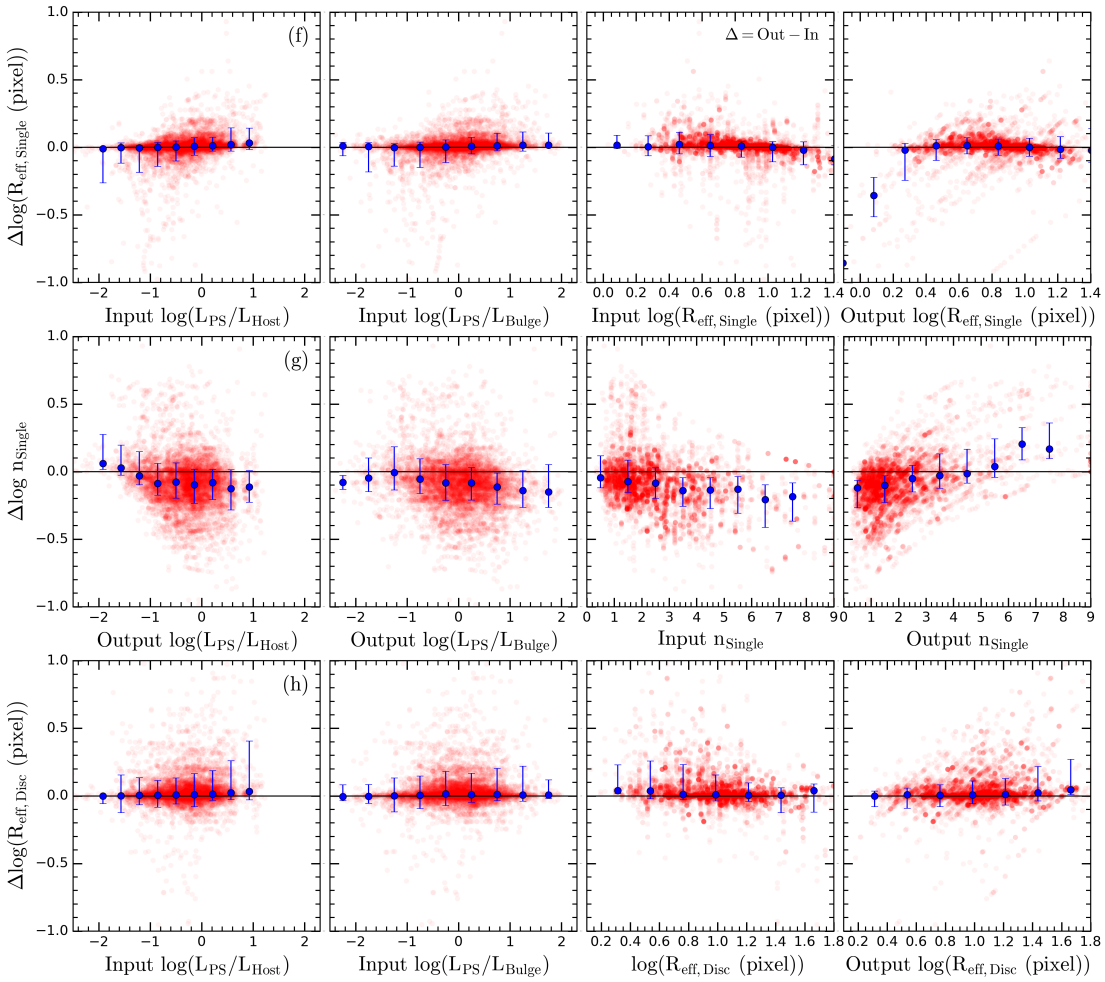

Figure 4.11: Same as Figure 4.10, with Rows (f-h) showing the difference between $R_{eff,Single}$, n_{Single} and $R_{eff,Disc}$ as a function of input L_{PS}/L_{Host}, input L_{PS}/L_{Bulge}, the input value of the parameter and the output value. The recovered parameters are reliable with little or no systematic offset.

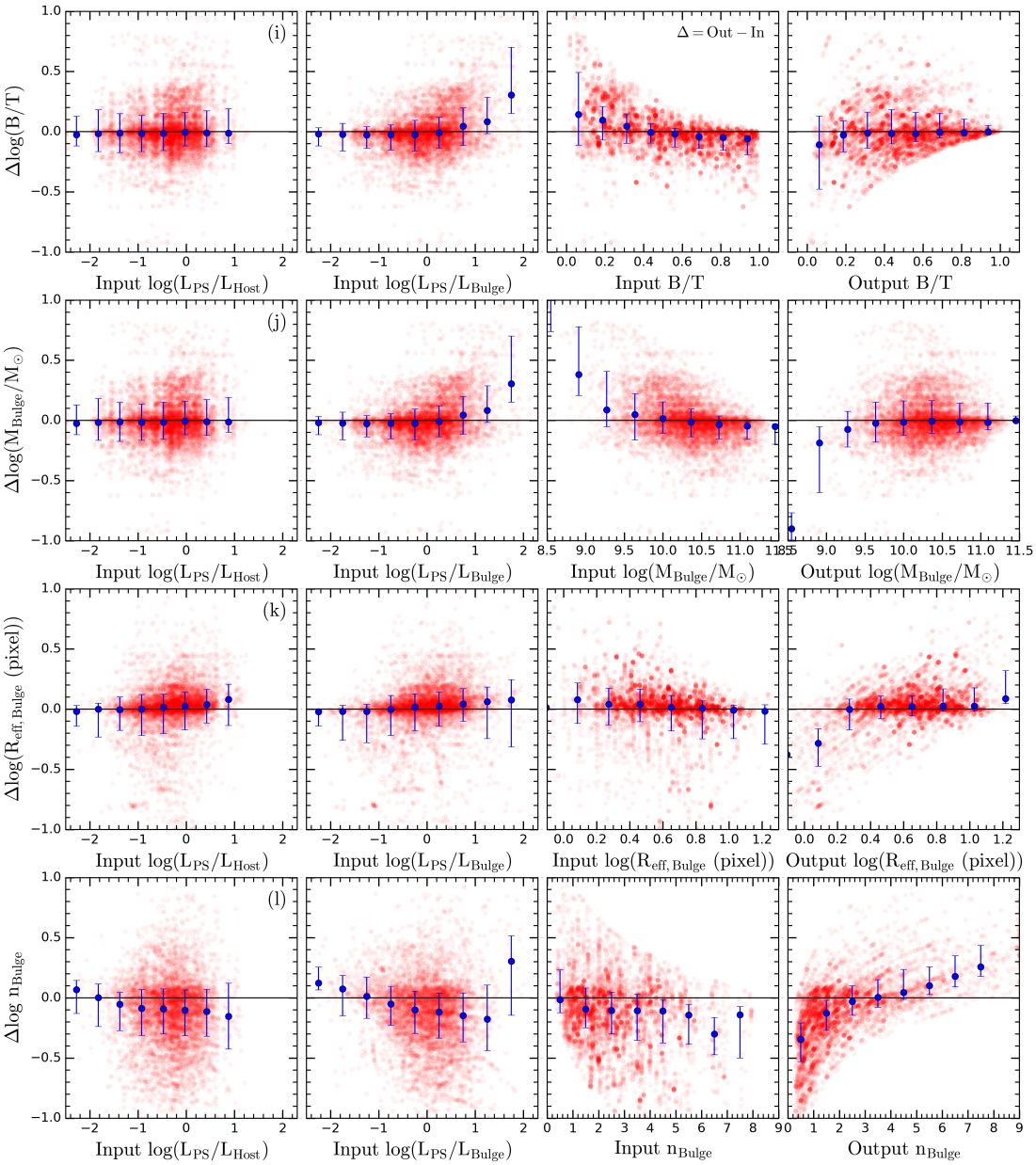

Figure 4.12: Same as Figure 4.10, with Rows (i-l) showing the difference between B/T, M_{Bulge}, $R_{eff,Bulge}$, n_{Bulge} as a function of input L_{PS}/L_{Host}, input L_{PS}/L_{Bulge}, the input value of the parameter and the output value. The recovered parameters are reliable with little or no systematic offset.

the same parameter, respectively. On average we find that the following parameters are well recovered with no systematic bias: B/T ($\Delta \log B/T \approx 0.01$ dex; $1\sigma \approx 0.2$ dex), M_{Bulge} ($\Delta \log M_{Bulge} \approx -0.01$ dex; $1\sigma \approx 0.2$ dex) and $R_{eff,Bulge}$ ($\Delta \log R_{eff,Bulge} \approx 0.02$ dex; $1\sigma \approx 0.2$ dex). There is little dependence on the properties of the galaxy or L_{PS}/L_{Host}. However, the offset and scatter increases significantly where $\log(L_{PS}/L_{Bulge}) > 1$. For B/T, there is increased offset and scatter at $B/T < 0.33$. This is expected as a small change in a flux measurement at low values of B/T has a large impact. Since B/T is directly used in determining M_{Bulge}, the offset and scatter in the recovered masses of low-mass bulges are larger than high-mass bulges. For n_{Bulge}, we find that there is a systematic bias toward lower values ($\Delta \log n_{Bulge} \approx -0.10$ dex; $1\sigma \approx 0.28$ dex) that increases as a function of L_{PS}/L_{Bulge}. Overall, the bulge parameter recovery is good with little or no systematic offset.

Having measured the dependence of recovered fit parameters on multiple variables in the data, we derive a set of parameter corrections to each AGN host galaxy based on these results. We apply these bespoke corrections to every AGN host galaxy fit to derive the final value and uncertainty of each parameter. The corrections to parameter values are generally very small compared to the additional uncertainty term added by the correction.

4.5.1.4 Recovery: Classical Bulges Versus Pseudo-Bulge

Galaxy bulges are typically split into two classifications: classical bulges, which are dispersion-dominated, and pseudo-bulges, which are rotation-dominated. Classical bulges are analogous to elliptical galaxies, with their growth likely driven by violent processes such as mergers (Kormendy & Kennicutt, 2004; Kormendy & Ho, 2013). Pseudo bulges, conversely, are believed to be formed through calmer secular evolution such as disc instabilities (Kormendy & Kennicutt, 2004; Combes, 2020; Sachdeva et al., 2020). These formation mechanisms are also heavily invoked for AGN fuelling. Thus the relation between bulge mass, bulge classification, and SMBH mass can provide an important insight into SMBH growth.

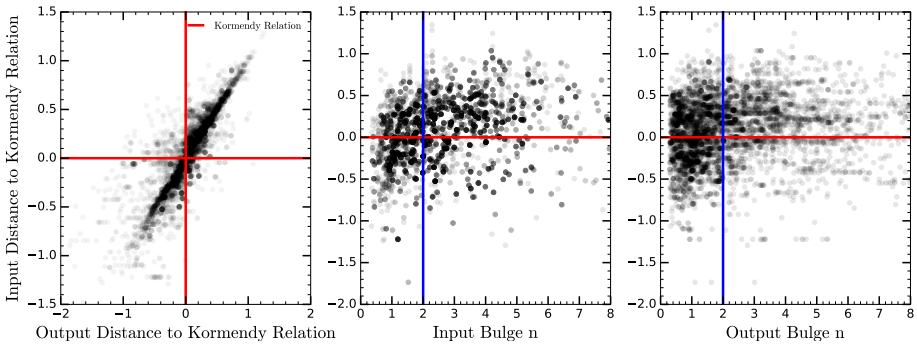

Figure 4.13: Left: The input against output distance from the Kormendy relation. **Middle and Right:** The input distance from the Kormendy relation against the Bulge Sérsic index (Input in the middle and output the right plot). Bulge classification is reliably recovered using the Kormendy relation, while the bulge Sérsic approximation becomes less reliable with the addition of a point source. Even so, only a small fraction of galaxies change their bulge classification with the addition of a point source.

As classical bulges have similar properties to ellipticals, they also follow the fundamental plane, which is a relation between size, mass and mean surface brightness followed by elliptical galaxies (Dressler, 1987; Djorgovski & Davis, 1987). The Kormendy relation (Kormendy, 1977; Hamabe & Kormendy, 1987) is a projection of the fundamental plane into mean surface brightness versus effective radius and is used to classify bulge type, with objects 1σ below the relation designated as pseudo-bulges. In this work, we use the Kormendy relation from Gadotti (2009), which is derived from galaxies at a similar redshift and magnitude as ours. The threshold for pseudo-bulge classification is given by:

$$\langle \mu_e \rangle > 13.95 + 1.74 \times \log(R_{eff}), \tag{4.4}$$

where $\langle \mu_e \rangle$ is the mean surface brightness within the effective radius, and R_{eff} is the effective radius in parsecs.

Figure 4.13 shows the distance from the Kormendy relation. In the left panel we plot the initial against recovered distance to the Kormendy relation. This distance is defined as the perpendicular offset of each point from the pseudo-bulge classification threshold in the Kormendy plane. The lines mark the Kormendy

bulge classification thresholds. Points in the lower left and upper right quadrants correspond to no change in bulge classification. We find that only a small fraction (9%) of galaxies change bulge classification with the addition of a point source. As the classification of bulges is a binary, the majority of misclassifications occur at galaxies around the threshold. Of galaxies more than 0.15 in perpendicular distance from the classification threshold in the μ_e versus $\log(R_{eff})$ plane, only 3.5% change bulge classification. Of bulges with a L_{PS}/L_{Host} ratio of 0 only 12% change classification. Thus bulge classification is highly reliable even in the presence of a bright point source.

Bulge Sérsic index is widely used to approximate bulge classification with $n > 2$ being classical and $n < 2$ pseudo (Gadotti, 2009). To quantify the reliability of this approximation, in the middle and right plots of Figure 4.13 we show the relation between bulge Sérsic index and distance from the Kormendy relation. The relative position of a component to the KR (marked by the horizontal red line) is used as the bulge type classifier, with above and below corresponding to classical and pseudo-bulges respectively. For the inactive galaxies (middle plot) we also find a Sérsic index of $n = 2$ to be the best division for classifying for bulges: 69% with $n > 2$ were classified as classical and 55% with $n < 2$ were classified as pseudo. However, due to the systematic underestimation and increased scatter in bulge Sérsic index, this method of bulge classification becomes less reliable for galaxies with a point source component. 53 percent of classical bulges are misclassified as pseudo-bulges, and 30 percent of pseudo-bulges are misclassified as classical bulges.

4.5.2 Host Galaxy Properties

For every galaxy in our sample, the 2D model fitting improves with the inclusion of a point source in the model. For 279 galaxies the fitting further improves with the inclusion of a second Sérsic profile. For 96 galaxies the inclusion of a bar Sérsic model significantly improves the fitting. Finally, 39 galaxies are best fit with a single Sérsic; based on the BIC and visual inspection, 10 are disc-dominated galaxies where a bulge cannot be reliably fit. Based on the i-band B/T, we divide the sample into three categories: disc-dominated, where $B/T < 0.33$ (162

galaxies); intermediate, where $0.33 < B/T < 0.66$ (110 galaxies); and bulge-dominated, where $B/T > 0.66$ (142 galaxies). The i-band B/T is also used to derive M_{Bulge}, which we find ranges from $8.7 < \log(M_{Bulge}/\mathrm{M}_{\odot}) < 11.3$, with a mean bulge stellar mass of $3 \times 10^{10}\,\mathrm{M}_{\odot}$.

We further classify the bulge components as classical and pseudo-bulges using Equation 4.4. We classify 302 bulges as classical and 106 as pseudo-bulges. The mean B/T of pseudo-bulges is 0.25 , while for classical bulges it is 0.5. For each galaxy, we also performe a visual analysis of the original HSC images to assign morphologies into three categories: 'disc-dominated', 'unsure' and 'bulge-dominated'. Galaxies could be classed as both 'X-dominated' and 'unsure'. We find a good match rate between the visual classifications and those based on the decompositions as shown by Table 4.2.

The wide coverage of the galaxy and BH parameter space makes this sample well suited to study the morphological importance in galaxy scaling relations.

Table 4.2: Confusion Matrix between Decomposed and Visually Classified Morphologies

	Visually Classed Dominant Component		
Decomposed Type	**Disc (%)**	**Unsure (%)**	**Bulge (%)**
Disc-dominated	71	33	8
Intermediate	18	47	43
Bulge-dominated	8	29	79

4.5.3 Black Hole - Stellar Mass Relations

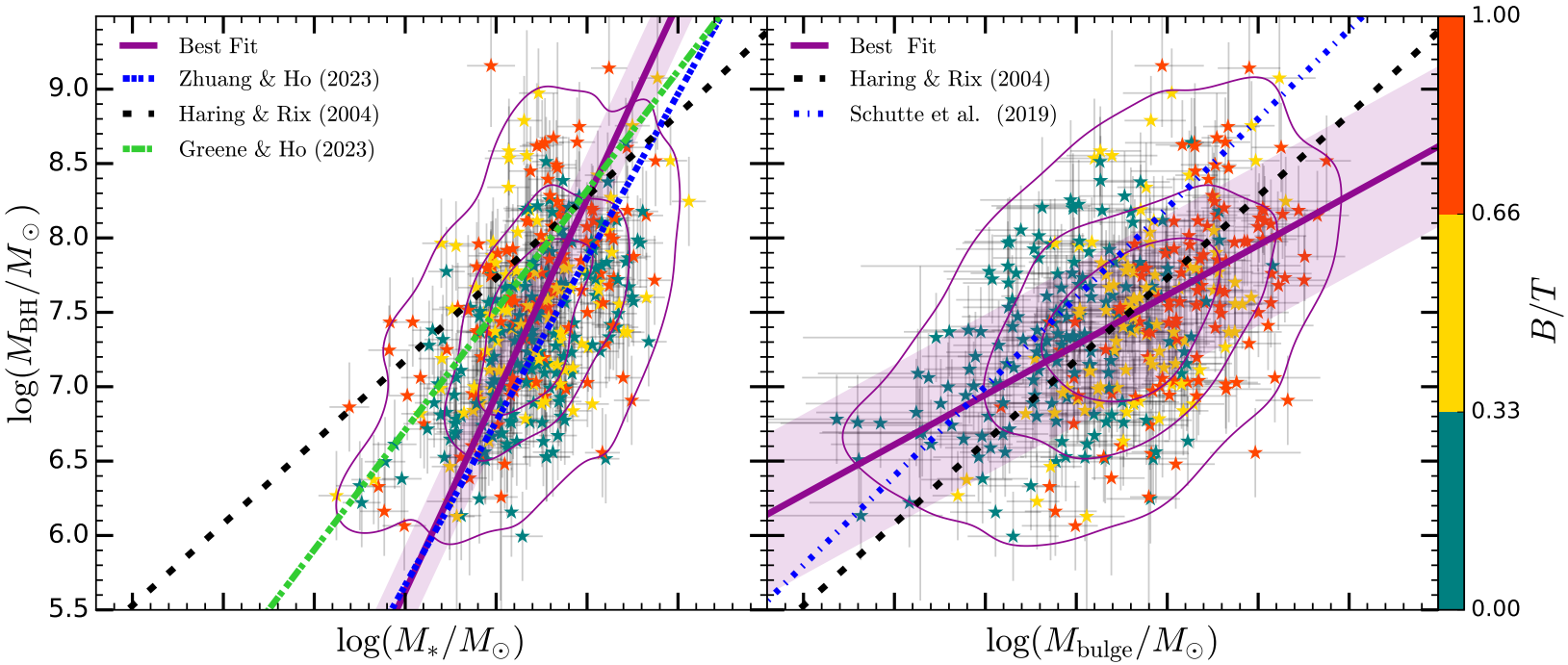

Figure 4.14: Left: Black hole - total stellar mass relation. The best-fit line is shown in purple with a 3σ error shaded region. The black dashed line represents the Häring & Rix (2004) relation for dynamically measured elliptical galaxies, and the lime green 1-2-1 dashed line represents the Greene et al. (2020) relation, dynamically derived from early and late-type galaxies. The blue 1-1-1 dashed line is the relation from Zhuang & Ho (2023) for AGN host galaxies at $z < 0.35$. **Right:** Black hole - bulge stellar mass relation. The blue dot-dashed line is the dynamical bulge relation including dwarf galaxies from Schutte et al. (2019). The Black hole - total stellar mass relation is steeper.

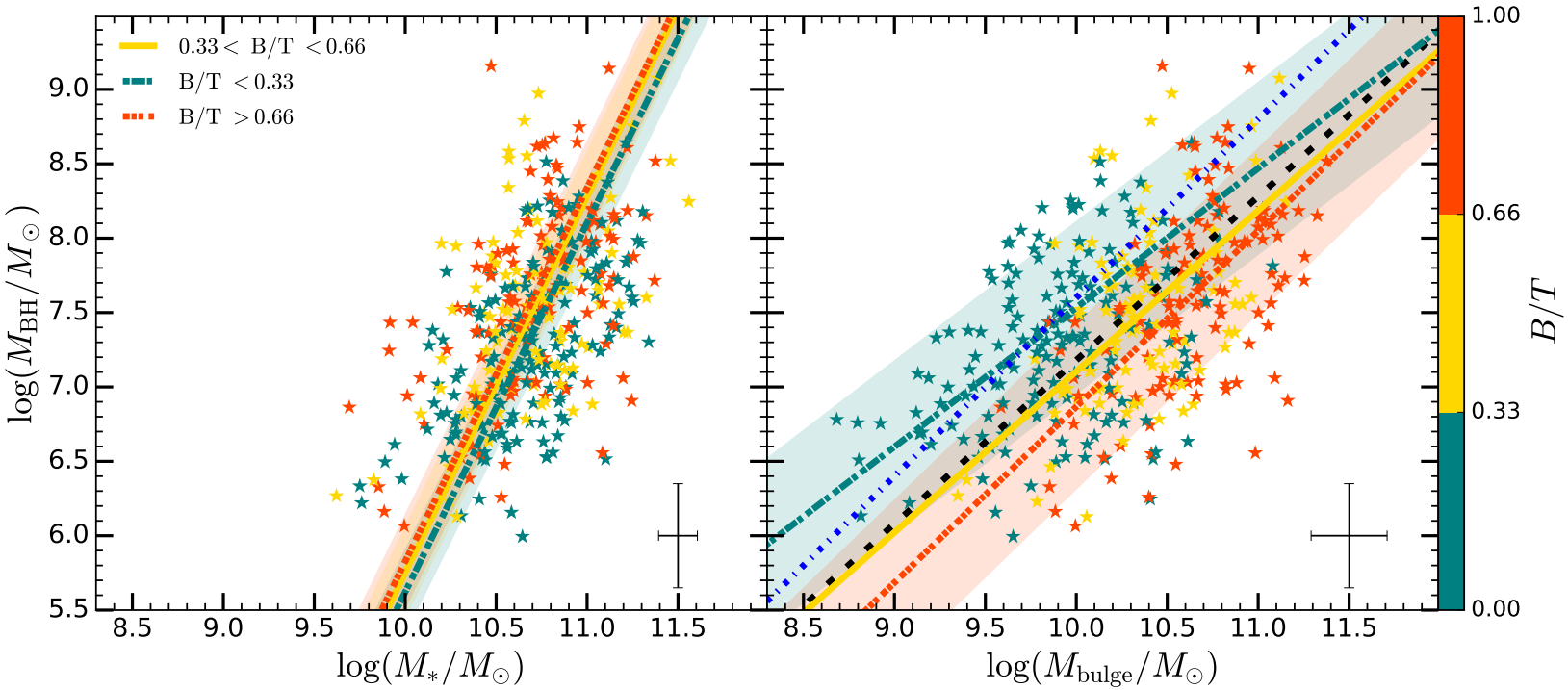

Figure 4.15: Same as Figure 4.14 but separated into the three morphological classifications and error bars removed for clarity. B/T is not a strong determinant of where a galaxy will lie on the Black hole - total stellar mass diagram, while it is on the Black hole - bulge stellar mass diagram, with disc-dominated galaxies offset above bulge-dominated galaxies.

We first present the $M_{\rm BH}$ – M_* relation in the left plot of Figure 4.14. We fit data using the linear regression fitting code `LINMIX_ERR` (Kelly, 2007). The solid purple line represents the best-fit relation and is described by:

$$\log\left(\frac{M_{BH}}{\rm M_\odot}\right) = (2.46 \pm 0.04)\log\left(\frac{M_*}{10^{11}\ \rm M_\odot}\right) + (8.24 \pm 0.30) \tag{4.5}$$

with a scatter of 0.3 dex, shown by the purple-shaded region. We find a positive correlation with the Spearman and Pearson correlation coefficients being $r_S = 0.52$ and $r_p = 0.50$, respectively, all with p-values $<< 0.01$. As a comparison, we include a number of relations taken from the literature. Plotted as a solid green line is the relation from Greene et al. (2020), which is derived from dynamical measurements of local ($z < 0.005$) SMBHs and includes both late and early-type galaxies. We also include the relation from Häring & Rix (2004), which is derived from dynamical measurements of local elliptical galaxies and is plotted as a dashed black line. The solid black line comes from Zhuang & Ho (2023) and is derived from an analysis of SDSS Type 1 AGN using Pan-STARRS. Our relation is in good agreement with the relation from Zhuang & Ho (2023). This is expected, as there is significant overlap between the samples; however, all values are measured independently. In comparison to Greene et al. (2020), we find a steeper relation, which differs by only 0.25 dex at $M_* = 10.5\ \rm M_\odot$, less than the typical error associated with single-epoch BH mass measurements. The difference is mainly driven by the inactive early-type galaxies hosting significantly larger SMBH than the active bulge-dominated galaxies in our sample. Previous studies have also highlighted the fact AGN are seemingly under-massive when compared to inactive galaxies (Reines & Volonteri, 2015; Shankar et al., 2016; Ho & Kim, 2014; Sturm & Reines, 2024). However, a conclusive reason for this is still elusive.

In the top right of Figure 4.14, we present our $M_{\rm BH}$ – $M_{\rm bulge}$ relation. To account for the uncertainty in the fitting of the bulge components, we incorporate the derived uncertainty in B/T for each galaxy from the matched error analyses (see Section 4.5.1.3) is incorporated into their bulge mass error. We then use `LINMIX_ERR` to fit a relation for galaxies with detected bulge components. The

best-fit relation is described as follows:

$$\log\left(\frac{M_{BH}}{\mathrm{M}_{\odot}}\right) = (0.67 \pm 0.07)\log\left(\frac{M_{Bulge}}{10^{11}\ \mathrm{M}_{\odot}}\right) + (7.95 \pm 0.76) \tag{4.6}$$

with a scatter of 0.55 dex, shown by the purple-shaded region. We also find a positive correlation in this relation, with the Spearman and Pearson correlation coefficients being $\rho_S = 0.45$ and $\rho_p = 0.43$, respectively. The p-values are all $<< 0.01$. As a comparison, we include two relations taken from the literature. Plotted as a blue dash-dot line is the relation from Schutte et al. (2019) and the solid black line is taken from Häring & Rix (2004), which are derived from dynamical measurements of local SMBHs hosted in classical bulges and elliptical galaxies. We find that, within their error, the AGN on the M_{BH} – M_{bulge} diagram are consistent with these dynamical relations.

When comparing the M_{BH} – M_{bulge} and M_{BH} – M_* relations we find there is greater scatter and lower correlation coefficients for the M_{BH} – M_{bulge} relation, which seems to suggest that M_{BH} – M_* is the stronger and tighter relation. This is seemingly in conflict with the merger-driven BH-galaxy co-evolution model. However, many studies have suggested that galaxies with different morphological structures follow different relations and should be treated separately (Kormendy & Ho, 2013; Reines & Volonteri, 2015; Greene et al., 2020).

To investigate whether this difference is driven by the grouping of galaxies with different morphologies, we fit separate relations to the different morphological categories, as shown in Figure 4.15. For the M_{BH} – M_* relation, we find that the disc-dominated (green), intermediate (yellow) and bulge-dominated (red) galaxies are consistent with each other. Therefore, morphology, as denoted by the B/T ratio, is not an indicator of where a galaxy falls in the M_{BH} – M_* relation. The correlation coefficients for disc-dominated, intermediate and bulge-dominated galaxies are ρ_S=0.59 & ρ_P=0.58, $\rho_S = 0.41$ & ρ_P=0.45, and $\rho_S = 0.50$ & ρ_P=0.49, respectively and the p-values are all $<< 0.01$.

As these morphological groups follow similar M_{BH} – M_* relations, it follows that they must populate different parts of the M_{BH} – M_{bulge} relation, as shown in the right plot of Figure 4.15. We find that location on the M_{BH} – M_{bulge} relation changes as a function of B/T, with SMBHs in disc-dominated galaxies being

more massive with respect to their bulges compared to bulge-dominated galaxies. The best fits for the $M_{\rm BH}$ – $M_{\rm bulge}$ relation broken down into the morphological groups are shown in Table 4.3:

Table 4.3: Black hole - bulge mass relations for different morphological types.

Morphology	**Slope**	**Intercept**	$\rho_{\mathbf{S}}$	$\rho_{\mathbf{P}}$	**Scatter (dex)**
Bulge-dominated	1.02 ± 0.21	8.15 ± 2.10	0.50	0.50	0.54
Intermediate	1.15 ± 0.18	8.03 ± 1.90	0.35	0.43	0.54
Disc-dominated	0.94 ± 0.25	11.64 ± 2.30	0.37	0.37	0.54

A similar result was also found by Fahey et al. (2025) and Simmons et al. (2017), who found that the SMBHs of the most luminous AGN in highly disc-dominated galaxies are over-massive compared to their bulges. Moreover, studies have found that broad-line AGN at high-redshift, which tend to be disc-dominated, correlate more strongly with the total stellar mass than bulge stellar mass, with their SMBHs being over-massive in comparison to the local $M_{\rm BH}$–$M_{\rm bulge}$ relation (Jahnke et al., 2009; Cisternas et al., 2011b; Schramm & Silverman, 2013; Sun et al., 2015; Li et al., 2021).

We find that at a bulge mass of $\log\left(M_{bulge}/\mathrm{M}_{\odot}\right) = 10.5$, SMBHs in the bulges of bulge-dominated galaxies is on average 0.5 dex less massive than ones in disc-dominated galaxies. When broken down into the morphological groups, we find that AGN host galaxies follow a similar slope to the local inactive relation, but with different normalisation: bulge-dominated galaxies are offset 0.25 dex lower and disc-dominated galaxies are offset 0.25 dex above the relation on average. The slightly lower correlation coefficient and slightly higher scatter could be consistent with a picture of BH averaging following a merger or that growth in disc-dominated galaxies is more stochastic in nature (Kormendy & Ho, 2013).

This seemingly suggests that for these AGN host galaxies, the process which drives BH growth is more connected to the total gravitational potential of the galaxy than the process that drives bulge growth. Under the paradigm where mergers drive both BH growth and bulge formation, we would expect disc-dominated galaxies to lie offset below the relation traced out by bulge-dominated galaxies in the $M_{\rm BH}$ – M_{*} diagram. In that same paradigm, classical bulges

of disc-dominated galaxies and the bulges of bulge-dominated galaxies should follow the same relation on the $M_{\rm BH}$ – $M_{\rm bulge}$ diagram. Therefore, our results are at odds with a co-evolution scenario only driven by mergers, or a scenario where SMBH growth is predominantly connected to bulge growth. However, we note that there is a significant error in the SMBH and bulge masses and that the relations are within 3σ of each other, so we cannot confidently rule out a bulge connection. Moreover, there is significant evidence that secular processes can drive both SMBH (Cisternas et al., 2011b,a; Bellovary et al., 2013; Villforth, 2023) and bulge growth (Bell et al., 2017; Gargiulo et al., 2017; Du et al., 2021), so a stronger $M_{\rm BH}$ – $M_{\rm bulge}$ relations would not necessarily indicate a merger-driven co-evolution.

Interestingly, our results are in good agreement with recent work by Smethurst et al. (2024), who investigated the $M_{\rm BH}$ – M_* and $M_{\rm BH}$ – $M_{\rm bulge}$ relations as functions of B/T and merger history in the Horizon-AGN hydrodynamical simulation (Dubois et al., 2014). They found that the correlation between total stellar mass and SMBH mass is stronger and tighter than that for the bulge stellar mass in the simulation. Moreover, similar to our results, they found no dependence on B/T for the $M_{\rm BH}$ – M_* relation and observed a dependence on B/T similar to ours for the $M_{\rm BH}$ – $M_{\rm bulge}$ relation.

In Figure 4.16, we plot our mass scaling relations with pseudo-bulges denoted by blue stars and classical bulges by red stars. We find that SMBHs in pseudo-bulges, as defined by the Kormendy relation, are consistent with classical bulges. This result is in line with some other works (*e.g.,* Bennert et al. 2021; Sahu et al. 2019a), which also suggest that classical and pseudo-bulges follow the same scaling relations. As pseudo-bulges are likely the result of secular dissipative processes rather than galaxy merger-driven, this result is also evidence against a merger-driven scenario which suggests that there should be no co-evolution in pseudo-bulges (Kormendy & Ho, 2013; Ho & Kim, 2014; Saglia et al., 2016).

Moreover, recent observations and simulations have suggested that classical bulges can develop through secular processes, such as violent disc instabilities and the destruction of bars (Martig et al., 2012; Bell et al., 2017; Park et al., 2019; Guo et al., 2020; Du et al., 2021). On the other hand, it is possible that mergers also play a role in the growth of pseudo-bulges (Okamoto, 2013; Sauvaget et al.,

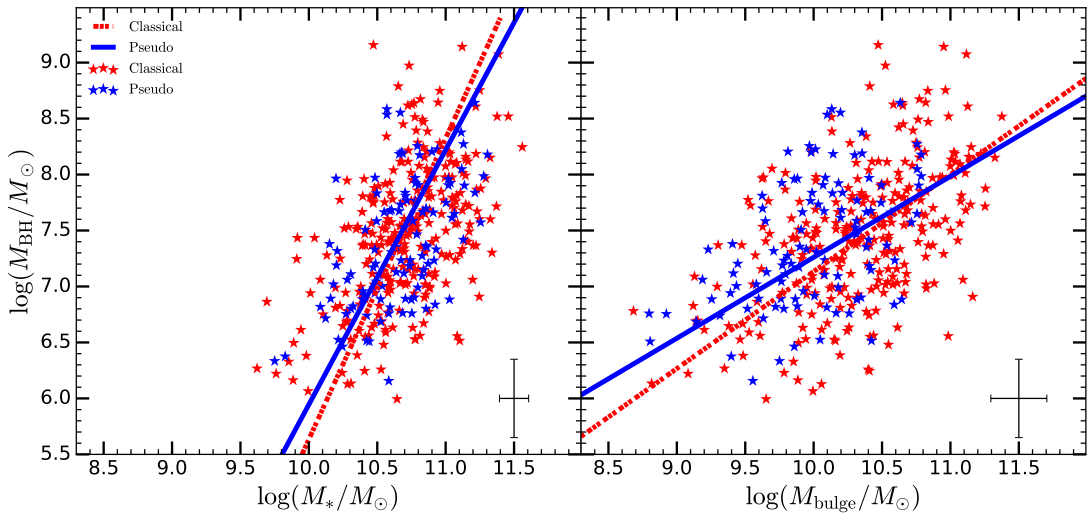

Figure 4.16: Same as Figure 4.15, but the sample is divided into galaxies hosting classical- (red dashed trend line and stars) and pseudo-bulges (blue dashed trend line and stars). Within the measurement uncertainties, the two follow consistent $M_{\rm BH}$–M_* relations, with pseudo-bulges showing a slightly higher normalisation.

2018). Furthermore, the small compact bulges of disc-dominated galaxies may be the remnants of high redshift ultra-compact spheroids, which have formed a disc component (Damjanov et al., 2009; de la Rosa et al., 2016; Costantin et al., 2023). The diversity in bulge growth mechanisms and the potential that local samples of inactive galaxies are atypical (Kormendy et al., 2010; Shankar et al., 2016) may contribute to the uncertainty of the scatter in the $M_{\rm BH}$ – $M_{\rm bulge}$ relation.

4.5.4 Mass - Size Relation of AGN Hosts

Feedback driven by accreting supermassive black holes has often been linked to the structural transformation and evolution of galaxies (e.g., Fabian, 2012; Dubois et al., 2014; Beckmann et al., 2017; van der Vlugt & Costa, 2019; Zinger et al., 2020). Therefore, the sizes of AGN host galaxies can help us understand the relation between galaxies and AGN.

In Figure 4.17 we plot the single Sérsic semimajor axis effective radius R_{eff} as a function of M_* for our AGN sample. We also plot a colour, mass and redshift limited inactive sample of HSC galaxies taken from our error analysis fitting in

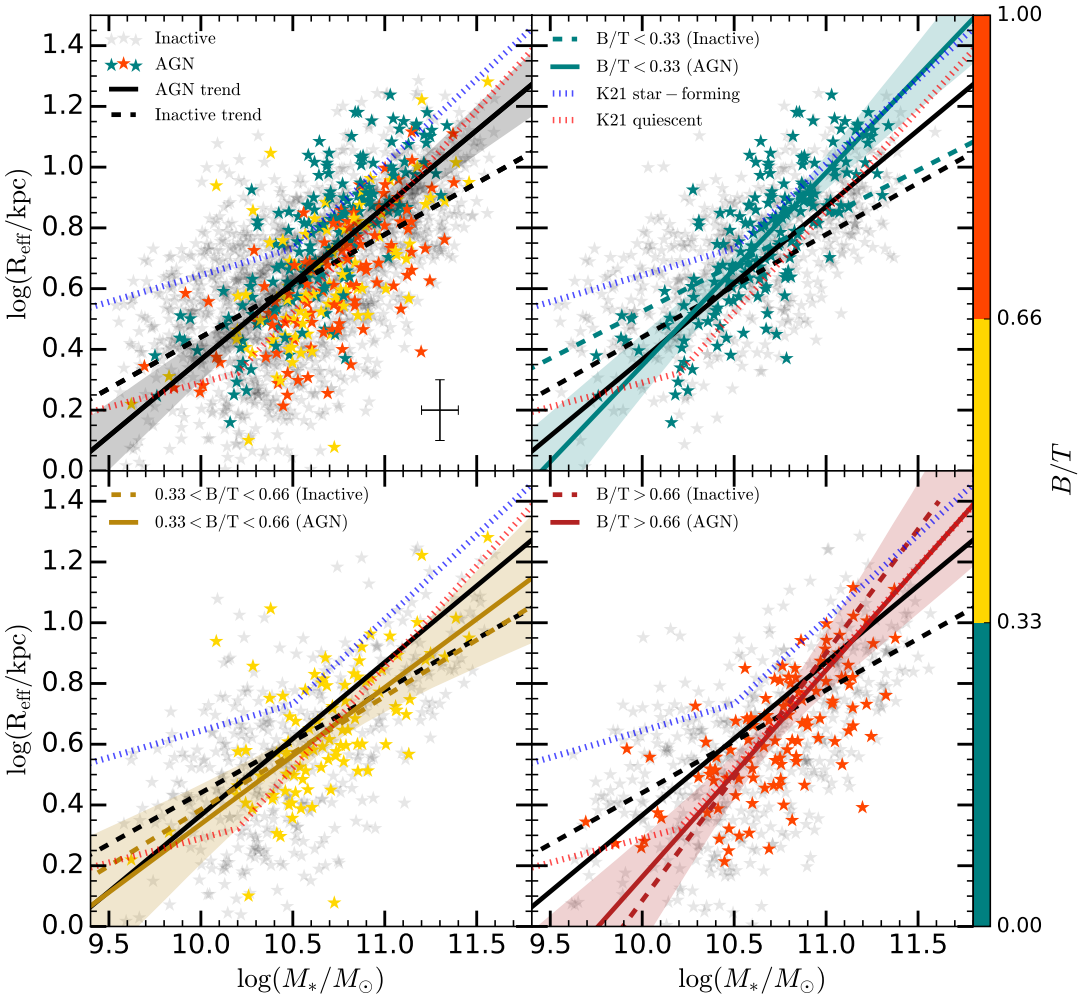

Figure 4.17: Galaxy size versus stellar mass for all galaxies (top left), disc-dominated galaxies (top right), intermediate galaxies (bottom left), and bulge-dominated galaxies (bottom right). The AGN host galaxies are shown as coloured stars, with the colour indicating B/T, and the inactive HSC galaxies are shown as grey stars. The single power-law fit to the entire AGN population and the inactive HSC galaxies is shown as a solid and dashed black line, respectively. The star-forming and quiescent double power-law relations from Kawinwanichakij et al. (2021) are shown as dotted blue and red lines, respectively. In the panels where the populations are divided into disc-dominated, intermediate, and bulge-dominated galaxies, the relations plotted for each sub-population use solid lines for the AGN sub-population and dashed lines for the inactive galaxies of each morphology class. The AGN host galaxies follow a steeper relation than the inactive galaxies.

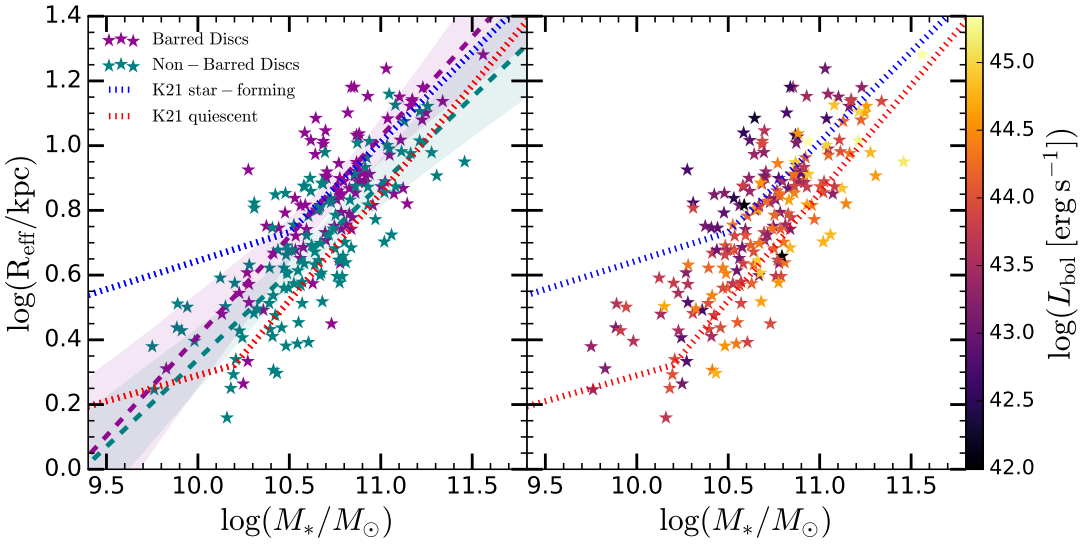

Figure 4.18: Same as top right of Figure 4.17 (disc-dominated galaxies) but with galaxies split into barred (purple) and non-barred (cyan) galaxies in the left panel. For a given stellar mass barred AGN host galaxies are on average larger than non-barred AGN host galaxies. The right panel shows the same data as the left panel, but points are coloured by bolometric AGN luminosity.

section 4.4. The AGN are shown as stars with colour denoting B/T, and the inactive galaxies are shown as grey stars. As another comparison to the general galaxy population, we include the size–mass relations from Kawinwanichakij et al. (2021)[K21], who find that their relations are best fit with double power laws. The relations are separated into star-forming and quiescent through colour–colour diagrams utilising IR photometry (i.e., UVJ diagram) (Wuyts et al., 2007; Williams et al., 2009). These relations, also measured from HSC data, are shown as a red dotted line for quiescent galaxies and a dotted blue line for star-forming galaxies.

As highlighted by previous studies (van der Wel et al., 2014; Vulcani et al., 2014; Kennedy et al., 2016), the internal colour gradients of galaxies cause size measurements to be wavelength-dependent. Therefore, for consistent rest-frame sizes and comparison with literature, we correct our i-band galaxy sizes to a wavelength of 5000Å following the method from van der Wel et al. (2014), who

give the corrected radius $R_{eff,c}$ as

$$R_{eff,c} = R_{eff,i} \left(\frac{1+z}{1+z_{\rm p}} \right)^{\Delta \log r_{eff} / \Delta \log \lambda}, \tag{4.7}$$

where $R_{eff,i}$ is the i-band effective radius, and z_p is the "pivot redshift" where the rest-frame effective wavelength of a filter is 5000Å and is 0.55 for HSC i-band. $\frac{\Delta \log r_{eff}}{\Delta \log \lambda}$ is the galaxy colour gradient, calibrated to 5000Å. For quiescent AGN host galaxies, a simple colour gradient of -0.25 is used, while for star-forming AGN host galaxies, it is formulated as

$$\frac{\Delta \log r_{eff}}{\Delta \log \lambda} = -0.35 + 0.12z - 0.25 \log \left(\frac{M_*}{10^{10}\ {\rm M}_\odot} \right) \tag{4.8}$$

We adopt the value of -0.25 for bulge-dominated galaxies and the star-forming formula for the disc-dominated and intermediate galaxies. We note that the choice is not significant enough to affect the qualitative results.

Following the approach of van der Wel et al. (2014), we assign each galaxy a weight W, which is inversely proportional to the number density based on the stellar mass function from Muzzin et al. (2013). This ensures that each mass bin carries the same weight in the fit. We fit the size-mass relations using a single-power law model as we do not see clear changes in the power law slopes.

We find a clear mass-size relation for the AGN host galaxies, as shown by the solid black line. Consistent with previous studies (Silverman et al., 2019; Li et al., 2021, 2024), we also find that the average AGN host size is in between that of quiescent and star-forming galaxies. We find that the slope for the AGN sample is steeper than that for the inactive HSC comparison sample (shown as a dashed line), mainly due to the larger sizes of the inactive HSC comparison sample below $\log (M_*/{\rm M}_\odot) = 10.5$.

As expected, we find that bulge-dominated AGN host galaxies are, on average, smaller than disc-dominated AGN host galaxies at any given mass. The mean R_{eff} for AGN host galaxies for three stellar mass bins is shown in Table 4.4.

We find that the inactive disc-dominated galaxies follow the bend in the mass-size relation for star-forming galaxies from K21, which are likely also to be disc-

Table 4.4: Mean effective radius $R_{\rm eff}$ of AGN host galaxies in different stellar mass bins for each morphological type.

Morphology	$10 < \log(M_*/\mathrm{M}_\odot) < 10.5$	$10.5 < \log(M_*/\mathrm{M}_\odot) < 11$	$11 < \log(M_*/\mathrm{M}_\odot) < 12$
Disc-dominated	3.4 kpc	6.4 kpc	10.4 kpc
Intermediate	3.5 kpc	4.3 kpc	7.0 kpc
Bulge-dominated	2.7 kpc	4.4 kpc	6.5 kpc

dominated. However, the AGN host galaxies follow a single power law, and no AGN lies on or above the star-forming relation below $\log(M_*/\mathrm{M}_\odot) = 10.3$. This is in line with previous studies, suggesting that the discs of the host galaxies of AGN are compact (Silverman et al., 2019; Li et al., 2021, 2024), which indicates that compaction may be linked to AGN activation. However, at higher masses, the disc-dominated galaxies align with the SFG relation. For bulge-dominated AGN host galaxies, we find that they agree well with inactive quiescent galaxies and bulge-dominated galaxies. We find that the intermediate galaxies are more compact than disc-dominated galaxies, with sizes similar to bulge-dominated galaxies. The AGN intermediate galaxies are also in good agreement with the inactive intermediate galaxies.

This is seemingly consistent with AGN activation correlating with a prior concentrated gas reservoir, which increases the infall probability of a gas cloud (Bournaud et al., 2011; Habouzit et al., 2019; Lapiner et al., 2021). Potential drivers of gas inflows and galaxy compaction include gas-rich mergers, counter-rotation, and violent disk instabilities. However, it is unlikely that the disc-dominated galaxies have had a major merger since $z \approx 2$ and any galaxy with evidence of tidal interactions was removed, so it is more likely that the compaction is the result of secular processes than tidally induced ones. However, previous minor mergers may no longer be discernible.

In Figure 4.18, we plot the mass-size relation for disc-dominated galaxies broken down into barred and non-barred galaxies. We find that the barred galaxies are on average larger than non-barred galaxies, with the normalisation of the barred galaxies' relation being 0.1 dex higher. While there is evidence that for the inactive population barred galaxies have larger R_{eff} than non-barred galaxies (Sanchez-Janssen & Gadotti, 2013; Díaz-García et al., 2016; Erwin, 2019), it is

not significant enough to resolve this discrepancy. Combined with the mounting evidence that bars trigger AGN (Galloway et al., 2015; Garland et al., 2023, 2024), these results could indicate that the fuelling of AGN via bars can occur in less compact galaxies than other secular processes fuelling AGN in non-barred galaxies. Detailed analysis of the molecular gas and dust distributions in barred and non-barred AGN host galaxies could investigate this. However, as shown by the left plot of Figure 4.18, the largest outliers above the mass-size relation, which are mostly barred galaxies, have lower AGN bolometric luminosities, suggesting that compaction is related to AGN fuelling. Moreover, this is at odds with a positive feedback scenario where stars are formed in AGN outflows, which increase R_{eff} (Fan et al., 2010; Ishibashi et al., 2013; Ishibashi & Fabian, 2014; Gallagher et al., 2019). If this were the case, the sizes of AGN host galaxies should increase as a function of L_{bol}, as higher luminosity drives faster outflows (Fiore et al., 2017) and faster outflows are associated with higher star formation rates (Gallagher et al., 2019).

It has been highlighted (Graham, 2019; Miller et al., 2019) that the relationship between galaxy size and mass depends on the chosen definition of radius. Typically, R_{50} is used as R_{eff}, which is the radius that encloses half the light. This is an arbitrary choice and using a different threshold may trace different processes and also follow different relations. To highlight this, we plot the mass size relations using R_{20},R_{50},R_{80}, and R_{95} in Figure 4.19. However, while the normalisations change significantly, relative slopes remain similar. The steeper relations for more disc-dominated galaxies is still potentially consistent with compaction being important in disc-dominated galaxies.

The structural properties of AGN host galaxies can provide crucial information on the triggering of AGN activity, the effect of AGN feedback, and how SMBHs and galaxies co-evolve. Through accurate decomposition and correcting for even the slight systematic biases we have found that $M_{\rm BH}$ – M_* relation is not dependent on morphology, while galaxies with different B/T follow different normalisations on the $M_{\rm BH}$ – $M_{\rm bulge}$ relation, indicating that co-evolution happens regardless of morphology and depends more on the total stellar mass than the bulge component specifically. Moreover, we find that compaction may be related to the activation of AGN in disc-dominated galaxies, which would be consistent

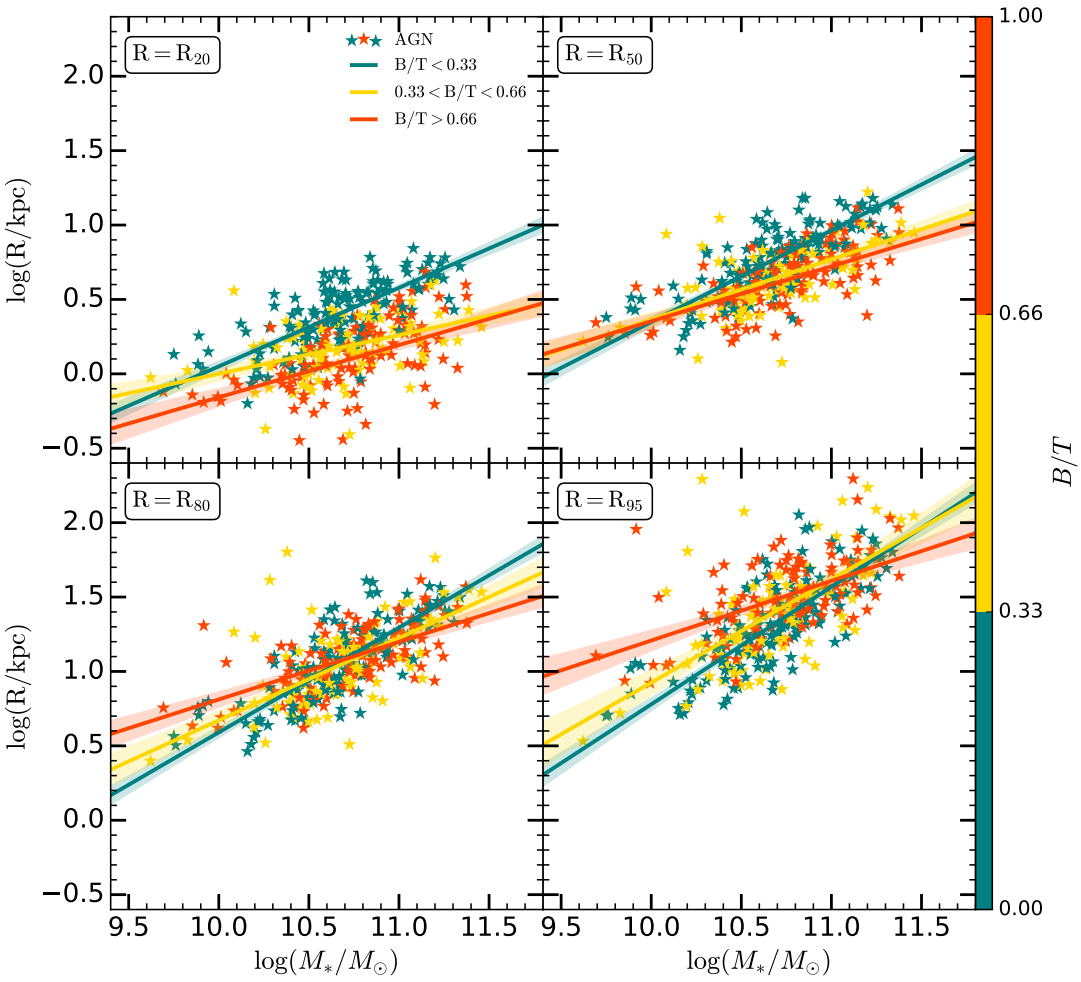

Figure 4.19: Same as top left of Figure 4.17 but each quadrant uses a different radius threshold containing 20, 50 , 80 and 95% of the light. This shows that the difference in the mass size relation is dependent on chosen definition of radius.

with AGN being in a particular evolutionary phase and not a stochastic phase on short timescales. Further work investigating how size fits in with co-evolution in this sample and disc-dominated sample from Chapter 3 is warranted.

4.6 Summary and Conclusions

We have performed multi-component 2D decomposition analysis for 415 low redshift ($0 < z < 0.35$) Type 1 AGN host galaxies in the HSC Wide survey. The decomposition analysis used Sérsic profiles for the host components and a point-spread function (PSF) model for the AGN component. We used visual analysis as well as χ^2 and the BIC to assess whether the decomposition fitting is improved with bulge, disc, and bar components. 39 galaxies are best fit with a single component while 279 and 96 are best fit with a bulge+disc and a bulge+disc+bar component respectively. The bulge components were further separated into classical (302) or pseudo-bulge (106) using the Kormendy relation.

The SDSS spectra were analysed using PyQSOFit (Ren et al., 2024): bolometric luminosity was estimated from the galaxy-flux-removed 5100 Å continuum luminosity, and black hole mass was estimated from Hβ and 5100 Å luminosities. The bolometric luminosity and black hole mass range of our sample is $L_{bol} = 10^{41} - 10^{45}$ erg s^{-1} and $M_{BH} = 10^{5.9} - 10^{9.1}$ M$_\odot$, respectively.

We estimate total stellar mass using SED fitting of AGN-subtracted photometry of the host galaxy in the g, r, i, z, y HSC wavebands. The stellar mass range of our sample is $M_* = 10^{9.6} - 10^{11.6}$ M$_\odot$. We estimate bulge mass using the bulge-to-total luminosity ratios derived from HSC i-band images and assume they correspond to the same mass ratio. The bulge stellar mass range of our sample is $M_{Bulge} = 10^{8.7} - 10^{11.3}$ M$_\odot$. We perform an error analysis of the parameters derived from decomposition of each AGN host galaxy by matching them to ≈ 15 inactive galaxies across 9 different metrics and assessing the impact of adding a point source with the same flux ratio. We find that the Sérsic index is often slightly underestimated, while most other parameters have no systematic offsets. The average error on R_{eff} and M_{Bulge} is ≈ 0.2 dex.

Our main findings are as follows:

1. For Type 1 AGN host galaxies the $M_{\rm BH}$ – M_* relation is steeper and slightly stronger than the $M_{\rm BH}$ – $M_{\rm bulge}$ relation.

2. We find no structural properties—such as B/T, bar presence, or pseudo/classical bulge presence—that correlate with deviations from the $M_{\rm BH}$ – M_* mass relation. However, B/T sets the normalisation of the $M_{\rm BH}$ – $M_{\rm bulge}$ relation. This suggests co-evolution could be independent of bulge mass and mergers.

3. The host galaxies of AGN follow a single power law mass–size relation with a positive correlation.

4. The average mass–size relation for AGN host galaxies lies between those of inactive and star-forming galaxies. This is driven by disc-dominated galaxies being more compact, while bulge-dominated AGN host sizes are consistent with those of inactive quiescent bulge-dominated galaxies.

5. The sizes of barred AGN host galaxies are larger than those of unbarred AGN host galaxies. However, the largest outliers have lower luminosities, suggesting compaction is important in AGN fuelling.

These results suggests that black hole mass is more strongly linked to the total potential of the host galaxy, as opposed to the processes that drive bulge growth. Moreover, the increased galaxy concentration in the AGN host galaxies may suggest a centrally concentrated gas distribution is necessary for AGN activation.

While the depth and resolution of HSC images allow for analysis of structural components, a matched sample using a space-based telescope such as *HST* or *Euclid* would allow for greater certainty in structural decomposition and would help to correct for systematic biases with ground-based analysis. Moreover, *HST* observations below the 4000 Å break would enable us to better determine the errors in HSC mass measurements, for the total stellar mass, bulge and bar mass. This would also allow us to determine how these systems evolve toward $z = 0$. LSST will have similar resolution and depth but with a factor of 10 larger coverage. This will create a considerably larger sample, which will significantly aid our understanding of the scaling relations.

Chapter 5

Conclusions

The results presented in this thesis contribute to our understanding of SMBH-galaxy co-evolution, by analysing different morphological populations of AGN host galaxies. In this section I briefly summarise my results, lay out how they fit into the 'big picture', and finally suggest how this work could be expanded on.

5.1 Selection effects in the total stellar mass scaling relations for disc-dominated AGN host galaxies

In Chapter 3, we investigate the selection and analysis of three samples of Type 1 AGN in disc-dominated galaxies, which produced seemingly disparate results. The three samples are from studies by Reines & Volonteri (2015), Simmons et al. (2017), and Bennert et al. (2021). While we find that the selection and analysis methods are appropriate for their respective studies, we uncover a previously unknown selection bias in the morphological analysis of the Reines & Volonteri (2015) study. The morphological classifications in that study were taken from Huertas-Company et al. (2011), who assigned morphological classifications to SDSS DR6 galaxies using a machine learning algorithm, which was not trained on AGN host galaxies. Due to the lower coverage of SDSS DR6 than SDSS DR7,

which is used in Reines & Volonteri (2015), and some galaxies not receiving a classification, only 121 of the 244 galaxies received a morphological classification. Moreover, by visually inspecting the images we determine that 24 of the galaxies were misclassified. We find that the AGN in the unclassified/misclassified subset tend to be of higher mass and luminosity than those in the classified sample. This bias leads to a 0.4 dex shift in the $M_{BH} - M_*$ relation at $M_* = 10^{10.5} M_\odot$. This is a significant shift due to the biased exclusion of sources, but it does not fully resolve the differences between this sample and the others we examine. We also noticed a trend in bolometric luminosity across the three samples, which may indicate that the three samples are selecting different parts of an underlying population.

To investigate whether the three samples are a continuous population, as hinted by the bolometric luminosity trending across the sample, we applied a selection function derived from their flux redshift distributions to a mock population of Type 1 AGN. As described in Chapter 2, the mock population of Type 1 AGN is generated by evolving a SMBH population selected from a heavy seed model mass function (Natarajan & Volonteri, 2012) at $z = 4.25$ to $z = 0$ using the probability distribution of specific black hole accretion rates (Aird et al., 2018). We find that the properties of the three samples are recoverable from the mock population and thus the three samples are consistent with being drawn from the same underlying population. This indicates that morphology cannot be the only factor in determining co-evolution for active galaxies. Moreover, the mock sample does not account for the galaxy morphology, suggesting that these disc-dominated galaxies may also consistent with the overall population, including the more bulge-dominated galaxies. A similar result was found by Zhuang & Ho (2023), who showed that early-type and late-type galaxies hosting Type 1 AGN follow very similar $M_{BH} - M_*$ relations. Utilising higher-quality photometric data of local AGN host galaxies with a broad range of morphologies would help expand on this result, and this is the motivation of the work in the subsequent chapters of this thesis.

5.2 Morphological dependence of the Black hole Bulge and Total stellar mass relations

In Chapter 4 we use multicomponent 2D decomposition of HSC images to measure the structural components of a large sample of Type 1 AGN host galaxies. The purpose of this study is to assess the morphological dependence, as indicated by the bulge to the total ratio, of $M_{BH} - M_*$, $M_{BH} - M_{Bulge}$ and the $M_* - R_{eff}$ relations. The AGN sample was selected by matching the the third data release of the HSC Subaru Strategic Program (HSCSSP) survey (Aihara et al., 2018a, 2022) with both the SDSS DR16 QSO catalogue (York et al., 2000; Lyke et al., 2020) and the AGN catalogue from Liu et al. (2019). The AGN were then re-analysed using `PyQSOFit` (Guo et al., 2018). For more reliable decomposition and to isolate the secularly growing SMBHs, we removed galaxies with evidence of recent or ongoing mergers by the visual inspection of HSC I-band images.

The sample contains 415 AGN host galaxies and spans the redshift range $0.05 < z < 0.35$. Each galaxy was fit with multiple potential components, including discs, bulges, bars, and nuclear point sources. The "best fit" to each source is determined by analysing the improvement of the BIC and extensive visual verification of the fits and their residuals. The morphologies of the AGN host galaxies show significant diversity, ranging from highly disc-dominated to highly bulge-dominated systems and spanning a total stellar mass range of $9.6 < \log(M_*/M_\odot) < 11.6$. The morphologies of galaxies, as traced by B/T, is an indicator of evolutionary history, with low B/T ratios indicating calm growth histories and larger B/T ratios indicating a history more dominated by mergers. We split the sample into three different morphological categories, based on the I-band B/T: disc-dominated with $B/T < 0.33$, intermediate galaxies with $0.33 < B/T < 0.66$, and bulge-dominated galaxies with $B/T > 0.66$. To quantify the accuracy of our decomposition, we performed a comprehensive error analysis of the decomposition, by testing the decomposition method on a matched sample of mock AGN hosts produced from real galaxies. AGN host galaxies were assigned 15 similar galaxies based on the error-weighted difference across 9 metrics, and then a point source was added to match the bulge-to-point-source flux ratio of the AGN host

galaxy. This allowed us to assign tailored uncertainty to the sample, to account for any possible source of systematic bias. The results of these simulations indicate that most parameters of AGN host galaxies can be measured reliably, with no significant systematic biases requiring correction. Most importantly for the analysis in this thesis, effective radius R_{eff} and B/T ratio are well recovered with ($\Delta \log R_{eff,Single} \approx 0.00$ dex; $1\sigma \approx -0.09$ dex) and ($\Delta \log B/T \approx 0.01$ dex; $1\sigma \approx 0.2$ dex). However, we found that the Sérsic index tends to be underestimated for AGN host galaxies and that it is only weakly related to B/T ratio or bulge classification. Conversely, we find that bulge classification as defined by the Kormendy relation is a more robust measurement.

In agreement with recent studies (Silverman et al., 2019; Li et al., 2021, 2024) we find that the average size–mass relation of AGN host galaxies is in-between that of inactive SFGs and QGs. We find that this is driven by the disc-dominated AGN host galaxies being more compact, while the more bulge-dominated galaxies are more comparable to their inactive counterparts. This suggests that AGN activity in disc-dominated galaxies may be related to compaction. We also find that barred disc galaxies are on average larger than unbarred disc galaxies at a given stellar mass. This may suggest that gas is more easily funnelled to the SMBH by galaxy bars, which is consistent with a higher incidence of AGN in barred galaxies (Garland et al., 2024). Moreover, the increased galaxy concentration in the AGN host galaxies may suggest a centrally concentrated gas distribution is necessary for AGN activation; it is possible that this process also contributes to the buildup of the bulge. Observations of molecular gas and star formation in the nuclear regions of a large and diverse sample of AGNs, covering a broad range of physical properties and evolutionary stages, are crucial for understanding how central gas concentrations form and how they are connected to SMBH activity.

In contention with some of the current literature on inactive SMBHs (Kormendy & Ho, 2013; Greene et al., 2020), we find that the $M_{BH} - M_*$ relation has no dependence on B/T, while the three morphological groups have different normalisations in the $M_{BH} - M_{Bulge}$ relation, with the disc-dominated galaxies having the highest normalisation. This suggests that regardless of the mechanism driving bulge growth, co-evolution of the galaxy and SMBH clearly occurs. Thus AGN growth may be more related to the total gravitational potential, which is

better traced by the total stellar mass than bulge mass for all galaxies. Despite our observational result disagreeing with some other studies, it agrees with some cosmological simulations. Additionally, studies focusing on highly accreting SMBHs hosted in highly disc-dominated "bulgeless" galaxies (Simmons et al., 2017; Fahey et al., 2025) and studies of higher-redshift broad-line AGN (Schramm & Silverman, 2013; Li et al., 2021, 2024) find that AGN in disc-dominated galaxies correlate more strongly with the total stellar mass of the galaxy, whereas SMBHs are over massive compared to predicted masses from the local $M_{BH} - M_{Bulge}$ relation.

Overall, Chapters 3 and 4 are consistent with a framework where black hole mass is more strongly linked to the total potential of the host galaxy, as opposed to the processes that drive bulge growth. Chapter 3 found that three samples of Type 1 AGN disc-dominated galaxies spanning different parts of the $M_{\rm BH} - M_*$ diagram are consistent with being drawn from the same mock underlying general population. This result is supported by the chapter 4, which found that galaxies of different morphological types, as determined by the B/T ratio, follow similar $M_{\rm BH} - M_*$ relations.

Further work is needed to solidify these results and to understand why the scaling relations traced out by AGN and inactive galaxies differ, and if it is driven by selection effects in both populations. The section below describes suggestions for further investigation in more detail.

5.3 Future Work

The work in this thesis has highlighted the broad nature of the AGN host population and shown that questions such as "do galaxies with different morphologies or bulge types follow the same BH scaling relations?" are more complex than previously thought. We have analysed the largest high-resolution sample of local AGN host galaxies covering a broad morphological range. We found evidence that mass of SMBHs in AGN host galaxies is more linked to the total potential of the host galaxy. However, these findings are not definitive and the new and upcoming generation of telescopes are primed to develop this work by increasing

the sample sizes by orders of magnitude with similar or superior data quality. The *Euclid* mission (Euclid Collaboration et al., 2025), successfully launched in 2023, is set to observe roughly one third of the sky over its six-year primary mission (2023-2029). Along with near-infrared photometry, it includes optical imaging in a single broad-band filter with a resolution comparable to that of HST. The *Nancy Grace Roman Space Telescope* (Kruk, 2025), scheduled for launch in 2027, will deliver HST-like resolution across wide fields in the near-infrared, The Legacy Survey of Space and Time (LSST), conducted by the Vera C. Rubin Observatory (Ivezić et al., 2019) with its 8.4-meter primary mirror is set to begin its main survey operations soon after the submission of this thesis and will cover > 18000 deg^2 with similar resolution and depth as HSC.

These studies will give us significantly more control over specific structural properties, which may be related to AGN fuelling. For example, AGN activation and activity may be related to the strength of a bar (Garland et al., 2024) and these surveys will allow us to control for bar strength. The sheer numbers of targets will also require increasing automation to processes the data. In Chapter 4 we showed that a mostly automated approach for HSC produces reliable fits, and similar studies using these surveys will need to be carried out to assess their errors. Moreover, expanding the error analysis from Chapter 4 to include barred galaxies would be beneficial when assessing how bar properties relate to AGN activation.

Moreover, the results in Chapter 4 show compaction may be related to the activation of AGN in disc-dominated galaxies. Further work investigating AGN activation, accretion rate, and location on scaling relations as a function of mass, size and morphology may produce interesting results. Investigating this for the samples in Chapter 3 would be a good starting point.

Another avenue of work is to study galaxies with reliable structural measurements would be a high spatial resolution IFU study of a sample of galaxies with similar AGN properties but with a broad range of morphologies, similar to studies by Smethurst et al. (2019, 2021). This would further our understanding of how galaxies with different morphologies are being impacted outflows from AGN feedback effects and co-evolving.

5.3.1 HST Study

Ground-based studies of quasar host galaxies have made remarkable gains by their sheer number statistics and deep depths from Pan-STARRS (Chambers et al., 2016), Subaru's HSC (Miyazaki et al., 2018) and DES (Dark Energy Survey Collaboration et al., 2016). In particular, HSC offers remarkable image quality ($0.6''$) for accurate decomposition of the quasar and host galaxy emission. These efforts have opened insight into the scaling relations as mentioned above and the structure and morphologies of the host galaxies. In particular, the wealth of structural information available with HSC is clearly seen in Figure 5.1, which approaches that possible with HST. We are only now exploring the rich HSC data set to study the inner central properties of quasar host galaxies, including their bulge mass.

While the depth and resolution of HSC images allow for analysis of structural components, a matched sample using a space-based telescope such as HST or Euclid would allow for greater certainty in structural decomposition and would help to correct for systematic biases with ground-based analysis. One benefit of HST is its UV coverage from bands such as $F225W$ and $F275W$, which allows for observations below the 4000 Å break at $z < 0.35$, which is required to assess the presence of a younger stellar population, and allows for better constraint of stellar mass and star formation rate (Paulino-Afonso et al., 2022).

One potential avenue to advance the work in this thesis and the field would be to construct a sample of active galaxies with HST observations bracketing the 4000 Åbreak. A study like this would enable us to more accurately measure the stellar mass of the host galaxies and their individual structural components. This will greatly facilitate answering one of the most critical questions in black hole–galaxy co-evolution: "Is supermassive black hole (SMBH) growth related to the overall gravitational potential, or to the formation of a bulge?" Utilising the spatially resolved SED fitting would allow us to determine where star formation is taking place and how that is impacting evolution on the $M_{BH} - M_*$ and $M_{BH} - M_{Bulge}$ relations. These observations would also serve as a gold standard for assessing systematic biases in wide-field, deep imaging surveys, including HSC, DES, Euclid, Roman and Rubin, which have lower spatial resolution and limited

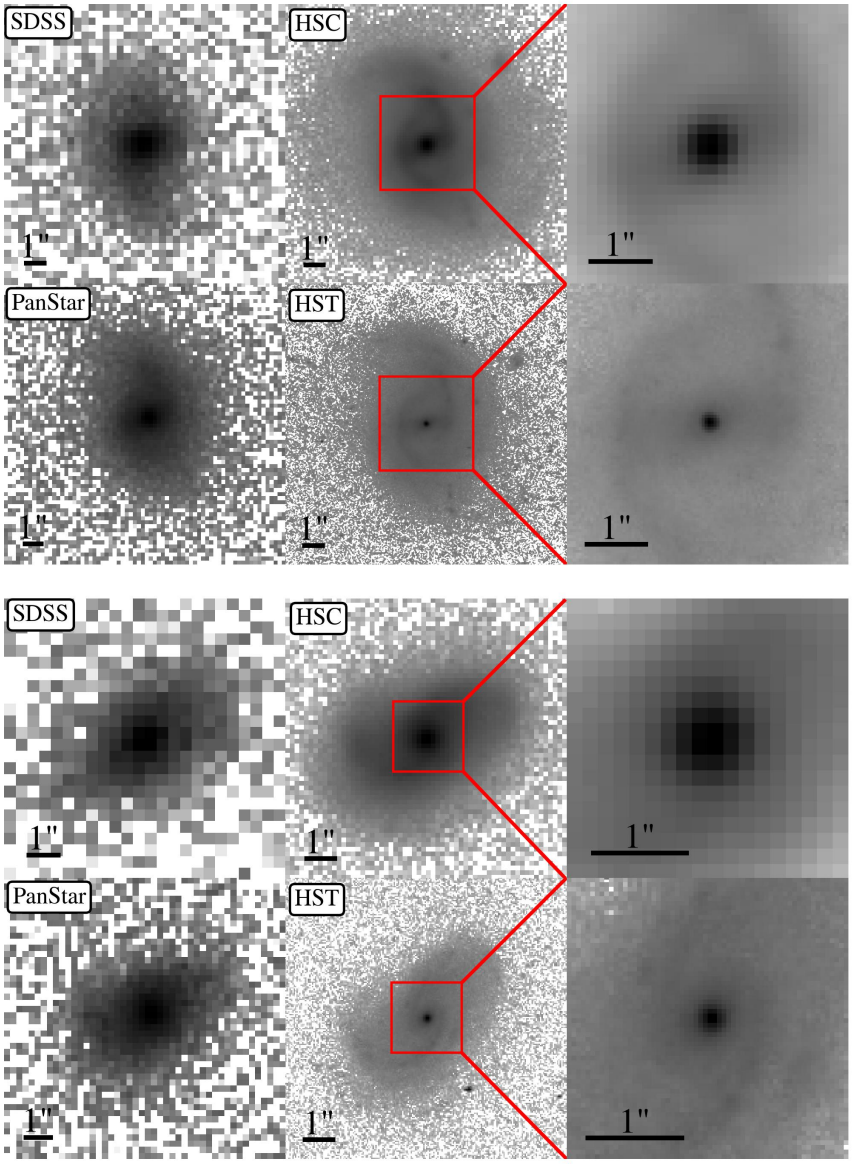

Figure 5.1: Example images of AGN host galaxies in the i band for SDSS, Pan-STARRS, Subaru/HSC and HST ($F814W$). The internal structure is clearly revealed in HSC and as shown by the zoomed-in HST image at greater resolution for mapping the properties of the nuclear region (i.e., bulge and inner bar).

coverage below the 4000 Å break. It would also provide a low-z comparison sample for high-z studies of quasar hosts with JWST.

There is already a significant number (> 150) of AGN host galaxies at $z < 0.35$ that have at least 1 HST observation, of which ≈ 10 are also covered by HSC and span a range of stellar masses and AGN luminosities. While a number of galaxies have also been observed in HST bands below 4000 Å; their exposure times are short and do not meet the requirements for structural analysis. Therefore, a proposal to observe these galaxies below the 4000 Å break would be very beneficial to the study of co-evolution.

Overall, the future is very bright for this area of study, with upcoming surveys and improved analysis techniques poised to greatly deepen our understanding of SMBH - Galaxy co-evolution.

References

Abazajian K. N., et al., 2009, ApJS, 182, 543

Abraham R. G., Merrifield M. R., 2000, AJ, 120, 2835

Adelman-McCarthy J. K., et al., 2008, ApJS, 175, 297

Aguerri J. A. L., Méndez-Abreu J., Corsini E. M., 2009, A&A, 495, 491

Aihara H., et al., 2011, ApJS, 193, 29

Aihara H., et al., 2018a, PASJ, 70, S4

Aihara H., et al., 2018b, PASJ, 70, S8

Aihara H., et al., 2022, PASJ, 74, 247

Aird J., et al., 2010, MNRAS, 401, 2531

Aird J., et al., 2012, ApJ, 746, 90

Aird J., Coil A. L., Georgakakis A., Nandra K., Barro G., Pérez-González P. G., 2015, MNRAS, 451, 1892

Aird J., Coil A. L., Georgakakis A., 2018, MNRAS, 474, 1225

Aird J., Coil A. L., Georgakakis A., 2019, MNRAS, 484, 4360

Aird J. A., Quon E. W., Barthelmie R. J., Pryor S. C., 2022, in Journal of Physics Conference Series. IOP, p. 032077, doi:10.1088/1742-6596/2265/3/032077

Alexander D. M., Lehmer B., Geach J., Bauer F., Chapman S., Matsuda Y., Smail I., Yamada T., 2008, in Ehle M., Diaz-Trigo M., eds, The X-ray Universe 2008. p. 127

Allen P. D., Driver S. P., Graham A. W., Cameron E., Liske J., de Propris R., 2006, MNRAS, 371, 2

Allevato V., et al., 2011, ApJ, 736, 99

Ananna T. T., et al., 2022, ApJS, 261, 9

Antonucci R. R. J., 1984, ApJ, 278, 499

Antonucci R., 1993, ARA&A, 31, 473

Assef R. J., et al., 2013, ApJ, 772, 26

Athanassoula E., 1992a, MNRAS, 259, 328

Athanassoula E., 1992b, MNRAS, 259, 345

Athanassoula E., Bosma A., 2003, Astrophysics and Space Science, 284, 491

Athanassoula E., Machado R. E. G., Rodionov S. A., 2013, MNRAS, 429, 1949

Baade W., Minkowski R., 1954, ApJ, 119, 206

Baldassare V. F., Reines A. E., Gallo E., Greene J. E., 2015, ApJL, 809, L14

Baldry I. K., Glazebrook K., Brinkmann J., Ivezić Ž., Lupton R. H., Nichol R. C., Szalay A. S., 2004, ApJ, 600, 681

Baldwin J. A., Phillips M. M., Terlevich R., 1981, PASP, 93, 5

Bamford S. P., et al., 2009, MNRAS, 393, 1324

Barazza F. D., Jogee S., Marinova I., 2008, ApJ, 675, 1194

Batcheldor D., 2010, ApJL, 711, L108

Baugh C. M., Cole S., Frenk C. S., Lacey C. G., 1998, ApJ, 498, 504

Baugh C. M., Lacey C. G., Frenk C. S., Granato G. L., Silva L., Bressan A., Benson A. J., Cole S., 2005, MNRAS, 356, 1191

Beckmann R. S., et al., 2017, MNRAS, 472, 949

Beckmann R. S., et al., 2024, MNRAS, 527, 10867

Begelman M. C., Blandford R. D., Rees M. J., 1980, Nature, 287, 307

Bekki K., 1998, ApJ, 496, 713

Bell E. F., et al., 2004, ApJ, 608, 752

Bell E. F., Monachesi A., Harmsen B., de Jong R. S., Bailin J., Radburn-Smith D. J., D'Souza R., Holwerda B. W., 2017, ApJL, 837, L8

Bellovary J., Brooks A., Volonteri M., Governato F., Quinn T., Wadsley J., 2013, ApJ, 779, 136

Bennert V. N., Auger M. W., Treu T., Woo J.-H., Malkan M. A., 2011, ApJ, 726, 59

Bennert V. N., et al., 2015, ApJ, 809, 20

Bennert V. N., et al., 2021, arXiv e-prints, p. arXiv:2101.10355

Bennett C. L., et al., 2013, ApJS, 208, 20

Bentz M. C., et al., 2013, ApJ, 767, 149

Bernardi M., Sheth R. K., Tundo E., Hyde J. B., 2007, ApJ, 660, 267

Binney J., Merrifield M., 1998, Galactic astronomy. Galactic astronomy / James Binney and Michael Merrifield. Princeton, NJ : Princeton University Press, 1998. (Princeton series in astrophysics) QB857 .B522 1998

Birrer S., Amara A., 2018, Lenstronomy: Multi-purpose gravitational lens modeling software package, Astrophysics Source Code Library, record ascl:1804.012

Blandford R. D., McKee C. F., 1982, ApJ, 255, 419

Blumenthal G. R., Faber S. M., Primack J. R., Rees M. J., 1984, Nature, 311, 517

Bohn T., Canalizo G., Satyapal S., Sales L. V., 2022, ApJ, 931, 69

Bongiorno A., et al., 2012, MNRAS, 427, 3103

Boquien M., 2020, in American Astronomical Society Meeting Abstracts #235. p. 228.01

Bosch J., et al., 2018, PASJ, 70, S5

Bournaud F., Elmegreen B. G., Elmegreen D. M., 2007, ApJ, 670, 237

Bournaud F., Dekel A., Teyssier R., Cacciato M., Daddi E., Juneau S., Shankar F., 2011, ApJL, 741, L33

Bournaud F., et al., 2014, ApJ, 780, 57

Bower R. G., Balogh M. L., 2004, in Mulchaey J. S., Dressler A., Oemler A., eds, Clusters of Galaxies: Probes of Cosmological Structure and Galaxy Evolution. p. 325 (arXiv:astro-ph/0306342), doi:10.48550/arXiv.astro-ph/0306342

Boylan-Kolchin M., Ma C.-P., Quataert E., 2005, MNRAS, 362, 184

Boyle B. J., Terlevich R. J., 1998, MNRAS, 293, L49

Brammer G. B., et al., 2009, ApJL, 706, L173

Brandt W. N., Alexander D. M., 2015, The Astronomy and Astrophysics Review, 23, 1

Bruce V. A., Dunlop J. S., Mortlock A., Kocevski D. D., McGrath E. J., Rosario D. J., 2016, MNRAS, 458, 2391

Bruzual G., Charlot S., 2003, MNRAS, 344, 1000

Burbidge G. R., Burbidge E. M., Sandage A. R., 1963, Reviews of Modern Physics, 35, 947

Buta R. J., 2017, MNRAS, 470, 3819

Buta R., Combes F., 1996, Fundamentals of Cosmic Physics, 17, 95

Buta R. J., et al., 2019, MNRAS, 488, 2175

Calzetti D., Armus L., Bohlin R. C., Kinney A. L., Koornneef J., Storchi-Bergmann T., 2000, ApJ, 533, 682

Cann J. M., Satyapal S., Abel N. P., Blecha L., Mushotzky R. F., Reynolds C. S., Secrest N. J., 2019, ApJL, 870, L2

Cappellari M., et al., 2011, MNRAS, 416, 1680

Cappelluti N., et al., 2009, A&A, 497, 635

Casteels K. R. V., et al., 2013, MNRAS, 429, 1051

Chabrier G., 2003, PASP, 115, 763

Chambers K. C., et al., 2016, arXiv e-prints, p. arXiv:1612.05560

Chapman S. C., Blain A. W., Smail I., Ivison R. J., 2005, ApJ, 622, 772

Cheung E., et al., 2015, MNRAS, 447, 506

Ciesla L., et al., 2015, A&A, 576, A10

Circosta C., et al., 2019, A&A, 623, A172

Cisternas M., Jahnke K., 2015, Highlights of Astronomy, 16, 344

Cisternas M., et al., 2011a, ApJ, 726, 57

Cisternas M., et al., 2011b, ApJL, 741, L11

Coldwell G. V., Alonso S., Duplancic F., Mesa V., 2018, MNRAS, 476, 2457

Combes F., 2017, Frontiers in Astronomy and Space Sciences, 4, 10

Combes F., 2020, in Valluri M., Sellwood J. A., eds, IAU Symposium Vol. 353, Galactic Dynamics in the Era of Large Surveys. pp 155–161 (arXiv:1908.03149), doi:10.1017/S1743921319007397

Costantin L., et al., 2023, Nature, 623, 499

Coulton W. R., Armstrong R., Smith K. M., Lupton R. H., Spergel D. N., 2018, AJ, 155, 258

Croton D. J., et al., 2006, MNRAS, 365, 11

Cui Y., Xiang Y., Rong K., Feris R., Cao L., 2014, in IEEE Winter Conference on Applications of Computer Vision. pp 213–219, doi:10.1109/WACV.2014.6836098

Czerny B., Hryniewicz K., 2011, A&A, 525, L8

Daddi E., et al., 2007, ApJ, 670, 173

Damjanov I., et al., 2009, ApJ, 695, 101

Dark Energy Survey Collaboration et al., 2016, MNRAS, 460, 1270

Davies R. I., Maciejewski W., Hicks E. K. S., Tacconi L. J., Genzel R., Engel H., 2009, ApJ, 702, 114

Davis B. L., Graham A. W., Combes F., 2019, ApJ, 877, 64

Dekel A., Silk J., 1986, ApJ, 303, 39

Della Ceca R., et al., 2008, A&A, 487, 119

Delvecchio I., et al., 2014, MNRAS, 439, 2736

Di Matteo T., Springel V., Hernquist L., 2005, Nature, 433, 604

Díaz-García S., Salo H., Laurikainen E., 2016, A&A, 596, A84

Ding X., et al., 2020, ApJ, 888, 37

Ding X., Birrer S., Treu T., Silverman J. D., 2021, arXiv e-prints, p. arXiv:2111.08721

Djorgovski S., Davis M., 1987, ApJ, 313, 59

Dobbs C., Baba J., 2014, PASA, 31, e035

Dominiak P., et al., 2024, arXiv e-prints, p. arXiv:2404.11260

Dressler A., 1980, ApJ, 236, 351

Dressler A., 1987, ApJ, 317, 1

Dressler A., Richstone D. O., 1988, ApJ, 324, 701

Dreyer J. L. E., 1888, Memoirs of the Royal Astronomical Society, 49, 1

Du P., Wang J.-M., Zhang Z.-X., 2017, ApJL, 840, L6

Du M., Ho L. C., Debattista V. P., Pillepich A., Nelson D., Hernquist L., Weinberger R., 2021, ApJ, 919, 135

Dubois Y., et al., 2014, MNRAS, 444, 1453

Dubois Y., Peirani S., Pichon C., Devriendt J., Gavazzi R., Welker C., Volonteri M., 2016, MNRAS, 463, 3948

Dullemond C. P., van Bemmel I. M., 2005, A&A, 436, 47

Dutton A. A., 2009, MNRAS, 396, 121

Edelson R., Malkan M., 2012, ApJ, 751, 52

Efstathiou G., Lake G., Negroponte J., 1982, MNRAS, 199, 1069

Elmegreen D. M., Sundin M., Elmegreen B., Sundelius B., 1991, A&A, 244, 52

Elmegreen B. G., Elmegreen D. M., Vollbach D. R., Foster E. R., Ferguson T. E., 2005, ApJ, 634, 101

Elvis M., et al., 1994, ApJS, 95, 1

Emsellem E., et al., 2011, MNRAS, 414, 888

Erwin P., 2004, A&A, 415, 941

Erwin P., 2015, ApJ, 799, 226

Erwin P., 2018, MNRAS, 474, 5372

Erwin P., 2019, MNRAS, 489, 3553

Eskridge P. B., et al., 2000, AJ, 119, 536

Euclid Collaboration et al., 2025, A&A, 697, A1

Fabian A. C., 1999, MNRAS, 308, L39

Fabian A. C., 2012, ARA&A, 50, 455

Fabian A. C., Allen S. W., Crawford C. S., Johnstone R. M., Morris R. G., Sanders J. S., Schmidt R. W., 2002, MNRAS, 332, L50

Fahey M. J., et al., 2025, MNRAS, 537, 3511

Fan L., Lapi A., Bressan A., Bernardi M., De Zotti G., Danese L., 2010, ApJ, 718, 1460

Fanali R., Dotti M., Fiacconi D., Haardt F., 2015, MNRAS, 454, 3641

Fath E. A., 1909, Lick Observatory Bulletin, 149, 71

Ferrarese L., Merritt D., 2000, ApJL, 539, L9

Ferrarese L., Pogge R. W., Peterson B. M., Merritt D., Wandel A., Joseph C. L., 2001, ApJL, 555, L79

Ferreira L., et al., 2023, ApJ, 955, 94

Fiore F., et al., 2017, A&A, 601, A143

Fisher D. B., Drory N., 2008, AJ, 136, 773

Flesch E. W., 2023, The Open Journal of Astrophysics, 6, 49

Fornasini F. M., Civano F., Fabbiano G., Elvis M., Marchesi S., Miyaji T., Zezas A., 2018, ApJ, 865, 43

Fotopoulou S., et al., 2016, A&A, 587, A142

Fritz J., Franceschini A., Hatziminaoglou E., 2006, MNRAS, 366, 767

Gadotti D. A., 2009, MNRAS, 393, 1531

Gadotti D. A., 2011, MNRAS, 415, 3308

Gallagher R., Maiolino R., Belfiore F., Drory N., Riffel R., Riffel R. A., 2019, MNRAS, 485, 3409

Galloway M. A., et al., 2015, MNRAS, 448, 3442

Gargiulo I. D., Cora S. A., Vega-Martínez C. A., Gonzalez O. A., Zoccali M., González R., Ruiz A. N., Padilla N. D., 2017, MNRAS, 472, 4133

Garland I. L., et al., 2023, MNRAS, 522, 211

Garland I. L., et al., 2024, MNRAS, 532, 2320

Gebhardt K., Thomas J., 2009, ApJ, 700, 1690

Gebhardt K., et al., 2000, ApJL, 539, L13

Gebhardt K., et al., 2003, ApJ, 583, 92

Genzel R., Thatte N., Krabbe A., Kroker H., Tacconi-Garman L. E., 1996, ApJ, 472, 153

Genzel R., Eisenhauer F., Gillessen S., 2010, Reviews of Modern Physics, 82, 3121

George K., Subramanian S., Paul K. T., 2019, A&A, 628, A24

Gerin M., Combes F., Athanassoula E., 1990, A&A, 230, 37

Géron T., Smethurst R. J., Lintott C., Kruk S., Masters K. L., Simmons B., Stark D. V., 2021, MNRAS, 507, 4389

Ghez A. M., Klein B. L., Morris M., Becklin E. E., 1998, ApJ, 509, 678

Ghez A. M., et al., 2008, ApJ, 689, 1044

Ghosh A., et al., 2023, ApJ, 953, 134

Gillessen S., Eisenhauer F., Trippe S., Alexander T., Genzel R., Martins F., Ott T., 2009, ApJ, 692, 1075

Glikman E., Simmons B., Mailly M., Schawinski K., Urry C. M., Lacy M., 2015, ApJ, 806, 218

Goulding A. D., et al., 2017, ApJ, 843, 135

Graham A. W., 2001, AJ, 121, 820

Graham A. W., 2004, ApJL, 613, L33

Graham A. W., 2012, ApJ, 746, 113

Graham A. W., 2019, PASA, 36, e035

Graham A. W., 2023, MNRAS, 518, 6293

Graham A. W., Driver S. P., 2007, ApJ, 655, 77

Graham A. W., Sahu N., 2023, MNRAS, 520, 1975

Graham A. W., Scott N., 2013, ApJ, 764, 151

Graham A. W., Onken C. A., Athanassoula E., Combes F., 2011, MNRAS, 412, 2211

Greene J. E., Ho L. C., 2005, ApJ, 630, 122

Greene J. E., Ho L. C., 2007, ApJ, 667, 131

Greene J. E., Strader J., Ho L. C., 2020, ARA&A, 58, 257

Grier C. J., et al., 2013, ApJ, 764, 47

Grogin N. A., et al., 2005, ApJL, 627, L97

Guedes J., Mayer L., Carollo M., Madau P., 2013, ApJ, 772, 36

Gültekin K., et al., 2009, ApJ, 698, 198

Gültekin K., Tremaine S., Loeb A., Richstone D. O., 2011, ApJ, 738, 17

Guo H., Shen Y., Wang S., 2018, PyQSOFit: Python Code to Fit the Spectrum of Quasars, Astrophysics Source Code Library, `http://ascl.net/1809.008`

Guo M., Du M., Ho L. C., Debattista V. P., Zhao D., 2020, ApJ, 888, 65

Guo Y., et al., 2023, ApJL, 945, L10

Habouzit M., et al., 2019, MNRAS, 484, 4413

Hafez I., 2010, PhD thesis, James Cook University, Australia

Hagen S., et al., 2024, MNRAS, 534, 2803

Haiman Z., Ciotti L., Ostriker J. P., 2004, ApJ, 606, 763

Hamabe M., Kormendy J., 1987, in de Zeeuw P. T., ed., IAU Symposium Series Vol. 127, IAU Symposium. International Astronomical Union, pp 379–380

Hao L., et al., 2005, AJ, 129, 1783

Hardcastle M., 2018, Nature Astronomy, 2, 273

Hardcastle M. J., Evans D. A., Croston J. H., 2007, MNRAS, 376, 1849

Häring N., Rix H.-W., 2004, ApJL, 604, L89

Harris C. E., Bennert V. N., Auger M. W., Treu T., Woo J.-H., Malkan M. A., 2012, ApJS, 201, 29

Harrison C. M., et al., 2012, ApJL, 760, L15

Harrison C. M., Alexander D. M., Mullaney J. R., Swinbank A. M., 2014, MNRAS, 441, 3306

Hart R. E., Bamford S. P., Casteels K. R. V., Kruk S. J., Lintott C. J., Masters K. L., 2017, MNRAS, 468, 1850

Hartmann M., Debattista V. P., Cole D. R., Valluri M., Widrow L. M., Shen J., 2014, MNRAS, 441, 1243

Hasinger G., Miyaji T., Schmidt M., 2005, A&A, 441, 417

Hasinger G., et al., 2007, ApJS, 172, 29

Hayward C. C., et al., 2014, MNRAS, 445, 1598

Heckman T. M., 1980, A&A, 87, 152

Heckman T. M., Best P. N., 2014, ARA&A, 52, 589

Herpich J., Tremaine S., Rix H.-W., 2017, MNRAS, 467, 5022

Herschel W., 1786, Philosophical Transactions of the Royal Society of London Series I, 76, 457

Hickox R. C., Alexander D. M., 2018, ARA&A, 56, 625

Hickox R. C., Mullaney J. R., Alexander D. M., Chen C.-T. J., Civano F. M., Goulding A. D., Hainline K. N., 2014, ApJ, 782, 9

Hilz M., Naab T., Ostriker J. P., Thomas J., Burkert A., Jesseit R., 2012, MNRAS, 425, 3119

Hirschmann M., Khochfar S., Burkert A., Naab T., Genel S., Somerville R. S., 2010, MNRAS, 407, 1016

Ho L. C., Kim M., 2014, ApJ, 789, 17

Hopkins P. F., Hernquist L., 2009a, ApJ, 694, 599

Hopkins P. F., Hernquist L., 2009b, ApJ, 694, 599

Hopkins P. F., Hernquist L., 2009c, ApJ, 698, 1550

Hopkins P. F., Hernquist L., Cox T. J., Robertson B., Di Matteo T., Springel V., 2006, ApJ, 639, 700

Hopkins P. F., Cox T. J., Younger J. D., Hernquist L., 2009, ApJ, 691, 1168

Hopkins P. F., Quataert E., Murray N., 2012, MNRAS, p. 2655

Hopkins P. F., Torrey P., Faucher-Giguère C.-A., Quataert E., Murray N., 2016, MNRAS, 458, 816

Hoyle F., Fowler W. A., 1963, MNRAS, 125, 169

Hubble E. P., 1926, ApJ, 64, 321

Hubble E. P., 1936, Realm of the Nebulae. Yale University Press

Huertas-Company M., Aguerri J. A. L., Bernardi M., Mei S., Sánchez Almeida J., 2011, A&A, 525, A157

Ishibashi W., Fabian A. C., 2012, MNRAS, 427, 2998

Ishibashi W., Fabian A. C., 2014, MNRAS, 441, 1474

Ishibashi W., Fabian A. C., Canning R. E. A., 2013, MNRAS, 431, 2350

Ivezić Ž., et al., 2019, ApJ, 873, 111

Jacobs C., et al., 2023, ApJL, 948, L13

Jahnke K., Macciò A. V., 2011, ApJ, 734, 92

Jahnke K., et al., 2009, ApJL, 706, L215

Ji Z., Giavalisco M., Kirkpatrick A., Kocevski D., Daddi E., Delvecchio I., Hatcher C., 2022, ApJ, 925, 74

Jones M. L., Hickox R. C., Mutch S. J., Croton D. J., Ptak A. F., DiPompeo M. A., 2017, ApJ, 843, 125

Kannan R., Macciò A. V., Fontanot F., Moster B. P., Karman W., Somerville R. S., 2015, MNRAS, 452, 4347

Kant I., 1755, Allgemeine Naturgeschichte und Theorie des Himmels. Petersen, Königsberg und Leipzig, https://korpora.zim.uni-duisburg-essen.de/Kant/aa01/215.html

Kaspi S., Smith P. S., Netzer H., Maoz D., Jannuzi B. T., Giveon U., 2000, ApJ, 533, 631

Kass R. E., Raftery A. E., 1995, Journal of the American Statistical Association, 90, 773

Kass, R. E Raftery A. E., 1978, Journal of theAmerican Statistical Association, 6, 461

Kataria S. K., Vivek M., 2024, MNRAS, 527, 3366

Kauffmann G., Colberg J. M., Diaferio A., White S. D. M., 1999a, MNRAS, 303, 188

Kauffmann G., Colberg J. M., Diaferio A., White S. D. M., 1999b, MNRAS, 307, 529

Kauffmann G., et al., 2003, MNRAS, 346, 1055

Kaviraj S., et al., 2017, MNRAS, 467, 4739

Kawanomoto S., et al., 2018, PASJ, 70, 66

Kawinwanichakij L., et al., 2021, ApJ, 921, 38

Kelly B. C., 2007, ApJ, 665, 1489

Kennedy J., Eberhart R., 1995, in Proceedings of ICNN'95 - International Conference on Neural Networks. pp 1942–1948 vol.4, doi:10.1109/ICNN.1995.488968

Kennedy R., Bamford S. P., Häußler B., Brough S., Holwerda B., Hopkins A. M., Vika M., Vulcani B., 2016, A&A, 593, A84

Kent S. M., 1985, ApJS, 59, 115

Kerr R. P., 1963, Physical Review Letters, 11, 237

Kewley L. J., Groves B., Kauffmann G., Heckman T., 2006, MNRAS, 372, 961

Khachikian E. Y., Weedman D. W., 1974, ApJ, 192, 581

Kim M., Ho L. C., Peng C. Y., Barth A. J., Im M., 2008, ApJS, 179, 283

King A., 2003, ApJL, 596, L27

King A., 2005, ApJL, 635, L121

Kitzbichler M. G., White S. D. M., 2006, MNRAS, 366, 858

Knapen J. H., Shlosman I., Peletier R. F., 2000, ApJ, 529, 93

Kocevski D. D., et al., 2012, ApJ, 744, 148

Kocevski D. D., et al., 2015, ApJ, 814, 104

Kolmogorov A., 1933, Inst. Ital. Attuari, Giorn., 4, 83

Kormendy J., 1977, ApJ, 214, 359

Kormendy J., 2016, in Laurikainen E., Peletier R., Gadotti D., eds, Astrophysics and Space Science Library Vol. 418, Galactic Bulges. p. 431 (arXiv:1504.03330), doi:10.1007/978-3-319-19378-6˙16

Kormendy J., Ho L. C., 2013, ARA&A, 51, 511

Kormendy J., Kennicutt Jr. R. C., 2004, ARA&A, 42, 603

Kormendy J., Richstone D., 1995, ARA&A, 33, 581

Kormendy J., Drory N., Bender R., Cornell M. E., 2010, ApJ, 723, 54

Koss M., Mushotzky R., Veilleux S., Winter L. M., Baumgartner W., Tueller J., Gehrels N., Valencic L., 2011, ApJ, 739, 57

Koss M., et al., 2017, ApJ, 850, 74

Koss M. J., et al., 2022, ApJS, 261, 2

Kovačević A. B., et al., 2022, ApJS, 262, 49

Kraljic K., Bournaud F., Martig M., 2012, ApJ, 757, 60

Kroupa P., 2001, MNRAS, 322, 231

Kruk J., 2025, in American Astronomical Society Meeting Abstracts #245. p. 305.13

Kruk S. J., et al., 2018, MNRAS, 473, 4731

Lacerda E. A. D., Sánchez S. F., Cid Fernandes R., López-Cobá C., Espinosa-Ponce C., Galbany L., 2020, MNRAS, 492, 3073

Lammers C., Iyer K. G., Ibarra-Medel H., Pacifici C., Sánchez S. F., Tacchella S., Woo J., 2023, ApJ, 953, 26

Lang M., Holley-Bockelmann K., Sinha M., 2014, ApJL, 790, L33

Laor A., 1998, ApJL, 505, L83

Laor A., 2001, ApJ, 553, 677

Laor A., Draine B. T., 1993, ApJ, 402, 441

Lapiner S., Dekel A., Dubois Y., 2021, MNRAS, 505, 172

Läsker R., Ferrarese L., van de Ven G., 2014, ApJ, 780, 69

Laurikainen E., Salo H., 2002, MNRAS, 337, 1118

Le Conte Z. A., et al., 2024, MNRAS, 530, 1984

Lee G.-H., Woo J.-H., Lee M. G., Hwang H. S., Lee J. C., Sohn J., Lee J. H., 2012, ApJ, 750, 141

Lehmer B. D., Alexander D. M., Bauer F. E., Brandt W. N., Goulding A. D., Jenkins L. P., Ptak A., Roberts T. P., 2010, ApJ, 724, 559

Lelli F., Di Teodoro E. M., Fraternali F., Man A. W. S., Zhang Z.-Y., De Breuck C., Davis T. A., Maiolino R., 2021, Science, 371, 713

Leslie S. K., Kewley L. J., Sanders D. B., Lee N., 2016, MNRAS, 455, L82

Li C., Kauffmann G., Heckman T. M., White S. D. M., Jing Y. P., 2008, MNRAS, 385, 1915

Li J., et al., 2021, ApJ, 918, 22

Li J., et al., 2024, MNRAS, 527, 4690

Lin Y., Cervantes Sodi B., Li C., Wang L., Wang E., 2014, ApJ, 796, 98

Lindblad P. O., 1960, Stockholms Observatoriums Annaler, 4, 4

Liu H.-Y., Liu W.-J., Dong X.-B., Zhou H., Wang T., Lu H., Yuan W., 2019, ApJS, 243, 21

Lodato C., Lopes S., 2006, Journal of Mathematical Imaging and Vision, 26, 345

Lodato L., Spampinato L., Harris A., Calvari S., Dehn J., Patrick M., 2007, Bulletin of Volcanology, 69, 661

Lopes P. A. A., Rembold S. B., Ribeiro A. L. B., Nascimento R. S., Vajgel B., 2016, MNRAS, 461, 2559

Lotz J. M., Jonsson P., Cox T. J., Croton D., Primack J. R., Somerville R. S., Stewart K., 2011, ApJ, 742, 103

Lyke B. W., et al., 2020, ApJS, 250, 8

Lynden-Bell D., 1969, Nature, 223, 690

Lynden-Bell D., Rees M. J., 1971, MNRAS, 152, 461

Lynds R., Toomre A., 1976, ApJ, 209, 382

Lyu J., Rieke G., 2022, Universe, 8, 304

Madau P., Dickinson M., 2014, ARA&A, 52, 415

Madau P., Rees M. J., 2001, ApJL, 551, L27

Magorrian J., et al., 1998, AJ, 115, 2285

Mahajan S., et al., 2020, MNRAS, 491, 398

Mandelker N., Dekel A., Ceverino D., Tweed D., Moody C. E., Primack J., 2014, MNRAS, 443, 3675

Marconi A., Hunt L. K., 2003, ApJL, 589, L21

Marels V., Mesa V., Jaque Arancibia M., Alonso S., Coldwell G., Damke G., Contreras Rojas V., 2025, arXiv e-prints, p. arXiv:2505.23958

Marian V., et al., 2019, ApJ, 882, 141

Marinova I., Jogee S., 2007, ApJ, 659, 1176

Martig M., Bournaud F., Croton D. J., Dekel A., Teyssier R., 2012, ApJ, 756, 26

Martin G., et al., 2018, MNRAS, 476, 2801

Martini P., Regan M. W., Mulchaey J. S., Pogge R. W., 2003, ApJ, 589, 774

Masters K. L., et al., 2010, MNRAS, 404, 792

Masters K. L., et al., 2011, MNRAS, 411, 2026

Mayo J. H., Lawrence A., 2013, MNRAS, 434, 1593

McAlpine S., et al., 2016, Astronomy and Computing, 15, 72

McAlpine S., Harrison C. M., Rosario D. J., Alexander D. M., Ellison S. L., Johansson P. H., Patton D. R., 2020, MNRAS, 494, 5713

McConnell N. J., Ma C.-P., 2013, ApJ, 764, 184

Mechtley M., et al., 2016, ApJ, 830, 156

Melvin T., et al., 2014, MNRAS, 438, 2882

Méndez-Abreu J., Sánchez-Janssen R., Aguerri J. A. L., Corsini E. M., Zarattini S., 2012, ApJL, 761, L6

Merloni A., et al., 2013, Monthly Notices of the Royal Astronomical Society, 437, 3550

Merloni A., et al., 2014, MNRAS, 437, 3550

Merritt D., 2006, ApJ, 648, 976

Merritt D., Ferrarese L., 2001, ApJ, 547, 140

Messier C., 1781, Catalogue des Nébuleuses et des Amas d'Étoiles (Catalog of Nebulae and Star Clusters), Connoissance des Temps ou des Mouvements Célestes, for 1784, p. 227-267

Mezcua M., Domínguez Sánchez H., 2024, MNRAS, 528, 5252

Michikoshi S., Kokubo E., 2020, ApJ, 897, 65

Mihos J. C., Hernquist L., 1994, ApJL, 431, L9

Mihos J. C., Hernquist L., 1996, ApJ, 464, 641

Miller T. B., van Dokkum P., Mowla L., van der Wel A., 2019, ApJL, 872, L14

Mitchell P. D., Lacey C. G., Baugh C. M., Cole S., 2013, MNRAS, 435, 87

Miwa T., Noguchi M., 1998, ApJ, 499, 149

Miyazaki S., et al., 2018, PASJ, 70, S1

Miyoshi M., Moran J., Herrnstein J., Greenhill L., Nakai N., Diamond P., Inoue M., 1995, Nature, 373, 127

Moiseev A. V., Smirnova A. A., 2023, Galaxies, 11, 118

Moore T. J. T., Urquhart J. S., Morgan L. K., Thompson M. A., 2012, MNRAS, 426, 701

Morabito L. K., Dai X., 2012, ApJ, 757, 172

Mountrichas G., 2023, A&A, 672, A98

Muzzin A., et al., 2013, ApJ, 777, 18

Nair P. B., Abraham R. G., 2010, ApJS, 186, 427

Natarajan P., Volonteri M., 2012, MNRAS, 422, 2051

Nenkova M., Sirocky M. M., Ivezić Ž., Elitzur M., 2008a, ApJ, 685, 147

Nenkova M., Sirocky M. M., Nikutta R., Ivezić Ž., Elitzur M., 2008b, ApJ, 685, 160

Netzer H., 1993, ApJ, 411, 594

Netzer H., 2019, MNRAS, 488, 5185

Nipoti C., Londrillo P., Ciotti L., 2003, MNRAS, 342, 501

Noguchi M., 1987, MNRAS, 228, 635

O'Sullivan E., Forbes D. A., Ponman T. J., 2001, MNRAS, 328, 461

Oh K., Yi S. K., Schawinski K., Koss M., Trakhtenbrot B., Soto K., 2015, VizieR Online Data Catalog: Catalog of Type-1 AGNs from SDSS-DR7 (Oh+, 2015), VizieR On-line Data Catalog: J/ApJS/219/1. Originally published in: 2015ApJS..219....1O, doi:10.26093/cds/vizier.22190001

Okamoto T., 2013, MNRAS, 428, 718

Onken C. A., Ferrarese L., Merritt D., Peterson B. M., Pogge R. W., Vestergaard M., Wandel A., 2004, ApJ, 615, 645

Osterbrock D. E., Ferland G. J., 2006, Astrophysics of gaseous nebulae and active galactic nuclei. University Science Books

Pacucci F., Nguyen B., Carniani S., Maiolino R., Fan X., 2023, ApJL, 957, L3

Pancoast A., Brewer B. J., Treu T., 2011, ApJ, 730, 139

Pancoast A., Brewer B. J., Treu T., Park D., Barth A. J., Bentz M. C., Woo J.-H., 2014, MNRAS, 445, 3073

Park D., Kelly B. C., Woo J.-H., Treu T., 2012, ApJS, 203, 6

Park M.-J., et al., 2019, ApJ, 883, 25

Parry O. H., Eke V. R., Frenk C. S., 2009, MNRAS, 396, 1972

Paulino-Afonso A., et al., 2022, A&A, 662, A86

Pearson K., 1896, Philosophical Transactions of the Royal Society of London Series A, 187, 253

Peebles P. J. E., 1984, ApJ, 284, 439

Peng C. Y., 2007, ApJ, 671, 1098

Peng C. Y., Ho L. C., Impey C. D., Rix H.-W., 2002, AJ, 124, 266

Peng C. Y., Impey C. D., Ho L. C., Barton E. J., Rix H.-W., 2006, ApJ, 640, 114

Peng C. Y., Ho L. C., Impey C. D., Rix H.-W., 2010, AJ, 139, 2097

Persic M., Rephaeli Y., 2007, A&A, 463, 481

Peterson B. M., 1993, PASP, 105, 247

Peterson B. M., 2006, in Alloin D., ed., , Vol. 693, Physics of Active Galactic Nuclei at all Scales. Cambridge University Press, p. 77, doi:10.1007/3-540-34621-X˙3

Pier E. A., Krolik J. H., 1992, ApJ, 401, 99

Polyachenko E. V., 2013, Astronomy Letters, 39, 72

Pontzen A., Slosar A., Roth N., Peiris H. V., 2016, Physical Review D, 93, 103519

Pouliasis E., et al., 2019, MNRAS, 487, 4285

Powell L. C., Slyz A., Devriendt J., 2011, MNRAS, 414, 3671

Powell M. C., Krumpe M., Coil A., Miyaji T., 2024, A&A, 686, A57

Pozo Nuñez F., Bruckmann C., Deesamutara S., Czerny B., Panda S., Lobban A. P., Pietrzyński G., Polsterer K. L., 2023, MNRAS, 522, 2002

Querejeta M., et al., 2024, A&A, 687, A293

Ranalli P., Comastri A., Setti G., 2003, A&A, 399, 39

Ravindranath S., et al., 2004, ApJL, 604, L9

Rebolledo D., Wong T., Leroy A., Koda J., Donovan Meyer J., 2012, ApJ, 757, 155

Regan M. W., Teuben P. J., 2004, ApJ, 600, 595

Reines A. E., Volonteri M., 2015, The Astrophysical Journal, 813, 82

Reines A. E., Greene J. E., Geha M., 2013, ApJ, 775, 116

Ren W., Guo H., Shen Y., Silverman J. D., Burke C. J., Wang S., Wang J., 2024, ApJ, 974, 153

Richards G. T., et al., 2006a, ApJS, 166, 470

Richards G. T., et al., 2006b, Astrophys. J. Suppl. Ser., 166, 470

Rix H.-W., Zaritsky D., 1995, ApJ, 447, 82

Robertson B., Cox T. J., Hernquist L., Franx M., Hopkins P. F., Martini P., Springel V., 2006, ApJ, 641, 21

Robertson B. E., et al., 2023, Nature Astronomy, 7, 611

Roman-Oliveira F., Fraternali F., Rizzo F., 2023, MNRAS, 521, 1045

Rosario D. J., et al., 2013, A&A, 560, A72

Rosas-Guevara Y., et al., 2020, MNRAS, 491, 2547

Rosito M. S., et al., 2021, A&A, 652, A44

Rowlands K., et al., 2012, MNRAS, 419, 2545

Sachdeva S., Ho L. C., Li Y. A., Shankar F., 2020, ApJ, 899, 89

Saglia R. P., et al., 2016, ApJ, 818, 47

Saha K., Cortesi A., 2018, ApJL, 862, L12

Sahu N., Graham A. W., Davis B. L., 2019a, ApJ, 876, 155

Sahu N., Graham A. W., Davis B. L., 2019b, ApJ, 887, 10

Sahu N., Graham A. W., Hon D. S. H., 2023, MNRAS, 518, 1352

Sales L. V., Navarro J. F., Theuns T., Schaye J., White S. D. M., Frenk C. S., Crain R. A., Dalla Vecchia C., 2012, MNRAS, 423, 1544

Salpeter E. E., 1964, ApJ, 140, 796

Salucci P., Ratnam C., Monaco P., Danese L., 2000, MNRAS, 317, 488

Sanchez-Janssen R., Gadotti D. A., 2013, MNRAS, 432, L56

Sancisi R., Fraternali F., Oosterloo T., van der Hulst T., 2008, The Astronomy and Astrophysics Review, 15, 189

Sanders D. B., Phinney E. S., Neugebauer G., Soifer B. T., Matthews K., 1989, ApJ, 347, 29

Sauvaget T., Hammer F., Puech M., Yang Y. B., Flores H., Rodrigues M., 2018, MNRAS, 473, 2521

Savorgnan G. A. D., Graham A. W., 2016, ApJS, 222, 10

Scannapieco C., White S. D. M., Springel V., Tissera P. B., 2009, MNRAS, 396, 696

Schartmann M., Meisenheimer K., Klahr H., Camenzind M., Wolf S., Henning T., 2009, MNRAS, 393, 759

Schawinski K., Thomas D., Sarzi M., Maraston C., Kaviraj S., Joo S.-J., Yi S. K., Silk J., 2007, MNRAS, 382, 1415

Schawinski K., Virani S., Simmons B., Urry C. M., Treister E., Kaviraj S., Kushkuley B., 2009, ApJL, 692, L19

Schawinski K., Treister E., Urry C. M., Cardamone C. N., Simmons B., Yi S. K., 2011, ApJL, 727, L31+

Schawinski K., Simmons B. D., Urry C. M., Treister E., Glikman E., 2012, MNRAS, 425, L61

Schawinski K., Koss M., Berney S., Sartori L. F., 2015, MNRAS, 451, 2517

Schaye J., et al., 2015, MNRAS, 446, 521

Schlegel D. J., Finkbeiner D. P., Davis M., 1998, ApJ, 500, 525

Schmidt M., 1963, Nature, 197, 1040

Schneider D. P., et al., 2010, AJ, 139, 2360

Schramm M., Silverman J. D., 2013, ApJ, 767, 13

Schulze A., Wisotzki L., 2014, MNRAS, 438, 3422

Schutte Z., Reines A. E., Greene J. E., 2019, ApJ, 887, 245

Sellwood J. A., 1981, A&A, 99, 362

Sellwood J. A., Kahn F. D., 1991, MNRAS, 250, 278

Sellwood J. A., Masters K. L., 2022, ARA&A, 60

Sérsic J. L., 1968, Atlas de galaxias australes. Cordoba, Argentina: Observatorio Astronomico, 1968

Sesana A., 2013, MNRAS, 433, L1

Sesana A., Vecchio A., Volonteri M., 2009, MNRAS, 394, 2255

Shankar F., et al., 2016, MNRAS, 460, 3119

Shankar F., et al., 2019, MNRAS, 485, 1278

Shankar F., et al., 2025, MNRAS,

Shen Y., et al., 2011, ApJS, 194, 45

Shen Y., et al., 2023, arXiv:2305.01014 [astro-ph.GA 10.48550/arXiv.2305.01014

Shimizu T. T., Mushotzky R. F., Meléndez M., Koss M. J., Barger A. J., Cowie L. L., 2017, MNRAS, 466, 3161

Shlosman I., Frank J., Begelman M. C., 1989, Nature, 338, 45

Silk J., 2013, ApJ, 772, 112

Silk J., Mamon G. A., 2012, Research in Astronomy and Astrophysics, 12, 917

Silk J., Rees M. J., 1998, A&A, 331, L1

Silva A., Marchesini D., Silverman J. D., Martis N., Iono D., Espada D., Skelton R., 2021, ApJ, 909, 124

Silverman J. D., et al., 2008, ApJ, 675, 1025

Silverman J. D., et al., 2009, The Astrophysical Journal, 696, 396

Silverman J. D., et al., 2019, ApJL, 887, L5

Simard L., et al., 1999, ApJ, 519, 563

Simard L., et al., 2002, ApJS, 142, 1

Simard L., Mendel J. T., Patton D. R., Ellison S. L., McConnachie A. W., 2011, ApJS, 196, 11

Simmons B. D., Urry C. M., 2008, ApJ, 683, 644

Simmons B. D., Van Duyne J., Urry C. M., Treister E., Koekemoer A. M., Grogin N. A., The GOODS Team 2011, ApJ, 734, 121

Simmons B. D., Urry C. M., Schawinski K., Cardamone C., Glikman E., 2012, ApJ, 761, 75

Simmons B. D., et al., 2013, MNRAS, 429, 2199

Simmons B. D., et al., 2014, MNRAS, 445, 3466

Simmons B. D., Smethurst R. J., Lintott C., 2017, MNRAS, 470, 1559

Simpson C., Westoby P., Arumugam V., Ivison R., Hartley W., Almaini O., 2013, MNRAS, 433, 2647

Sivasankaran A., et al., 2025, MNRAS, 537, 817

Skelton R. E., et al., 2014, ApJS, 214, 24

Skrutskie M. F., et al., 2006, AJ, 131, 1163

Slater R., et al., 2019, A&A, 621, A83

Smethurst R. J., et al., 2016, MNRAS, 463, 2986

Smethurst R. J., Simmons B. D., Lintott C. J., Shanahan J., 2019, MNRAS, 489, 4016

Smethurst R. J., et al., 2021, MNRAS, 507, 3985

Smethurst R. J., et al., 2022, MNRAS, 510, 4126

Smethurst R. J., et al., 2024, MNRAS, 527, 10855

Soltan A., 1982, MNRAS, 200, 115

Somerville R. S., Primack J. R., Faber S. M., 2001, MNRAS, 320, 504

Somerville R. S., Hopkins P. F., Cox T. J., Robertson B. E., Hernquist L., 2008, MNRAS, 391, 481

Song M., et al., 2016, ApJ, 825, 5

Sparre M., Springel V., 2016, MNRAS, 462, 2418

Sparre M., Springel V., 2017, MNRAS, 470, 3946

Spergel D. N., et al., 2003, ApJS, 148, 175

Spinoso D., Bonoli S., Dotti M., Mayer L., Madau P., Bellovary J., 2017, MNRAS, 465, 3729

Steffen A. T., Strateva I., Brandt W. N., Alexander D. M., Koekemoer A. M., Lehmer B. D., Schneider D. P., Vignali C., 2006, AJ, 131, 2826

Strateva I., et al., 2001, AJ, 122, 1861

Sturm M. R., Reines A. E., 2024, ApJ, 971, 173

Suh H., Civano F., Trakhtenbrot B., Shankar F., Hasinger G., Sanders D. B., Allevato V., 2020, ApJ, 889, 32

Sun M., et al., 2015, ApJ, 802, 14

Sun B., Calzetti D., Battisti A. J., 2024, ApJ, 973, 137

Taranu D., Dubinski J., Yee H. K. C., 2015, ApJ, 803, 78

Thater S., et al., 2017, A&A, 597, A18

Thorne K. S., 1974, ApJ, 191, 507

Thornton C. E., Barth A. J., Ho L. C., Rutledge R. E., Greene J. E., 2008, ApJ, 686, 892

Tonini C., Mutch S. J., Croton D. J., Wyithe J. S. B., 2016, MNRAS, 459, 4109

Toomre A., 1964, ApJ, 139, 1217

Toomre A., 1977, in B. M. Tinsley & R. B. G. Larson D. Campbell ed., Evolution of Galaxies and Stellar Populations. p. 401

Trakhtenbrot B., Lira P., Netzer H., Cicone C., Maiolino R., Shemmer O., 2017, ApJ, 836, 8

Treister E., Urry C. M., 2006, ApJL, 652, L79

Treister E., et al., 2004, ApJ, 616, 123

Tremaine S., et al., 2002, ApJ, 574, 740

Trump J. R., et al., 2015, ApJ, 811, 26

Ulrich M.-H., Maraschi L., Urry C. M., 1997, ARA&A, 35, 445

Urrutia T., Lacy M., Becker R. H., 2008, ApJ, 674, 80

Urry C. M., Padovani P., 1995, PASP, 107, 803

Vera-Ciro C., D'Onghia E., Navarro J., Abadi M., 2014, ApJ, 794, 173

Vestergaard M., Peterson B. M., 2006, ApJ, 641, 689

Vika M., Vulcani B., Bamford S. P., Häußler B., Rojas A. L., 2015, A&A, 577, A97

Villforth C., 2023, The Open Journal of Astrophysics, 6, 34

Vogelsberger M., et al., 2014, Nature, 509, 177

Voges W., et al., 1999, A&A, 349, 389

Volonteri M., Ciotti L., 2013, ApJ, 768, 29

Volonteri M., Salvaterra R., Haardt F., 2006, MNRAS, 373, 121

Volonteri M., Dubois Y., Pichon C., Devriendt J., 2016, MNRAS, 460, 2979

Vulcani B., et al., 2014, MNRAS, 441, 1340

Walker I. R., Mihos J. C., Hernquist L., 1996, ApJ, 460, 121

Wandel A., 1999, ApJL, 519, L39

Wang E., Lilly S. J., 2022, ApJ, 927, 217

Wang Q. D., et al., 2013, Science, 341, 981

Wang L., et al., 2019, MNRAS, 482, 5477

Wardlow J. L., et al., 2011, MNRAS, 415, 1479

Weedman D. W., 1973, ApJ, 183, 29

Weiner B. J., Williams T. B., van Gorkom J. H., Sellwood J. A., 2001, ApJ, 546, 916

Weisskopf M. C., Brinkman B., Canizares C., Garmire G., Murray S., Van Speybroeck L. P., 2002, PASP, 114, 1

Williams R. J., Quadri R. F., Franx M., van Dokkum P., Labbé I., 2009, ApJ, 691, 1879

Willmer C. N. A., et al., 2006, ApJ, 647, 853

Winkel N., et al., 2025, ApJ, 978, 115

Woo J.-H., Schulze A., Park D., Kang W.-R., Kim S. C., Riechers D. A., 2013, ApJ, 772, 49

Wright E. L., et al., 2010a, AJ, 140, 1868

Wright E. L., et al., 2010b, AJ, 140, 1868

Wu J., Struck C., D'Onghia E., Elmegreen B. G., 2020, MNRAS, 499, 2672

Wuyts S., et al., 2007, ApJ, 655, 51

Yang G., et al., 2016, ApJ, 831, 145

Yang Y.-y., Zhang C.-m., Wang D.-h., Pan Y.-y., Zhou Z.-w., 2017, A&A, 41, 505

Yang L., Dai X., Lu Y., Zhu Z.-H., Shankar F., 2018, MNRAS, 480, 5504

Yang G., et al., 2020, MNRAS, 491, 740

York D. G., et al., 2000, AJ, 120, 1579

Yuan F., Narayan R., 2014, ARA&A, 52, 529

Yue M., et al., 2024, ApJ, 966, 176

Zanella A., et al., 2019, MNRAS, 489, 2792

Zhuang M.-Y., Ho L. C., 2023, Nature Astronomy, 7, 1376

Zibetti S., Charlot S., Rix H.-W., 2009, MNRAS, 400, 1181

Zinger E., et al., 2020, MNRAS, 499, 768

Zou F., Yang G., Brandt W. N., Xue Y., 2019, ApJ, 878, 11

Zou F., Yu Z., Brandt W. N., Tak H., Yang G., Ni Q., 2024, ApJ, 964, 183

Zubovas K., Nayakshin S., King A., Wilkinson M., 2013, MNRAS, 433, 3079

de Bernardis P., et al., 2000, Nature, 404, 955

de Sá-Freitas C., et al., 2023, A&A, 671, A8

de Vaucouleurs G., 1948, Annales d'Astrophysique, 11, 247

de Vaucouleurs G., 1959, Handbuch der Physik, 53, 275

de Vaucouleurs G., 1963, ApJS, 8, 31

de la Rosa I. G., La Barbera F., Ferreras I., Sánchez Almeida J., Dalla Vecchia C., Martínez-Valpuesta I., Stringer M., 2016, MNRAS, 457, 1916

do Nascimento J. C., et al., 2019, MNRAS, 486, 5075

van der Vlugt D., Costa T., 2019, MNRAS, 490, 4918

van der Wel A., et al., 2014, ApJ, 788, 28